NUCLEAR EQUATIONS OF STATE, SUPERFLUIDITY MODELS AND COLD NEUTRON STAR OBSERVATIONS

MELISSA MENDES

Department of Physics
Faculty of Science
McGill University, Montreal

July 2023

A thesis submitted to McGill University in partial fulfillment of the requirements of the degree of Doctor of Philosophy

STATEMENT OF ORIGINALITY

The research work contained in this thesis was conducted between September 2018 and July 2023. It is original work except where due reference is made. It has not been and shall not be submitted for the award of any degree or diploma to any other institution of higher learning.

I have performed all calculations on Chapter 4 and 5. The nucleonic equations of state were provided by my collaborator, Prof. Farrukh Fattoyev. The quark part of the hybrid equations of state, discussed on Chapter 3, was built by me, with the data constrain contours provided by my collaborator, Jan-Erik Christian. All figures were made by me.

Dedicated to prof. Marcelo Brites

One day you told me I was born to be a physicist.

That was the first day I actually believed it.

ABSTRACT

This research investigates neutron stars' innermost region, their core, and models of neutron star particle composition: the nuclear Equation of State (EOS). The goal of this research has been to combine data from nuclear physics measurements and astrophysics observations to constrain neutron star equations of state. In particular, I investigate neutron star core cooling and fast-cooling reactions involved in this process: the direct Urca (dUrca) reactions.

Initially, I consider only nucleonic matter (neutrons, protons) with electrons and muons and work with a family of 20 Relativistic Mean Field (RMF) EOS, to reproduce the luminosities of cold neutron stars MXB 1659-29 and SAX J1808.4-3625. I also include models describing proton and neutron core superfluidity, which influence neutron star cooling directly. I investigate 8 gap models of proton singlet superconductivity and 9 gap models of neutron triplet superfluidity. Additionally, I calculate each neutron star's total heat capacity for all these scenarios and show how, with precise temperature observations, one can infer the neutron star's heat capacity, thus, its core particle composition.

I find that all nucleonic EOS reproduce the inferred luminosities and that, up to a limit, less effective fast-cooling processes can reproduce them as well, in some cases, being favored over completely nucleonic dUrca processes. I also investigate the less efficient quark dUrca processes within quark-hadron hybrid neutron stars. I built a first-order phase transition, at chosen transition densities with a Maxwell construction, to quark matter, with an EOS parametrized by the speed of sound. I discuss the consequences of these results and the expectations coming with future observations.

RÉSUMÉ

Cette recherche porte sur la région la plus interne des étoiles à neutrons, leur cœur, et sur les modèles de composition des particules des étoiles à neutrons : l'équation d'état nucléaire (EOS). L'objectif de cette recherche est de combiner des données provenant de mesures de physique nucléaire et d'observations astrophysiques pour contraindre les équations d'état des étoiles à neutrons. En particulier, j'étudie le refroidissement du cœur des étoiles à neutrons et les réactions de refroidissement rapide impliquées dans ce processus : les réactions Urca directes (dUrca).

Dans un premier temps, je ne considère que la matière nucléonique (neutrons, protons) avec des électrons et des muons et je travaille avec une famille de 20 EOS à champ moyen relativiste (RMF), pour reproduire les luminosités des étoiles à neutrons froides MXB 1659-29 et SAX J1808.4-3625. J'inclus également des modèles décrivant la superfluidité des noyaux de protons et de neutrons, qui influencent directement le refroidissement des étoiles à neutrons. J'étudie 8 modèles de lacune de supraconductivité singulet du proton et 9 modèles de lacune de superfluidité triplet du neutron. En outre, je calcule la capacité thermique totale de chaque étoile à neutrons pour tous ces scénarios et je montre comment, avec des observations précises de la température, on peut déduire la capacité thermique de l'étoile à neutrons, et donc la composition des particules de son noyau.

Je constate que tous les EOS nucléoniques reproduisent les luminosités déduites et que, jusqu'à une certaine limite, les processus de refroidissement rapide moins efficaces peuvent également les reproduire et, dans certains cas, être favorisés par rapport aux processus dUrca entièrement nucléoniques. J'étudie également les processus dUrca de quark moins efficaces au sein des étoiles à neutrons hybrides quark-hadron. J'ai construit une transition de phase du premier ordre, à des densités de transition choisies avec une construction de Maxwell, vers la matière quark, avec un EOS paramétré par la vitesse du

son. Je discute des conséquences de ces résultats et des attentes liées aux observations futures.

ACKNOWLEDGEMENTS

This research would not have been possible without the support of the Schlumberger Foundation with the Faculty for the Future Fellowship, that sponsored the first four years of my PhD, and connected me with an incredibly inspiring community of fellows who are truly changing the world for the best, one degree at a time. I am also thankful for the support of the Mitacs Foundation, that financed my research internship at Goethe Universitaet, in Frankfurt, Germany, with a Globalink Research Award.

I thank my supervisors, prof. Charles Gale and prof. Andrew Cumming. Prof. Farrukh Fattoyev and prof. Juergen Schaffner-Bielich have also in many ways oriented this work and inspired its future steps, for which I am forever grateful. I also appreciate the technical support of Canada's Digital Research Alliance team, that has been vital to the computer-intensive calculations performed in this work, especially the ones realized on their clusters.

Many friends and family members supported me in various ways through the last five years. Without them, I wouldn't be half as motivated to pursue and finish this degree, thus this achievement is also theirs. Thank you for all the shared laughs and tears. Thank you for believing in this dream even when I couldn't put it into words and thank you for always showing me where the magic is.

Das ist nur der Anfang.

CONTENTS

LIST OF FIGURES

LIST OF TABLES

LIST OF ABBREVIATIONS

EOS Equation of State

dUrca direct Urca

RMF Relativistic Mean Field

QCD Quantum Chromodynamics

LMXB Low-Mass X-ray Binary

TOV Tolman-Oppenheimer-Volkov

PBF Pair Breaking and Formation

BPS Baym-Pethick-Sutherland

Part I

INTRODUCTION

In this section we introduce the reader to neutron stars. We outline a brief historical perspective of the field, including theoretical and observational milestones, and we explain how this research fills a knowledge gap. In addition, we summarize the goals of our work and describe how this thesis is organized.

1

INTRODUCTION

The existence of compact stars where general relativity effects are important was first conjectured by L. Landau in 1931, who, ironically to us nowadays, discussed the existence of stars without neutrons that challenged the laws of quantum mechanics [1]. After the discovery of the neutron, a more accurate description of those stars was proposed by W. Baade and F. Zwicky, also known to coin the term "neutron stars" in the literature [2]. They characterized these objects as massive, with a relatively small radius, thus extremely compact and mainly composed of neutrons. They also inferred that this compactness would explain the great amount of energy release in supernova outbursts, when, they conjectured, ordinary stars transform into neutron stars [3]. Supernova events had been observed several times in history, some dating back to around AD 1054 for particularly bright "stars", even seen during day time [2], but this paper was the first to suggest a relation between these observations and neutron stars. Their general characterization of neutron stars is very close to the current understanding of these objects: compact stars with masses between $1-2$ solar masses $(M_{\odot})$, radius between $10-15\,\text{km}$, composed mainly of neutrons [4]. The conjecture that neutron stars are a result of supernova outbursts is also the current standard framework, which has, nonetheless, evolved since then to include a more detailed description as well as computational simulations [5].

Soon afterwards the first appearances of neutron stars in the literature, Oppenheimer, Volkov [6] and Tolman [7], investigated the problem of the star stability. Inspired by a previous paper by Landau [8], they studied the effects of general relativity and non-relativistic neutron Fermi gas in neutron stars. The equations they used, nowadays known as the TOV equations, are still used to describe the internal pressure and mass of spherically symmetric non-rotating neutron stars. On the other hand, their simplified particle model, that disregarded particle interactions, has been replaced by more complex ones in the later years. Nowadays, describing matter in a high density environment, such as neutron stars, remains an active area of research.

The difficulties involved in these calculations lie mainly in the modelling of particle interactions for all densities. Some techniques attempt to solve this problem by approximating its Lagrangian as combinations of two- or three- body interactions [9]. This approach is called microscopic ab-initio, including for example, chiral effective field theory, which considers only short-range contact interactions and pion exchanges in its Hamiltonian [10]. The results of this kind of approach tend to work well in the low-density limit but they underestimate or ignore interactions that become important at higher densities, present in the innermost parts of neutron stars. Another possible approach to describe matter interactions in this environment is modelling them as particles interacting via exchanges of mesons, then determining the strength of those interactions by guaranteeing that the nuclear properties predicted by these models fit laboratory data. This is the phenomenological approach, which includes, for example, relativistic mean field (RMF) theory. RMF simplifies the calculation of its Lagrangian with the approximation that the particles interact with an averaged, or mean field [11]. Theories in this category generate results applicable to high density environments, but the strength of the interactions is not calculated from first-principles, instead being fixed to reproduce both finite nuclear and nuclear matter properties at densities close to equilibrium nuclear matter density. Another, more recent, approach has taken this generalization a step further and focused instead on interpolating the relationship between pressure and energy density for all matter densities from well-studied low density and high density limits. Pressure and energy density functions are known as equations of state (EOS). Equations of state are the macroscopic counterpart of the microscopic model of particle interactions. This technique interpolates between calculated EOS curves, valid at low densities, and perturbative Quantum Chromodynamics (QCD) EOS, which are reliable only at extremely high densities, to find the behavior of matter for intermediate densities [12]. This technique does not attempt to describe the microscopic model which generates that EOS, so it does not provide crucial quantities to calculate transport coefficients or luminosities, such as the particle fractions.

The examples above do not constitute a complete list of all neutron star EOS-building methods, but they illustrate how any particle interaction model is only an approximation of the real physical situation, thus, it will not be completely accurate in describing neutron stars. Another degree of freedom for which one has to account in this calculation is the possible existence of non-nucleonic particles inside neutron stars, that is, additional particles beyond the standard composition of neutrons, protons, electrons and muons. They can include heavier particles, such as delta resonances (Δ), baryons with strange quarks, such as hyperons $(\Upsilon : \Lambda, \Sigma, \Xi, \text{etc})$, a phase of free quark matter, among others. Nonetheless, for all particle compositions and interactions modelling techniques, one can test the reliability of the equation of state predictions by comparing them with data from astrophysical observations and laboratory measurements of nuclear properties. The latter includes nuclear charge radii, binding energies and, when available, neutron radii of spherical nuclei, among others [13]. The astrophysical observations are the ones related to the neutron star structure, such as mass, radius and tidal deformability, and the ones related to heat transport, such as neutrino luminosity and heat capacity, which cannot be directly measured, but are inferred from other observations [9]. The line of research in which this work is inserted uses this correspondence between data and equation of state predictions to constrain the equation of state space with the most precise data sets available.

Precise neutron star measurements are usually technically hard to achieve. One of the most successful methods of measuring neutron star masses uses the correspondence between orbital parameters and masses for pulsars in binary systems. The first mass measurement with this technique happened around 1979 for system PSR B1913 + 16, the first binary pulsar discovered [14]. The heaviest neutron star to date is MSP J0740 + 6620 with $M = 2.14^{+0.10}_{-0.09}\,M_\odot$ [15]. Neutron star radii observations tend to be less precise. They are usually obtained through analysis of the source's X-ray spectra, used to find its angular size or other emission effects that can be traced back to its radius. Therefore, this measurement depends on the neutron star distance to the telescope, its magnetic field and atmosphere composition [9], quantities that are prone to larger uncertainties. In particular, due to the nature of the measurement techniques and limitations of the observation instruments, it has been challenging to obtain precise mass and radius measurements for the same compact object. This situation changed thanks to the pulse profile modelling technique, which analyzes the brightness of temperature anisotropies (the "hot spots") on spinning neutron stars as a function of, among other quantities, their mass and radius [14]. Using this technique, the NICER collaboration has simultaneously determined, for PSR $J0030+0451$, $M = 1.34^{+0.15}_{-0.16}\,M_\odot$ and $R = 12.71^{+1.14}_{-1.19}\,\mathrm{km}$ [16] or, in independent analysis with a different spot configuration, $M = 1.44^{+0.15}_{-0.14}\,M_\odot$ and $R = 13.02^{+1.24}_{-1.06}\,\mathrm{km}$ [17]. For PSR $J0740+6620$, whose mass of $M = 2.08 \pm 0.07\,M_\odot$ is one of the most precise ever measured, NICER observations constrained its radius to $R = 13.7^{+2.6}_{-1.5}\,\mathrm{km}$ [18], or alternatively, $R = 12.39^{+1.30}_{-0.98}\,\mathrm{km}$ [19]. These are the most constraining mass and radii measurements to date. When the first detection of gravitational waves from a neutron star merger happened, an event known as GW170817, tidal deformabilities were able to be measured, and also used as an equation of state constraint. This first observation has determined the combined tidal deformability of the merging system as $\tilde{\Lambda} < 800$ or $\tilde{\Lambda} < 700$, depending on the assumptions about the compact stars' spins [20]. This value was later revised to $\tilde{\Lambda} = 300^{+420}_{-230}$, for respectively high and low values of spin [21]. This single measurement has significantly reduced the space of possible neutron star equations of state, displaying the relevance of this approach in determining the EOS of matter at high densities.

Neutrino luminosity and heat capacity provide less restricting constraints, nonetheless, they can offer a singular perspective in probing the microphysics of neutron stars' equations of state. In particular, it has been shown that the calculation of neutron star luminosity is very sensitive to its particle content, which may activate different cooling channels, and its particle interactions, which directly affect the effectiveness of some cooling processes [22]. For the same reasons, the formation of nuclear Cooper pairs is also important to neutron star cooling as well as heat capacity calculations. Considering all these factors, previous studies have investigated EOS compatibility to isolated neutron stars' inferred luminosities and ages [23], transiently-accreting neutron stars' luminosities and accretion rates [24] as well as neutron stars' luminosities and magnetic fields [25, 26]. Works in this research line are crucial to a better understanding of neutron stars' EOS expected properties and they help constraining the EOS space, however, currently both the neutron star equation of state and a consistent description of its nuclear pairing gap models remain undetermined. Furthermore, other works such as [27] have tested hadronic and quark-hadron hybrid EOS to find they both can be constructed to fit all current data, thus there is still also no consensus on whether a quark-hadron phase transition takes place in the interior of neutron stars.

Currently, the luminosities of 24 neutron stars in soft X-ray transients, that is, neutron stars in low-mass X-ray binaries that accrete material from a companion, are known. These luminosities are related to their average mass accretion rates, which in turn can be used to infer the neutrino luminosity of a source [28]. It is particularly interesting to investigate the neutrino luminosities of cold neutron stars, that must present fast-cooling processes in their interior. These processes were shown to be strongly dependent on the neutron star core equation of state [22], so by reproducing the neutrino luminosities of cold neutron stars one can potentially constrain some properties of its EOS. This work adds to this research line by investigating whether nucleonic and hybrid equations of state can naturally reproduce the luminosity of two sources, the neutron stars in MXB 1659-29 and SAX J1808.4-3658. The former has been observed in three different cycles of accretion-quiescence, which has improved the determination of its crust heat transport models, as well as temperature estimation [29]. Thanks to this increase in accuracy in the external layers modelling, the authors of [29] have been able to infer the neutron star core luminosity and even estimate the percentage of core volume involved in fast-cooling processes. On the other hand, SAX J1808.4-3658 is one of the coldest neutron stars ever observed, so reproducing its extremely low neutrino luminosity might strongly constrain the EOS. Furthermore, MXB 1659-29 is hotter than SAX J1808.4-3658, so pinpointing exactly how much of the neutron star's volume has to be undergoing fast-cooling processes to reproduce the luminosities of each of those sources can be very telling for the EOS, potentially even discriminating between nucleonic and quark-hadron hybrid equations of state.

In this work, we introduce a family of the simplest realistic nucleonic equations of state, composed only of neutrons, protons, electrons and muons. They are parametrized by the density slope of symmetry energy (L), a parameter one can infer from nuclei measurements [30, 31]. I investigate whether neutron star cooling observations can also set limits on the possible values of L, by investigating 20 EOS with $47\,\text{MeV} \leq L \leq 112.7\,\text{MeV}$.

Then I repeat the calculation with hybrid quark-hadron equations of state where the nucleonic part comes from the family of EOS above and the quark part is modelled by parametrizing the speed of sound. In both cases I investigate several superfluidity and superconductivity gap model parametrizations, respectively, for neutrons and protons, also considered in [32]. When dealing with hybrid EOS, I probe several possible phase transition densities and check whether reproducing the inferred luminosities constrains the space of phase transitions.

Part II of this thesis introduces the theoretical framework needed to develop neutron star luminosity calculations, including more details on the equations of state used. In Chapter 2, I present the differential equations one needs to solve to calculate neutron star structure and transport quantities, as well as some subtleties of numerical solving. I explain the importance of including nuclear pairing gap models in the neutrino emissivity and heat capacity calculations and detail how to properly incorporate them. In Chapter 3, the nucleonic and quark equations of state are detailed as well as the procedure to construct a consistent transition between the two phases. I also give an overview on the nuclear pairing gap models used in this work as well as their parametrizations. Part III describes in detail the results obtained for each scenario considered: in Chapter 4, for nucleonic EOS with all combinations of proton and neutron pairing gap models, including simulations of less efficient fast cooling processes; In Chapter 5, for quark-hadron hybrid EOS with several possible values of phase transition density. Part IV contains the conclusion, summarizing this research's results and contextualizing them in view of future experiments and observation plans.

Part II

THEORETICAL FRAMEWORK

The next chapters detail the theoretical framework used in this research as well as its implementation in the numerical code we developed. We overview the procedure to calculate neutron star structure and transport observables and detail both the nucleonic and quark equations of state used as well as the nuclear pairing gap models.

2

NEUTRON STAR BASICS

Compact stars refer to all stars to which general relativity effects are important, that include white dwarfs, neutron stars and exotic stars. Exotic stars are as compact as neutron stars but contain non-nucleonic particles or a quark phase. This thesis will explore important distinctions between neutron stars and exotic, quark-hadron hybrid neutron stars, especially in relation to their temperature evolution and inferred luminosities. For simplicity, I shall refer to those two types of compact stars as neutron stars in this chapter, since the theoretical framework developed here applies to both. Whenever details on a quark phase are discussed, I imply they refer only to the quark-hadron hybrid neutron stars.

To study this topic, I begin by characterizing neutron stars as well as their layers in section 2.1, then introducing the TOV equations in section 2.2, which are necessary to describe structural observables of non-rotating compact stars. In section 2.3, I detail the temperature evolution equations and explain the procedure to obtain important quantities from spectral observations. Then, I describe some neutron star cooling processes, their emissivities and the effects of nuclear pairing in section 2.4 and conclude, in section 2.5, by explaining how to calculate a neutron star's total heat capacity, including nuclear pairing effects.

2.1 NEUTRON STAR STRUCTURE

Based on neutron stars' surface emission, history and characteristics, one can classify them in non-exclusive categories, such as pulsars, magnetars, isolated neutron stars, etc. For the purposes of this work, I focus on transiently-accreting neutron stars, that is, neutron stars in binary systems that periodically accrete mass from their companion, which can be white dwarfs, main sequence stars or evolved stars. When this companion has a low mass, ($\lesssim M_\odot$), the system can be called Low-Mass X-ray Binary (LMXB) [2], the case of the neutron stars under study in this work. Transiently-accreting neutron stars go through cycles of accretion-quiescence, that is, a phase of high rate of mass accretion is followed by quiescence, when the accretion stops completely or is extremely reduced. During accretion, the observed X-ray spectrum originates mostly from the accretion disk, whereas during quiescence, it comes from the neutron star's surface [33].

For convenience, it is useful to artificially separate the neutron star in regions, based on their mass or number density. When the latter is used, the saturation density, $\mathrm{n_{sat}} \approx 0.15\,\mathrm{fm}^{-3}$, is a good reference for discriminating between regions of high and low density within the neutron star. The exact value of the saturation density depends on the EOS considered, but regardless, regions with $\mathrm{n} \leq \mathrm{n_{sat}}$ are considered low density regions, because one can access this limit in the laboratory, by studying nuclear properties. The saturation density also marks the point of minimum energy per nucleon in symmetric matter, that is, matter with the same number of protons and neutrons [11]. Its importance to the equation of state of neutron star matter, that is highly asymmetric, will be discussed in Chapter 3.

In the literature, the most common categorization divides the neutron star into inner and outer core, inner and outer crust and atmosphere. I briefly describe each of those regions:

- Inner core. The region with the highest densities, from approximately $n \gtrsim 2n_{\mathrm{sat}}$ [4]. Its composition is an open research problem, but may include heavy hadronic matter, such as delta resonances, strange matter such as hyperons, pion and kaon condensates or even free quark matter, in the case of hybrid quark-hadron neutron stars. Depending on the equation of state, lighter neutron stars might not reach those densities, thus, not present this region.

- Outer core. From $0.5\, n_{\mathrm{sat}} \lesssim n 2\, n_{\mathrm{sat}}$, this region's high density also prevents a precise determination of its composition, which strongly depends on the equation of state. The simplest possibility consists of a majority of neutrons, a few protons (proton fraction $Y_p \approx 0.1 - 0.2$, where Y_p is a ratio between the number of protons and the number of baryons), electrons and muons, for neutron stars in beta equilibrium, that is, in chemical balance such that the chemical potentials $\mu_n = \mu_p + \mu_e$. Free neutrons in abundance are expected because this region's density is significantly above the neutron drip density $\rho_{\text{drip}} \approx 4 \cdot 10^{14} - 5 \cdot 10^{14}\,\text{kg/m}^3$, that is, $\approx 4 - 5 \cdot 10^{-31}\,\text{kg/fm}^3$, the reference value over which it is more energetically favored for neutrons to unbind from nuclei [4]. Proton superconductivity and neutron superfluidity, defined in section 2.4.3, are also potentially present. This region extends for several kilometers and, for small neutron stars, can account for most of their volume.

- Inner crust. Composed of electrons, nuclei and free neutrons, this region starts at the neutron drip density, going from approximately $n_{\text{drip}} \leq n \lesssim 0.5\,n_{\text{sat}}$ [2]. Neutron superfluidity is expected to take place here as well. In addition, in its innermost layers, it is possible that the energy interaction between the nuclear force, shaping the nuclei surface energy, and the Coulomb energy force the nuclei into non-spherical exotic structures, resembling pasta shapes, forming what is called a pasta phase [34]. The presence of this phase could have consequences for neutron star properties including cooling [35].

- Outer crust. Also composed of electrons and nuclei, with $n < 0.5\,n_{\text{drip}}$. It may extend for several hundred meters, such that the total extension of outer and inner crust lies in the range of 10^2 to 10^3 m [2]. The ions organize in a lattice, that goes from a solid to a liquid form as the density increases [4].

- Atmosphere. In an analogy to planetary atmospheres, this is a blanket region extending up to 10 cm around the neutron star, composed of atoms or fully-ionized elements, for accreting neutron stars [2]. Its specific chemical composition is a reminiscence of processes that happened in that region of space, which might include previous matter accretions or, for non-accreting neutron stars, supernova remains from its creation.

Often it is convenient to also define a region called envelope, consisting of the neutron star atmosphere and most superficial layers of its crust. In section 2.3 I explain how the chemical composition of this region affects the modelling of neutron star interior temperature.

2.2 TOV EQUATIONS

The Tolman-Oppenheimer-Volkov (TOV) equation was first derived in Tolman's textbook [36] and it was described in detail in [6, 7]. To obtain it, one uses the most general spherically symmetrical static metric,

$$ds^2 = -e^{\lambda} dr^2 - r^2 d\theta^2 - r^2 \sin^2\theta d\phi^2 + e^{\nu} c^2 dt^2, \tag{2.1}$$

where λ and ν are generic functions of radius, and assume a perfect fluid energy-momentum tensor in general relativity equations. Adding a few reasonable considerations from a physical point of view, such that the pressure inside the star has to be larger than or equal to zero, one solves Einstein's equations to get the mass conservation equation (2.2), describing the mass distribution in the star's volume, and the TOV equation (2.3):

$$\frac{dm}{dr} = 4\pi r^2 \rho(r) \tag{2.2}$$

$$\frac{dp}{dr} = -\frac{Gm(r)\rho(r)}{r^2}\left(1 + \frac{p(r)}{\rho(r)c^2}\right)\left(1 + \frac{4\pi p(r) r^3}{m(r)c^2}\right)\left(1 - \frac{2Gm(r)}{rc^2}\right)^{-1}, \tag{2.3}$$

where G corresponds to the gravitational constant and c is the speed of light.

The mass density $\rho(r)$ and energy density $\epsilon(r)$ are related by $\rho(r) = \epsilon(r)/c^2$. The total radius R of the star is the value of r where the pressure $p = 0$, that is, at the boundary, thus, the total mass M is an integral of the internal mass at a given radius, $m(r)$, such that $M = \int_0^R 4\pi r^2 \rho(r) dr$. Note that, to correspond to neutron stars, it is necessary that

$R > R_{\text{Schwarzschild}} = 2GM/c^2$, or else the solution would be a Schwarzschild black hole [2].

This system of equations requires initial conditions $m(0) = 0$ and $p(0) = p_0$. They are used to describe non-rotating, low magnetic field neutron stars. Their compactness is measured by

$$C_{\text{comp}} = \frac{GM}{Rc^2} = \frac{g}{c^2} \quad , \tag{2.4}$$

where g is the surface gravity. Typical neutron stars, with $M = 1 - 2\,M_\odot$ and $R \approx 10 - 15$ km have $C_{\text{comp}} = 0.1 - 0.5$. The closer C_{comp} is to 1, the bigger the effects of general relativity. For non-rotating neutron stars, it was also shown [37] that $C_{\text{comp}} \geq 4/9 = 0.44...$, if the energy density is not increasing with the radius.

For the system of equations 2.2, 2.3 to be closed, one needs to specify a relation between $p(r)$ and $\rho(r)$, or equivalently, $p(\rho)$, known as an equation of state (EOS). Therefore, the structural observables of neutron stars, such as total mass and radius, do not depend on the microphysical properties of the EOS, such as particle composition or number density, but only on the bulk quantities of mass and pressure distribution. As it will be seen in Chapter 3, these bulk quantities are a result of EOS matter dynamics, thus, the most fundamental ingredients of equations of state are their particle composition and particle interactions, described by their Lagrangians, which uniquely determine all the neutron star properties [38].

Solving equations 2.2 and 2.3 is the minimum necessary to obtain information on the neutron star mass and radius. Mass versus radius curves pinpoint the total mass and radius of all possible stable neutron stars for a given EOS, an example shown in Figure 1. Stable neutron stars can be found by studying linear perturbations around hydrostatic equilibrium of the star's radial oscillations [39]. In most cases, this criterion has been shown to correspond to an analysis of the mass-radius curve [2], such that stable neutron stars are those whose total masses $m(R)$ increase with the central energy density $\epsilon(0) = \epsilon_0$. Thus, to find the maximum mass neutron star predicted by a given EOS, one can search for stars with decreasing mass for increasing ϵ_0, which translates

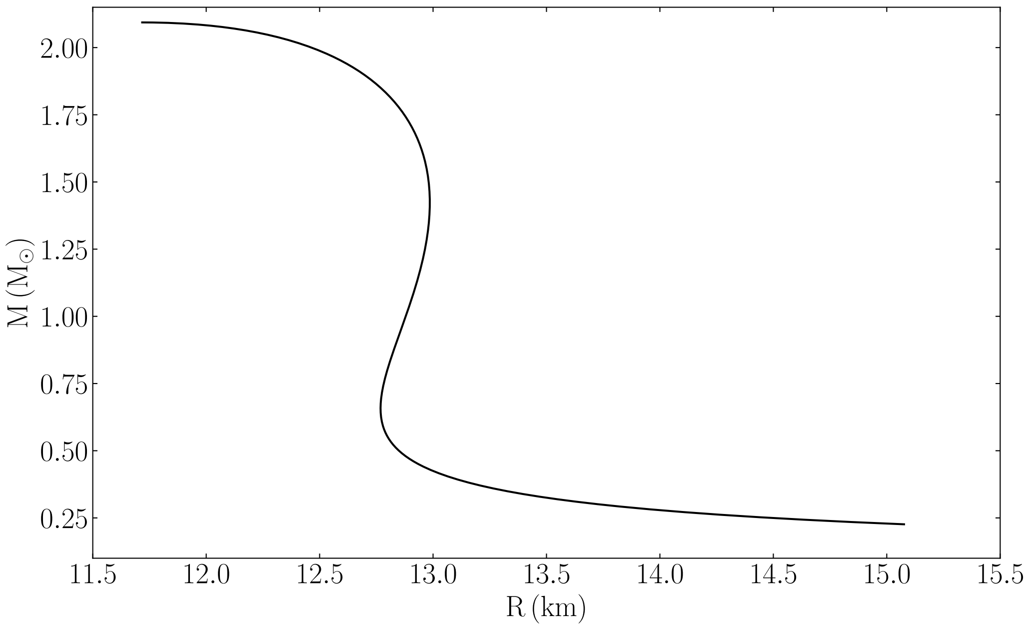

Figure 1: Mass-radius curve for a specific equation of state. Masses are displayed in terms of the solar mass $M_{\odot}$ and radii in km.

to a change of slope in the mass versus radius curve [2]. Because mass and radius are solutions to the system of linear first-order differential equations 2.2 and 2.3, they are exclusive to a given equation of state. In other words, given a curve of mass and radius simultaneous measurements, one can uniquely determine its generating equation of state and vice-versa [38, 40].

Furthermore, one can solve additional equations to obtain extra information, such as the neutron star's temperature evolution, to be discussed in section 2.3, or tidal deformability. For convenience, one can also calculate the quantity $\phi(r) = 1/2\nu(r)$, where $\nu(r)$ is the exponent of the exponential in the dt-term in equation 2.1. $\phi(r)$ is useful in the neutron star's cooling calculations, to be described in detail in section 2.4. This additional differential equation is given by

$$\frac{d\phi}{dr} = -\frac{dp}{dr}\frac{1}{\rho c^2 + p} \quad , \tag{2.5}$$

which requires a boundary condition. I use its known value at the total neutron star radius,

$$\phi(R) = \frac{1}{2}\ln\left(1 - \frac{2GM(R)}{Rc^2}\right). \tag{2.6}$$

2.2.1 *TOV numerical solver*

I wrote a routine in Python to perform all calculations in this research. I solve the TOV equations with an already developed one-dimensional differential equation solver, which uses an explicit Runge-Kutta method of order 3 [41], with adaptive step-size [42]. Other ODE solving methods were investigated in the same routine, including the more precise Runge-Kutta method of order 4. The time difference between these two methods was not significant and the difference between the solutions of neutron star masses and radii was only observed at the sixth decimal place, making it also not significant for the applications in this work.

Regarding the initial conditions, I do not usually start at $r_0 = 0$, but choose a finite r_0 such that $m(r_0) = m_0 \neq 0$, which facilitates numerical calculation. Fixing a r_0, one can find its corresponding m_0, and vice-versa, using the approximate relation

$$\rho_0 = \frac{m_0}{(4/3)\pi r_0^3} \quad , \tag{2.7}$$

given a corresponding ρ_0. I use $m_0 = 3 \cdot 10^{20}\text{kg} \approx 1.51 \cdot 10^{-10}\,\text{M}_\odot$. To deal with the boundary condition for $\phi(r)$, I solve equations 2.2, 2.3 and 2.5 assuming a placeholder value of $\phi(r_0) = 10^{-2}$ as initial condition. Then, I calculate $\phi(R)$ with equation 2.6, after knowing the total mass and radius of the neutron star in question, and correct all the $\phi(r)$ found with the TOV solver by adding a constant $C' = \phi(R)_{eq\,2.6} - \phi(R)_{TOV\,eq}$, such that $\phi(R)_{TOV\,eq} = \phi(R)_{eq\,2.6}$.

I fix the absolute and relative errors of the TOV solver to 10^{-8}. To speed up the convergence of the solution, I set the solver to stop calculating once $p(r) = 10^{18}\,\text{J/m}^3$ or $r = 30\text{km}$. This value of radius is an overestimation of the total radius a neutron star would have, thus, in the code, it acts as a safety stop: if it is ever reached, it means there was a problem in the convergence of the TOV solution, which one needs to investigate. The value of pressure was chosen because it is relatively close to zero for the purposes of this work. As a reference, typical central pressures of the neutron stars investigated in this work range around 10^{32} to $10^{34}\,\mathrm{J/m^3}$, so a final pressure of $10^{18}\,\mathrm{J/m^3} \approx 10^{-14}$ of the maximum pressure. Choosing a lower value of p_0 does not improve the code's precision significantly, but it does increase its running time.

2.3 TEMPERATURE EVOLUTION EQUATIONS

To study the neutron star temperature evolution, one should solve an additional independent system of tri-dimensional equations, which, as justified in [43], can be reduced to their 1D forms if the magnetic fields are weak. The simplified 1D equations are [44]:

$$\frac{d\left(L_r e^{2\phi(r)}\right)}{dr} = -\frac{4\pi r^2 e^{\phi(r)}}{\sqrt{1-2Gm(r)/c^2 r}}\left[\frac{d\epsilon(r)}{dt} + q_\nu e^{\Phi(r)}\right] \tag{2.8}$$

$$\frac{d\left(T e^{\phi(r)}\right)}{dr} = -\frac{1}{\lambda}\frac{L_r e^{\phi(r)}}{4\pi r^2\sqrt{1-2Gm(r)/c^2 r}} \tag{2.9}$$

Equation 2.8 describes the radial component of the internal luminosity L_r of the neutron star as a function of its internal energy variation with time $d\epsilon(r)/dt$ and the neutrino emissivity q_ν per volume. Thermal conduction processes determine a relationship between luminosity and temperature, equation 2.9, where the internal temperature T is a function of the internal luminosity and thermal conductivity λ. The two equations are connected by $\frac{d\epsilon(r)}{dt} = c_v \frac{dT}{dt}$, where c_v is the specific heat at constant volume thus, by solving equations 2.8 and 2.9, one obtains $T(t,r)$ and $L_r(t,r)$, respectively, the values of temperature and luminosity at all radii within the star. In particular, at its total radius R, $L_r(R)$ corresponds to the total luminosity of the neutron star at its surface. The effective luminosity observed a large distance away, L^∞, is redshifted such that $L^\infty = L_r(R)e^{2\phi(R)}$. The effective temperature one can observe is T_e^∞, defined as

$$T_e^\infty = T_s e^{\phi(R)} = \left(\frac{L^\infty}{4\pi R^{\infty\,2}\sigma_{SB}}\right)^{1/4}, \tag{2.10}$$

where T_s is the surface temperature, σ_{SB} is the Stefan-Boltzmann constant [44] and the observed radius R^∞ is given by $R^\infty = Re^{-\phi(R)}$.

One strategy to solve equations 2.8 and 2.9 is to divide the problem in two regions: outermost, dominated by heat transport processes, and innermost, dominated by neutrino emission. By doing that, one deals separately with the two main challenges in this calculation: for the outer layers, to determine their precise chemical composition, which directly affects heat transport, thus, the relationship between observed effective temperature T_e^∞ and the interior temperature $T(r)$; for the inner layers, the inclusion of all neutrino emission processes, which are very dependent on the EOS and will determine the neutron star total luminosity [22]. In the next section, 2.3.1, I explain how the effective temperature T_e^∞ can be obtained from the neutron star's X-ray spectrum.

2.3.1 *Spectral fits*

The effective temperatures of neutron stars are not directly measured but can be inferred from the neutron star spectrum. To obtain them, one starts by performing a numerical fit of the photon spectral flux, F^∞. The simplest possible model assumes its radiation identical to a blackbody's [33]. In this approximation,

$$F^\infty = \sigma_B T_e^{\infty\,4} \left(\frac{R}{D}\right)^2 \left(1 - \frac{2GM}{c^2 R}\right)^{-1}, \tag{2.11}$$

where D stands for the distance between the source and the telescope and I assume the effects from neutron star magnetic field and spin are negligible. That equation depends on the neutron star mass and radius, which might not be known when performing this numerical fit, hence one usually needs to estimate these values to obtain a neutron star's calculated temperature.

However, the blackbody spectrum approximation does not always fit the observed signal. In this case, an additional temperature dependence can be added, which improves the spectrum modelling, but reduces the precision of the temperature measurement, shifting it by a color correction factor f_c, such that $T_e^\infty = T_{\text{blackbody}}/f_c$, where $T_{\text{blackbody}}$ is the temperature a blackbody spectrum fit would provide. Deviations from a blackbody spectrum can suggest that important emission processes are taking place, for example, a transiently-accreting neutron star in quiescence might still be accreting matter from its companion [33].

The effective temperature obtained from equation 2.11 can be related to the quantity $\tilde{T}$, which in turn can used to calculate the neutron star's interior temperature through the relation $T(r) = \tilde{T}e^{-\phi(r)}$, valid for isothermal regions. The relationship between T_e^∞ and $\tilde{T}$ is strongly dependent on the chemical elements present at the neutron star envelope, a region at the boundary of the neutron star whose layers are not isothermal even after its crust and core have reached thermal equilibrium [45]. To find an expression relating $\tilde{T}$ and T_e^∞, one solves the TOV equations 2.2 and 2.3, as well as luminosity equations 2.8 and 2.9 for only the envelope layers of the neutron star, considering models for heat transport as a function of their chemical composition.

If the neutron star envelope mostly contains light elements, such as helium, then its thermal conductivity is high [46], leading to the expression

$$\tilde{T} = 0.552 e^{\phi(R)} \times 10^8 K \left[\left(\frac{T_e^\infty}{10^{24}\, K} \right)^4 e^{-3\phi(R)} \frac{10^{14} cms^{-2}\, R^2}{GM} \right]^{0.413}, \tag{2.12}$$

where the bracket is dimensionless and both $\tilde{T}$ and T_e^∞ are in Kelvin [47]. Equation 2.12 can be rewritten for easier code implementation to the equivalent expression

$$\tilde{T} = 0.552 \times 10^{3.044} e^{-0.239\ \phi(R)} \left(\frac{R^2}{GM} \right)^{0.413} T_e^{\infty\ 1.652}. \tag{2.13}$$

Note that the term in parenthesis has units of acceleration and the factor of 10 has units of acceleration and temperature such that $\tilde{T}$ is still in Kelvin. For the case when the envelope contains mostly heavy elements, such as iron, then, from [48],

$$\tilde{T} = 1.288 e^{\phi(R)} \times 10^{8} K \left[\left(\frac{T_e^{\infty}}{10^{24}\, K} \right)^4 e^{-3\phi(R)} \frac{10^{14} cm s^{-2}\, R^2}{GM} \right]^{0.455}, \tag{2.14}$$

which can be reorganized as

$$\tilde{T} = 1.288 \times 10^{2.54} e^{-0.365\ \phi(R)} \left(\frac{R^2}{GM} \right)^{0.455} T_e^{\infty\ 1.82}. \tag{2.15}$$

Observations suggest that young isolated neutron stars will have a light element envelope whereas older neutron stars' envelope will mostly be composed of heavy elements, suggesting that chemical envelope composition naturally changes with time [46]. However, neutron star age is not the only characteristic affecting envelope composition. For example, transiently-accreting neutron star envelopes will be mostly determined by the accreted material and the rate at which its light elements burn to heavy elements, so that, at quiescence, their envelopes can consist of a mixture of elements [45]. Given all the assumptions and estimates that go into deriving expressions 2.12 and 2.14, as well as into inferring which one should be used for a specific source, the determination of neutron star temperature is very model-dependent. Nonetheless, for transiently accreting sources, one may increase its precision by studying neutron stars whose spectrum most resembles a blackbody's and whose quiescent fluxes are the most similar between accretion periods [33]. This is the case for the neutron star in the MXB 1659-29 binary system, for example.

2.3.2 *Code implementation*

I took MXB 1659-29 and SAX J1808.4-3658 most likely effective temperatures from the literature. For the former, I follow [29, 45], with $T_e^{\infty} = 55$ eV and envelope composition of mainly light elements, which seem consistent with the crust cooling observations up to date. Hence, I use equation 2.12 to find the neutron star's internal temperature and solve for its inferred luminosity. The envelope composition of SAX J1808.4-3658 has not been precisely modelled, nonetheless, an upper limit on its luminosity has been established, indicating it is a fast-cooling source and one of the coldest transiently-accreting neutron stars observed [24]. From the modelling presented in [49], $T_e^{\infty} = 36^{+4}_{-8}$ eV, the effective temperature I use for this source. To find $T(r)$, I calculate both cases of light and heavy element envelope composition.

To reproduce the neutrino luminosities of transiently-accreting neutron stars, one needs to first estimate its value. A possible procedure to perform this calculation is explained in [29, 45], where they take the sources inferred average mass accretion rate $\langle \dot{M} \rangle$ and estimate the amount of deposited energy from accretion. Assuming most of this energy will be deposited as heat in the core, which later, during quiescence, will radiate as neutrinos, they estimate the neutron star's neutrino luminosity. For MXB 1659-29, the authors of [29] have run simulations for the calculation described above considering several models for the neutron star envelope, attempting to fit its X-ray emission spectrum. This calculation determined the most likely parameters of this source as a light element envelope, distance of $D = 10$ kpc and neutrino luminosity observed at infinity $L_\nu = (3.91 \pm 2) \times 10^{34}$ erg/s, with 1σ standard deviation. This result was verified to be insensitive to the uniformity of the outburst accretion rate or whether, for different quiescence-accretion cycles, the outburst recurrence durations are identical. Uncertainties on the source's distance or envelope composition could change the estimated luminosity by a factor of 2 [29]. In the cooling calculations, I attempt to reproduce the luminosities of $L_\nu = 2 \times 10^{34}$ erg/s, $L_\nu = 3.9 \times 10^{34}$ erg/s and $L_\nu = 8 \times 10^{34}$ erg/s for this neutron star.

For the other neutron star considered in this work, SAX J1808.4-3658, the estimations are less precise. I reproduce the procedure above to estimate the source's neutrino luminosity, without the numerical robustness of considering different envelope models and reproducing the X-ray spectral fit, hence obtaining only upper and lower limits on the inferred luminosity. From [49], I take $\langle \dot{M} \rangle = 9 \times 10^{-12} \mathrm{M}_\odot/\mathrm{yr} \approx 5.67 \times 10^{11}$ kg/s and I assume the energy deposited per nuclei in this accretion is $\mathrm{Q} = 0.5 - 2\,\mathrm{MeV}/\mathrm{m_u}$, for the lower and upper limits, where m_u is the atomic mass unit. Hence, the energy absorption rate by the crust $E = \langle \dot{M} \rangle Q \approx 6.83 \times 10^{44}$eV/s $\approx 1 \times 10^{33}$ erg/s, if $Q = 2$ MeV/m_u, and $E \approx 1 \times 10^{32}$ erg/s, if $Q = 0.5$ MeV/m_u. The deposited energy will eventually be transferred to the core as heat, which will later be dissipated by neutrinos, thus it approximately corresponds to the neutron star's neutrino luminosity. With the cooling calculations, I attempt to reach the luminosities of $L_\nu = 1 \times 10^{32}$ erg/s and $L_\nu = 1 \times 10^{33}$ erg/s for this source.

2.4 COOLING PROCESSES

Cooling processes are all reactions that emit particles which escape the neutron star, thereby removing energy from it. For cold neutron stars, $(T \lesssim 10^9\text{K})$, made only of neutrons, protons, electrons and muons, ($npe\mu$ EOS), and assuming the framework of the Standard Model of Particle Physics, those particles are photons and neutrinos [43]. Neutrinos are emitted from reactions within the core and crust, while photons, that are always optically thick, only escape from the photosphere, where they are emitted as a result of heat transport processes between the neutron star interior and its surface [22].

For hot neutron stars, neutrinos might be trapped, that is, their mean-free path could be smaller than the radius of the neutron star. This could be the case, for example, of proto-neutron stars and merging neutron stars. In this situation, the star might also not be in chemical equilibrium, that is, its composition may change, hence, one should re-evaluate which cooling processes are important as well as their emissivities. In this thesis I will only work with cold neutron stars in beta equilibrium, that is, neutron stars whose particle composition is not expected to change as they cool down. Then, when investigating cooling one must include both decay and capture processes simultaneously, for example, $n \rightarrow pl\bar{\nu}_l; \quad pl \rightarrow n\nu_l$, where l stands for a lepton and ν_l, its corresponding neutrino.

Each reaction resulting in photon or neutrino emission contributes to the total neutron star luminosity, calculated with equation 2.8, with their individual rates q_ν and energy transport processes. Furthermore, with equation 2.9, each reaction has a given relation with the neutron star temperature, T, which is also a function of time. Then, one can associate each cooling reaction with the rate it takes to cool the neutron star by itself, thus classifying them into slow- and fast-cooling processes. Slow-cooling processes have a dependency of T^8, thus $T(0,t) \propto t^{-1/6}$, when they dominate, whereas fast-cooling processes have T^6, thus, $T(0,t) \propto t^{-1/4}$ [22]. In this thesis I will focus on fast-cooling processes, happening in the neutron star core, but I briefly mention neutrino emitting reactions taking place in the whole star for reference.

2.4.1 *Slow-cooling processes*

These processes are the most common. They happen throughout the neutron star, but when including nuclei, they take place at the crust. For a $npe\mu$ EOS, they include [22]:

- Neutron-neutron, proton-proton, neutron-proton bremsstrahlung $(NN \to NN\nu\bar{\nu})$, where N is a neutron or proton.
- Electron-nucleus bremsstrahlung $(eN \to eN\nu\bar{\nu})$, where N is a nucleus.
- Plasmon decay $(\gamma \to \nu\bar{\nu})$, where γ is a plasmon, that is, a quantum of plasma oscillation, or a photon. This reaction can also be rewritten as $e \to e\nu\bar{\nu}$, where e represents electrons interacting with the plasma microfields [22].
- Electron-positron, $\mu^- - \mu^+$ pair annihilation $(ee^+ \to \nu\bar{\nu}; \quad \mu\mu^+ \to \nu\bar{\nu})$
- Modified Urca $(nN \to pNl\bar{\nu}_l; \quad pNl \to nN\nu_l)$, where N is a spectator particle and l represents a lepton.
- Lepton modified Urca $(\mu p \to ep\bar{\nu}_e\nu_\mu;\ ep \to \mu p\bar{\nu}_\mu\nu_e;\ \mu e \to ee\bar{\nu}_e\nu_\mu;\ ee \to \mu e\bar{\nu}_\mu\nu_e;\ \mu\mu \to e\mu\bar{\nu}_e\nu_\mu;\ e\mu \to \mu\mu\bar{\nu}_\mu\nu_e)$.
- Nuclei beta decay $(A,Z) + e \to (A,Z-1) + \nu_e$, $(A,Z-1) \to (A,Z) + e + \bar{\nu}_e$; $(A,Z) \to (A,Z-1) + e^+ + \nu_e$, $(A,Z-1) + e^+ \to (A,Z) + \bar{\nu}_e$.

As the density in the neutron star increases, more processes become available, thus this is not a comprehensive list. Even though one should ideally include as many processes as possible when calculating the neutron star luminosity, often the emissivities of some processes are considerably smaller than others. This is the case, for example, of lepton modified Urca and nuclei beta decay processes, whose neutrino emissivities are so low, even among other slow-cooling processes, that, for cold neutron stars, they can usually be ignored [22]. When an equation of state does not reach densities where fast-cooling processes are allowed, that is, when only slow-cooling processes determine the neutron star temperature evolution, this scenario is called "minimal cooling model" or "standard cooling".

2.4.2 *Fast-cooling processes*

These processes happen at higher densities, thus, in the neutron star core. They are called, in a wordplay in Russian and Brazilian Portuguese, direct Urca processes, dUrca, in reference to their cooling efficiency [22]. The emissivity of those reactions is much larger than the slow-cooling processes, thus, when active, they dominate. This scenario is also called "enhanced cooling".

Those reactions are such as $n \to pl\bar{\nu}_l; \quad pl \to n\nu_l$, where the neutron and proton can be replaced with other particles, for example, delta-resonances or hyperons, for other hadronic equations of state, or free quarks, for hybrid quark-hadron EOS. l and the subscript ν_l correspond to any lepton, but for neutron star densities, it often refers to electrons and, in some cases, muons. τ could in principle also participate, but the densities at which it becomes energetically favourable for them to appear are very high and normally not reached within neutron stars.

2.4.2.1 *Nucleonic*

One can calculate the emissivity of reactions $n \to pl\bar{\nu}_l; \quad pl \to n\nu_l$ by, in a first approximation, assuming in-medium effects are negligible. The emissivity of the beta-decay equals that of the proton capture reaction, thus, it suffices to calculate one of those and double it to obtain the neutrino emission rate of the whole process. Following [22], one can find that that rate is given by

$$Q^{(\mathrm{D})} = 2\int \frac{\mathrm{d}\mathbf{k}_n}{(2\pi)^3}\,\mathrm{d}W_{i\to f}\epsilon_\nu f_n\left(1-f_p\right)\left(1-f_e\right), \tag{2.16}$$

where $\mathrm{d}W_{i\to f}$ is the beta decay differential probability, f_x is the Fermi distribution of particle x, ϵ_ν, the neutrino energy distribution. All these factors are integrated over the neutron momenta $\mathbf{k}_n$. This integral can be simplified by assuming those reactions take place at the Fermi surface and that the neutrino momentum is much smaller than that of the other particles. Then, the integral can be rewritten as

$$\begin{aligned} Q^{(\mathrm{D})} = \frac{2}{(2\pi)^8}T^6 4\pi \int \mathrm{d}\Omega_1\,\mathrm{d}\Omega_2\,\mathrm{d}\Omega_3\delta\left(\mathbf{k}_n-\mathbf{k}_p-\mathbf{k}_e\right) \\ \int_0^\infty \mathrm{d}x_\nu x_\nu^3\left[\prod_{j=1}^{3}\int_{-\infty}^{+\infty}\mathrm{d}x_j f_j\right]\delta\left(x_1+x_2+x_3-x_\nu\right)\left|M_{fi}\right|^2\prod_{j=1}^{3}k_{\mathrm{F}j}m_j^* \end{aligned} \tag{2.17}$$

with the squared matrix element $\left|M_{fi}\right|^2 = 2G_\mathrm{F}^2\cos^2\theta_\mathrm{C}\left(1+3g_A^2\right)$ and j representing each particle species, where $j=1$, 2, and 3 stand for the neutron, proton and electron respectively. Dirac delta functions are indicated by $\delta(x)$.

In expression 2.17, T represents temperature, $\mathrm{d}\Omega_x$ are the elements of solid angle integrating the particle momenta $\mathbf{k}_x$ and x_i are the energies of the particles, such that $x_j = \left(\epsilon_j-\mu_j\right)/T \simeq v_{\mathrm{F}j}\left(k-k_{\mathrm{F}j}\right)/T$ and $x_\nu = \epsilon_\nu/T$. In-medium corrections are then included in the effective Landau masses m_n^*, m_p^*, that are defined as

$$m_{n,\,p}^* = \sqrt{m_{\mathrm{Dirac}\;n,\,p}^2 + k_{n,\,p}^2}\quad, \tag{2.18}$$

where $k_{n,\,p} = \left(3\pi^2 n_{n,\,p}\right)^{1/3}$ in natural units where $\hbar = c = 1$ [50], and the Dirac masses, $m_{\mathrm{Dirac}\,n,p} = m_{\mathrm{vacuum}\,n,\,p} - g_s\phi$, where g_s is the sigma meson Yukawa coupling constant, and ϕ is the corresponding sigma meson field, parameters that will be discussed again in Chapter 3. One can further define $m^* = m_{\mathrm{Dirac}\,n,p}/m_{\mathrm{vacuum}\,n,\,p}$. G_F is the weak interaction constant, θ_C, the Cabibbo angle, and g_A is the value of the axial vector coupling in vacuum. Further in-medium corrections are added by replacing g_A with g_A^* [51], where

$$g_A^* \simeq g_A \left(1 - \frac{n}{4.15\,(n_{sat} + n)}\right), \tag{2.19}$$

and n_{sat} is the value of number density at saturation. Performing the integral in equation 2.17 leads to the total rate

$$\epsilon_{\text{Urca}} = \frac{457\pi}{10080} G_{\text{F}}^2 \cos^2\theta_{\text{C}} \left(1 + 3g_{\text{A}}^{*2}\right) \frac{m_n^* m_p^*}{\hbar^{10} c^3} \frac{\left(3\pi^2\hbar^3 Y_e n\right)^{1/3}}{c} (k_{\text{B}} T)^6, \tag{2.20}$$

where Y_x are the particle fractions, thus Y_e corresponds to the electron fraction, also provided by the equation of state.

Note that, for 3-body reactions like the direct Urca ones, which happen at the Fermi surface, energy-momentum conservation implies that they can only happen if $k_{Fn} \leq k_{Fp} + k_{Fe}$, which can be rewritten in terms of the particle fractions of the proton Y_p, the neutron Y_n and electron Y_e, such that

$$Y_p \geq Y_{\text{p dUrca}} = \left[Y_n^{1/3} - Y_e^{1/3}\right]^3. \tag{2.21}$$

The advantage of working with equation 2.21 is that proton fractions are microphysical parameters of equations of state. Therefore, one can relate the onset of dUrca processes to a certain density threshold within the neutron star core or a proton fraction threshold within the equation of state. Those relationships are important because they help setting constraints on the EOS: knowing there are very cold neutron stars one can only explain with fast-cooling processes, it becomes evident some part of the neutron star EOS has to be above the dUrca threshold.

This realization excludes several equation of state candidates for neutron stars. In the 1990′s, works such as [52, 53] showed that realistic equations of state can be above the dUrca threshold, which has encouraged deeper investigations on the reproducibility of neutron star luminosities by different EOS, including factors that could change the emissivity 2.20. The authors of [54], for example, have found that superfluidity is crucial to explain the luminosity data when dealing with nucleonic EOS. How superfluidity diminishes the efficiency of dUrca reactions will be detailed in section 2.4.3.1.

Other studies have explored how different particle compositions affect neutrino dUrca luminosity, such as [55] that has showed that EOS with hyperons are also consistent with observational constraints and even hybrid quark-hadron neutron stars have been shown to reproduce the inferred luminosities of neutron stars [56]. This research builds on these results to investigate an interesting family of nucleonic EOS, as well as hybrid quark-hadron equations of state with updated data constraints. Quark dUrca emissivities are discussed next.

2.4.2.2 *Quark*

Analogously to the derivation of the nucleonic direct Urca emissivities, one obtains the quark dUrca emissivity in the quark phase

$$\epsilon_{\text{q Urca}} \simeq \frac{214}{315}\frac{G_{\text{F}}^2\cos^2\theta_{\text{C}}}{\hbar^{10}c^6}\alpha k_{\text{F}}(d)k_{\text{F}}(u)k_{\text{F}}(e)\,(k_BT)^6 \tag{2.22}$$

for reactions $d \to u + e^- + \bar{\nu}_e, \quad u + e^- \to d + \nu_e$, assuming finite quark mass effects are negligible [57]. The new quantity α is the strong coupling constant, which is a function of density, and is expected to be of the order of ≈ 0.1 for core neutron star densities [58]. Again, I assume the reactions take place approximately at the Fermi surface and one can write, for a given quark q,

$$\begin{aligned} k_{\text{F}}(q) &= (\pi^2\hbar^3 n_q)^{1/3} \approx 235\left(\frac{\rho}{\rho_{sat}}\right)^{1/3}\frac{\text{MeV}}{c}, \\ k_{\text{F}}(e) &= (3Y_e)^{1/3}k_{\text{F}}(q) \end{aligned} \tag{2.23}$$

valid when

$$n_u = n_d = n_{\text{baryons}},\; n_e = 0 \tag{2.24}$$

so I can rewrite equation 2.22 as

$$\epsilon_{\text{q Urca}} = \frac{914}{315}\frac{G_{\text{F}}^2 \cos^2\theta_{\text{C}}}{\hbar^{10}c^9}\alpha Y_e^{1/3}\left(k_{\text{B}}T\right)^6 \frac{\rho}{\rho_{sat}}\left(\frac{1.602176634 \cdot 10^{-13} \cdot 235}{3^{1/9}}\right)^3 \text{J/m}^3\text{s} \quad (2.25)$$

where ρ is the mass density, but one could also write that expression in terms of baryonic number density, such that

$$\epsilon_{\text{q Urca}} = \frac{914}{315}\frac{G_{\text{F}}^2 \cos^2\theta_{\text{C}}}{\hbar^{10}c^6}(3Y_e)^{1/3}\alpha\pi^2\hbar^3 n(k_{\text{B}}T)^6\,\text{J/m}^3\text{s}. \quad (2.26)$$

Expressions 2.23 and, consequently, 2.25, are exactly valid given condition 2.24, which does not necessarily always hold within compact stars with charge neutrality. Therefore, for the system under study, equations 2.25 and 2.26 are only approximately valid. Furthermore, if $n_e = 0$, then $Y_e = 0 \rightarrow \epsilon_{\text{q Urca}} = 0$, thus, to have non-zero quark dUrca neutrino emission while simultaneously being close enough to the conditions 2.24 to use expression 2.25, one needs a small non-zero electron fraction in the quark equation of state. There is no quark dUrca threshold because the energy-momentum conservation expression $k_{\text{F}}(d) \leq k_{\text{F}}(u) + k_{\text{F}}(e)$ leads to the condition $Y_e \geq 0$, which is always valid.

Similar reactions including strange quarks are possible and likewise emit neutrinos with approximately the same rate, equation 2.25, for similar conditions as before, $n_s = n_u = n_d = n_{\text{baryons}}$, $n_e = 0$ [57]. Nonetheless, most realistic quark EOS models include strange quarks only at relatively high densities, which might not include the cold neutron star core limits [59, 60]. In this research I assume all conditions allowing equation 2.25 hold, thus, that will be the expression used whenever there is quark direct Urca cooling.

2.4.3 *Nuclear pairing*

The phenomena of superconductivity and superfluidity have been experimentally observed around 1910 and 1930 respectively. Back then, it was found that, below a critical temperature, an attractive force appears in electron-phonon interactions, making it energetically favorable for electrons of certain elements to form pairs, called Cooper pairs.

When these pairs form an electrically charged medium, it is said the material is a superconductor, and when not, a superfluid. Starting in 1958 and in later years, theoretical investigations studied the possibility that, somewhat similarly, neutrons and protons could undergo pairing in specific conditions [61]. Particularly, the interior of neutron stars posed a convenient environment for this study because its high pressure could allow for the realization of that phenomenon in larger temperatures than laboratory-induced electron pairing. Nonetheless, the calculations of nuclear pairing properties, such as energy gaps and critical temperature, in high density environments, like neutron stars, are still an open research problem. Possible pairing models are discussed in Chapter 3.

When dealing with nuclear pairing, one needs to also account for the existence of spin in nuclei, thus consider the channels for nuclear pairing in terms of L_J^{2S+1}, where S is the nuclear pair spin, J the total angular momentum and L the orbital angular momentum. Models of nuclear interaction applicable to neutron stars predict that the singlet S_0^1 neutron superfluidity happens in the neutron star crust [2]. The lower densities in this region reduce the importance of in-medium effects, thus, making the current calculations more reliable. This is not the case of the denser core, where the singlet S_0^1 proton superconductivity and the triplet P_2^3 neutron superfluidity are expected to take place and whose gap models' calculation is more challenging [61].

It is of relevance to this research to consider how nuclear pairing affects neutron star cooling. Primarily, the number of nuclei available to join all cooling processes is reduced, because some of them will be in Cooper pairs, thus, there is a suppression of fast- and slow- cooling emissivities, discussed in section 2.4.3.1. On the other hand, the formation and breaking of nuclear pairs can also emit neutrinos, therefore contributing to the neutron star cooling, through reactions like $N + N \to \mathcal{C} + \nu_f + \bar{\nu}_f$, where $\mathcal{C}$ corresponds to the Cooper pair of nucleon N and the subscript f indicates the neutrino flavours. These processes are called Pair Breaking and Formation (PBF), with emissivity [22]

$$\epsilon_{\mathrm{PBF}} = 3\frac{4G_{\mathrm{F}}^2 m_N^* k_{\mathrm{F}}}{15\pi^5\hbar^{10}c^6}\,(k_{\mathrm{B}}T)^7\,aF(y), \tag{2.27}$$

where k_{F} if the Fermi momentum of the nuclei in question, a is a dimensionless number which depends on nuclear pairing type and $F(y)$ is a function such that, for proton singlet

$$F_{\mathrm{A}}(y_{\mathrm{A}}) = \left(0.602y_{\mathrm{A}}^2 + 0.5942y_{\mathrm{A}}^4 + 0.288y_{\mathrm{A}}^6\right)\left(0.5547 + \sqrt{(0.4453)^2 + 0.0113y_{\mathrm{A}}^2}\right)^{1/2} \times \exp\left(-\sqrt{4y_{\mathrm{A}}^2 + (2.245)^2} + 2.245\right), \quad (2.28)$$

and for neutron triplet,

$$F_{\mathrm{B}}(y_{\mathrm{B}}) = \frac{1.204y_{\mathrm{B}}^2 + 3.733y_{\mathrm{B}}^4 + 0.3191y_{\mathrm{B}}^6}{1 + 0.3511y_{\mathrm{B}}^2}\left(0.7591 + \sqrt{(0.2409)^2 + 0.3145y_{\mathrm{B}}^2}\right)^2 \times \exp\left(-\sqrt{4y_{\mathrm{B}}^2 + (0.4616)^2} + 0.4616\right), \quad (2.29)$$

where $y_{\mathrm{A,B}} = \Delta_{\mathrm{A},B}/k_{\mathrm{B}}T$ are the nuclear pairing energy gaps divided by temperature, assuming 3 neutrino flavours are participating in this process [22].

Its temperature dependence T^7 indicates this is a "medium"-cooling process, with a cooling rate between the slow- and fast-cooling rates, but because of its dependence with the energy gap, one can check that it actually becomes efficient only for $T \lesssim T_c$ [62]. Despite some studies that found these processes can dominate neutron star cooling in some cases, especially before the onset of direct Urca processes [22], I have not at the moment included their contribution in the cooling calculations.

Similarly to nuclear pairing, the effect of color superconductivity has been conjectured to exist on the possible quark phase of neutron stars. If that is the case, then quark direct Urca cooling would also be suppressed by this type of superconductivity, however its onset and gap model predictions are currently very model-dependent and there is still a debate on whether neutron stars would reach densities high enough to contain this phase of matter. Due to this uncertainty, quark color superconductivity is not included in this work.

2.4.3.1 *Reduction rates*

The direct Urca neutrino emissivity suppression due to the presence of superfluidity or superconductivity can be found by accounting for their energy gaps (Δ) in equation 2.16. To perform this calculation, it is useful to write Δ as a function of $\tau = T/T_c$ and its anisotropy, that is, the angle between the particle momentum and the z-axis of the Fermi-sphere (ϑ). S_0^1 nuclear pairings are isotropic, so their dimensionless energy gap is not a function of ϑ and can be written

$$y_A = \frac{\Delta}{k_\mathrm{B}T} = \sqrt{1-\tau}\left(1.456 - \frac{0.157}{\sqrt{\tau}} + \frac{1.764}{\tau}\right). \tag{2.30}$$

The energy gap for P_2^3 nuclear pairings is $y_B = \Delta/k_\mathrm{B}T = \sqrt{1+3\cos^2\vartheta}\, v_B$, where

$$v_B = \sqrt{1-\tau}\left(0.7893 + \frac{1.188}{\tau}\right), \tag{2.31}$$

assuming the projection of the Cooper pair momentum into the quantization axis is $m = 0$. Other projections, with other energy gaps, could be feasible in neutron stars, but in this work I assume P_2^3 pairings are always $m = 0$ for simplicity. Equations 2.30 and 2.31 are analytical approximations of the result of BCS equations that issue less than 1% error when compared to their numerical values [63].

Note that in integrating equation 2.16 with the new expressions for energy, there will be a significant difference whether two nuclear pairings are simultaneously active or not. In case only proton superconductivity is present, I use $\epsilon'_\mathrm{Urca} = \epsilon_\mathrm{Urca} R_\mathrm{proton}$, where the reduction factor is

$$R_\mathrm{proton} = \left[0.2312 + \sqrt{(0.7688)^2 + (0.1438\, v_A)^2}\right]^{5.5} \times \exp\left(3.427 - \sqrt{(3.427)^2 + v_A^2}\right). \tag{2.32}$$

When only neutron superfluidity is present, $\epsilon'_\mathrm{Urca} = \epsilon_\mathrm{Urca} R_\mathrm{neutron}$ with

$$R_{\text{neutron}} = \left[0.2546 + \sqrt{(0.7454)^2 + (0.1284\ v_B)^2}\right]^5 \times \exp\left(2.701 - \sqrt{(2.701)^2 + v_B^2}\right). \quad (2.33)$$

If $\tau \leq 1$, by definition the nuclear pairing is not active, thus, the dUrca emissivity is not suppressed and $R_{\text{proton, neutron}} \equiv 1$. The analytical expressions 2.32 and 2.33 are also approximations with average error smaller than 1% [63].

When more than one nuclear pairing is active, new reduction rates for cooling processes should be calculated. However, performing the integral 2.16 for these cases usually does not lead to a result that can be easily approximated by an analytical expression for all values of τ. In this case, a useful approximation is $R_{\text{proton, neutron}} \sim \min\left(R_{\text{proton}}, R_{\text{neutron}}\right)$. Thus, I consider the strongest nuclear pairing will dominate and only its reduction rate is taken into account to determine the reduced direct Urca neutrino emissivity. In the cooling code, this is the expression used when both proton superconductivity and neutron superfluidity gap models are simultaneously active.

2.4.4 *Cooling calculation code implementation*

To verify that the neutron stars with direct Urca processes can reproduce the neutrino luminosity of MXB 1659-29 and SAX J1808.4-3658, I perform cooling calculations for the core of these neutron stars, assuming slow-cooling as well as crust cooling processes can be ignored in this preliminary analysis, because their cooling rates are subdominant. For reference, the modified Urca emissivity is of the order of $\epsilon_{\text{m Urca}} \approx \left(10^{17} - 10^{20}\right)\left(T/10^9\right)^8 \text{J/m}^3$, while the direct Urca is $\epsilon_{\text{Urca}} \approx \left(10^{22} - 10^{26}\right)\left(T/10^9\right)^6 \text{J/m}^3$ [22]. Therefore, I do not include the emissivities of any of these other processes, opting for working only with nucleonic neutrino direct Urca rates (equation 2.20), for the nucleonic EOS, and both nucleonic and quark direct Urca rates (equation 2.25) for the hybrid quark-hadron EOS, including the nuclear pairing reduction factors when necessary.

Hence, equation 2.8 is reduced to $L_r(r) = \int_{r_0}^{r'} \frac{4\pi r^2 q_\nu e^{2\phi(r)}}{\sqrt{1-2Gm(r)/c^2 r}} dr$ and by solving it I obtain only the neutrino core luminosity for a given neutron star. Instead of modelling the heat blanket envelope for each star to obtain a relationship between the effective temperature, T_e^∞, and the interior temperature, $T(r)$, I take the expressions from literature as well as the sources' most likely T_e^∞ and envelope compositions, as explained in section 2.3.2. After calculating the dUrca neutrino luminosity for neutron stars of $M = M_\odot$ up to the most massive ones for all EOS under study, I solve the optimization problem of finding the central pressure and energy density of the neutron star with the exact values of luminosity for which I am searching. I use the Scipy routine optimize.brent or, for faster calculation with less precision, a linear interpolation.

2.5 HEAT CAPACITY

Heat capacities quantify the ability of a material or substance to store heat. Therefore, in the context of neutron star research, it is an important quantity to calculate, because it is intrinsically connected to the star's heat transfer processes and cooling, as seen in equation 2.9. A neutron star total heat capacity C is a sum of the individual particles' heat capacities, such that, for the specific volumetric heat capacities c_x,

$$C = \int_0^R \frac{4\pi r^2 \sum_x (c_x e^{-\phi(r)})}{(1-(2Gm(r)/c^2 r))^{1/2}} dr. \tag{2.34}$$

In general, one can find the specific volumetric heat capacities c_x by integrating each particle species energy density and chemical potential with regards to particle momenta. For neutrons, protons and electrons within neutron stars, that are strongly degenerate, the specific volumetric heat capacities can be written

$$c_x = \frac{m_x^* k_{\mathrm{F}\ x} k_{\mathrm{B}}^2 T}{3\hbar^3} \quad , \tag{2.35}$$

in this expression, the Fermi momentum $k_{\mathrm{F}\ x} = (3\pi^2\hbar^3 n_x)^{1/3}$, and for electrons $m_e^* \approx m_e$, while, for protons and neutrons, m_x^* represents their respective effective Landau masses.

2.5.1 *Nuclear pairing reduction rates*

Similarly to neutrino emissivities in neutron star cooling, nuclei heat capacities are also reduced when nuclear pairing processes are active. The new heat capacities are given by $c'_x = R_x c_x$. To find the reduction factor R_x, one must once again integrate each particle species energy density and chemical potential with regards to particle momenta, but now also accounting for nuclear pairing energy gaps. For all limits of $\tau = T/T_c$, an analytical approximation to this integral has been found [64], that gives, for proton superconductivity S_0^1,

$$R_A = \left[0.4186 + \sqrt{(1.007)^2 + (0.5010u_A)^2}\right]^{2.5} \exp\left(1.456 - \sqrt{(1.456)^2 + u_A^2)}\right)$$
$$\text{where } u_A = \sqrt{1-\tau}\left(1.456 - \frac{0.157}{\sqrt{\tau}} + \frac{1.764}{\tau}\right). \quad (2.36)$$

For neutron superfluidity P_2^3,

$$R_B = \left[0.6893 + \sqrt{(0.790)^2 + (0.03983u_B)^2}\right]^{2} \exp\left(1.934 - \sqrt{\left((1.934)^2 + \frac{u_B^2}{16\pi}\right)}\right)$$
$$\text{where } u_B = \sqrt{1-\tau}\left(5.596 + \frac{8.424}{\sqrt{\tau}}\right). \quad (2.37)$$

The expressions above have less than 1.2% of error in comparison with numerical results, even so, they present a small region with $R_{A,B} > 1$. This violates the definition, in which $R_{A,B} = 1$ only when $T > T_c$, that is, when nuclear pairing channels are not active, hence $c'_x = c_x$, and equation 2.35 remains valid. This approximation error can be fixed by numerically forcing $R_{A,B} \geq 1$ whenever $T \geq T_c$. Nonetheless, I verified that $R_{A,B} > 1$ only happens in small enough neutron star volumes that it becomes insignificant when calculating the neutron star total heat capacity and chose not to include this correction in the cooling code. The new expression for the total heat capacity becomes

$$C = \int_0^R \frac{4\pi r^2 \sum_x (c'_x e^{-\phi(r)})}{(1-(2Gm(r)/c^2 r))^{1/2}} dr. \tag{2.38}$$

2.5.2 *Approximate relation between heat capacity and luminosity*

Even though neutron stars' total heat capacity cannot be directly measured, it can be inferred from other quantities. Obtaining its value is relevant because heat capacities are a function of neutron stars' particle composition, thus, investigating them may help in the determination of the equation of state. With this goal, the authors of [45] have obtained an approximate expression that relates neutron star core heat capacity and neutrino luminosity for fast-cooling transiently-accreting neutron stars in quiescence

$$\frac{C_{core}/10^{38}}{L_\nu/10^{35}} = \left(\frac{\Delta\tilde{T}/\tilde{T}}{0.3\%}\right)^{-1} \left(\frac{t_q}{10\ yr}\right) (\tilde{T}/10^8)^{-1}. \tag{2.39}$$

Note that the star's total heat capacity and neutrino luminosity are normalized respectively by factors 10^{38} erg/K and 10^{35} erg/s. $\Delta\tilde{T}$ corresponds to the temperature variation in quiescence time t_q, which is also normalized by a factor of 10 years. $\tilde{T}$ is the non-redshifted local temperature, such that, as seen before, $T(r) = \tilde{T}e^{-\phi(r)}$.

Equation 2.39 comes from rewriting the relation $\frac{d\epsilon(r)}{dt} = c_v \frac{dT}{dt}$ for the core of quiescent neutron stars, so one can ignore photon contributions to their luminosity as well as the heat exchange between crust and core. Focusing on direct Urca cooling processes, that have $L_\nu \propto \tilde{T}^6$, one can write

$$C_{core}\frac{d\tilde{T}}{dt} = -L_\nu \Rightarrow \left(\frac{\tilde{T}_i}{\tilde{T}_f}\right)^4 = 4\frac{L_\nu \Delta t}{C\tilde{T}} + 1, \tag{2.40}$$

leading to equation 2.39. It provides a relationship for the inference of core heat capacity as a function of the neutron star's neutrino luminosity and temperature variation $(\Delta\tilde{T}/\tilde{T})$, quantities that can be obtained through observations. In particular, the authors of [45] have predicted that, for cold neutron stars MXB 1659-29, KS $1731-260$ and XTE J$1701-462$, $C_{core} < 2-5\times 10^{36}\left(\tilde{T}/10^{8}\right)$ erg/K. Additional measurements of those sources' temperature variation could establish a more precise value for C_{core} instead of just upper limits, thus determining whether these sources are under strong superfluidity or not, even if their nuclear pairing gap models are unspecified. Calculations of the core heat capacity of neutron stars MXB 1659-29 and SAX J1808.4-3658, predicted by the equations of state and nuclear pairing models considered in this work, will be detailed in Chapter 4.

3

EQUATIONS OF STATE

In this chapter I briefly describe the equations of state and nuclear pairing gap models used in this research. In section 3.1, I focus on the family of nucleonic EOS and how they affect the dUrca threshold. Section 3.2 presents the nuclear pairing gap models with which I work, as well as a convenient parametrization to represent them. Hybrid EOS are introduced in section 3.3, where I detail the phase construction method and its implementation in the cooling code.

3.1 NUCLEONIC EOS

To model the particle content of the neutron star core, I chose to work with the simplest matter composition, consisting of neutrons, protons, electrons and muons, ($npe\mu$ EOS). The family of nucleonic equations of state modelling their interactions was based on the FSUGold2 EOS [65], an equation of state created to reproduce the ground-state properties of finite nuclei such as binding energy, charge radii as well as their monopole response, that is, the centroid energies of their monopole resonances, and the maximum observed neutron star mass at the time [66].

The nucleonic EOS used in this work were updated to reflect the most recent astrophysical data constraints. They were built by our collaborator Prof. Farrukh J. Fattoyev and provided to us in tabular form. Their Lagrangian is written as $\mathcal{L} = \mathcal{L}_0 + \mathcal{L}_{\text{int}}$, split in a non-interacting part $\mathcal{L}_0$ and an interacting part $\mathcal{L}_{\text{int}}$, where

$$\mathcal{L}_0 = \bar{\psi}\left(i\gamma^\mu\partial_\mu - M\right)\psi + \frac{1}{2}\left(\partial_\mu\phi\partial^\mu\phi - m_\text{s}^2\phi^2\right) + \frac{1}{2}m_\text{v}^2 V_\mu V^\mu - \frac{1}{4}F_{\mu\nu}F^{\mu\nu} + \frac{1}{2}m_\rho^2 \boldsymbol{b}_{\boldsymbol{\mu}}\cdot\boldsymbol{b}^{\boldsymbol{\mu}} - \\ - \frac{1}{4}V_{\mu\nu}V^{\mu\nu} - \frac{1}{4}\boldsymbol{b}_{\boldsymbol{\mu\nu}}\cdot\boldsymbol{b}^{\boldsymbol{\mu\nu}}, \quad (3.1)$$

$$\mathcal{L}_{int} = \bar{\psi}\left[g_s\phi - \left(g_{\rm v}V_\mu + \frac{g_\rho}{2}\tau\cdot\boldsymbol{b_\mu} + \frac{e}{2}\left(1+\tau_3\right)A_\mu\right)\gamma^\mu\right]\psi - \frac{\kappa}{3!}\left(g_{\rm s}\phi\right)^3 - \frac{\lambda}{4!}\left(g_{\rm s}\phi\right)^4 + \\ + \frac{\zeta}{4!}\left(g_{\rm v}^2 V_\mu V^\mu\right)^2 + \Lambda_{\rm v}\left(g_{\rm v}^2 V_\mu V^\mu\right)\left(g_\rho^2 \boldsymbol{b_\mu}\cdot\boldsymbol{b^\mu}\right). \quad (3.2)$$

In this Lagrangian, the nucleon interactions are modelled by the exchange of mesons, such that ϕ represents the interactions of the σ-meson, V^μ the w-meson and $\boldsymbol{b}_\mu$ the ρ-meson. The fields are defined by

$$\begin{aligned} F_{\mu\nu} &= \partial_\mu A_\nu - \partial_\nu A_\mu \quad , \\ V_{\mu\nu} &= \partial_\mu V_\nu - \partial_\nu V_\mu \quad , \\ \mathbf{b}_{\mu\nu} &= \partial_\mu \mathbf{b}_\nu - \partial_\nu \mathbf{b}_\mu \quad , \end{aligned} \quad (3.3)$$

such that the σ meson field mediates intermediate attractive interactions between the nucleons, the V^μ field, short range repulsive interactions, the $\mathbf{b}^\mu$ field, isospin dependence and A_μ is the photon-field [11]. The γ^μ matrices are also known as the Dirac matrices and the τ and τ_3 are the Pauli matrices. The strength of each interaction is estimated with the relativistic mean field (RMF) approximation, so they represent average values, determined to reproduce nuclear properties and astrophysical constraints.

The energy per nucleon generated by the Lagrangian above can be approximated to second order in α as

$$E(n,\alpha) \approx E_{\rm SNM}(n) + E_{\rm sym}(n)\cdot\alpha^2 + \mathcal{O}\left(\alpha^4\right) \quad , \quad (3.4)$$

where $E_{\rm SNM}(n)$ stands for the energy of symmetric nuclear matter, that is, matter with the same number of protons and neutrons, and $E_{\rm sym}(n)$ is the symmetry energy, corresponding to the contributions of asymmetric nuclear matter to the energy. The parameter $\alpha = (n_{\rm n} - n_{\rm p})/(n_{\rm n} + n_{\rm p})$, quantifies the asymmetry in the number of protons and neutrons. The symmetric and asymmetric parts of the EOS can also be written as expansions around saturation density [67],

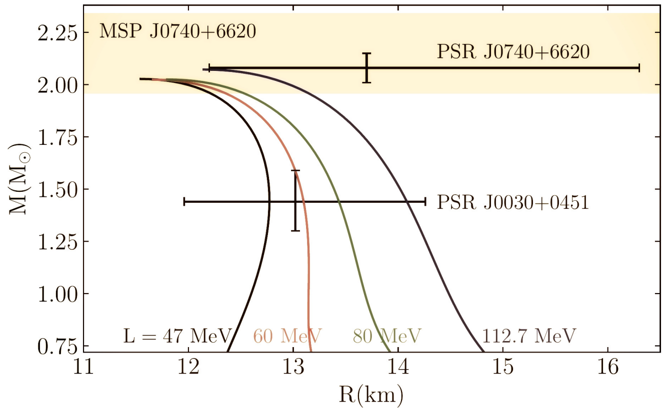

Figure 2: Mass-radius curves for L47, L60, L80 and L112.7 EOS including error bars of the NICER measurements for PSR J0030+0451 and PSR J0740+6620. The shaded horizontal region marks the mass limits of heaviest neutron star observed to date, MSP J0740+6620.

$$
\begin{aligned}
E_{\mathrm{SNM}}(n) &= \mathrm{B} + \frac{1}{2}\mathrm{K}x^2 + \cdots \\
E_{\mathrm{sym}}(n) &= \mathrm{J} + \mathrm{L}x + \frac{1}{2}\mathrm{K}_{\mathrm{sym}}x^2 + \cdots
\end{aligned}
\tag{3.5}
$$

where $x = (n - n_{\mathrm{sat}})/3n_{\mathrm{sat}}$. The saturation density is the point of minimum energy per nucleon in symmetric matter [11], B is the energy per nucleon and K is the incompressibility coefficient of symmetric nuclear matter. In the expression $E_{\mathrm{sym}}(n)$, the parameter J is the value of symmetry energy at saturation density, while L is the slope of symmetry energy and $\mathrm{K}_{\mathrm{sym}}$ is the curvature of symmetry energy, both at saturation density.

One of the goals of this research has been to identify whether equations of state with various values of L would fit the neutrino luminosities of cold neutron stars. Hence, I used a family of EOS with L varying from 47 to 112.7 MeV and $\zeta = 0.0256$, but identical values of $\mathrm{B} = -16$ MeV, $\mathrm{K} = 230$ MeV and $n_{\mathrm{sat}} = 0.1504\,\mathrm{fm}^{-3}$, such that they make identical predictions for the ground state properties of finite nuclei and present a range of neutron star masses and radii compatible with astrophysical constraints. Figure 2 illustrates how the maximum mass neutron star and NICER simultaneous measurements of mass and radius of two neutron stars can be reproduced by all investigated EOS.

Assuming matter within stable neutron stars is in chemical equilibrium and electrically neutral, the beta-equilibrium condition can be written such that the proton fraction is

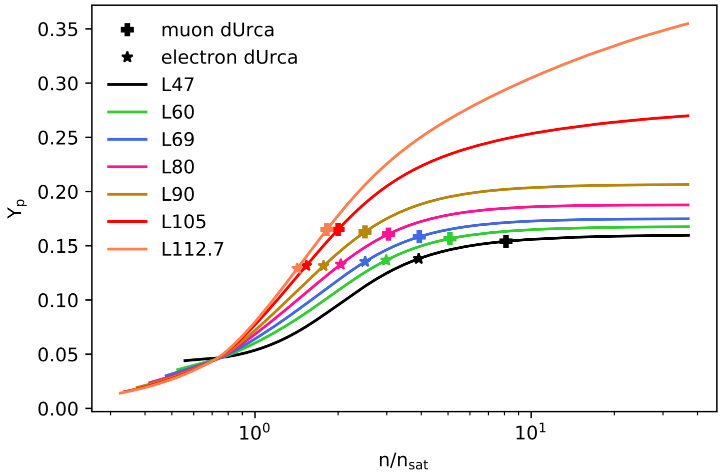

Figure 3: Proton fractions as a function of density, for various equations of state. The stars mark the dUrca threshold for dUrca reactions that do not include muons and the diamonds, the dUrca threshold for dUrca reactions that do.

a function of the symmetry energy expansion, equation 3.5. In the simplified case of neutron stars without muons, Y_p is approximately [66]:

$$Y_p \simeq \frac{64}{3\pi^2 n_{\text{sat}}\,(3x+1)} \left(\frac{\mathrm{J} + \mathrm{L}x + \frac{1}{2}\mathrm{K}_{\text{sym}} x^2}{\hbar c} \right)^3 . \tag{3.6}$$

The proton fraction is proportional to the symmetry energy, as previously discussed in [68] and, for densities up to around $1.5\,n_{\text{sat}}$, E_{sym} can be well approximated by its first three terms, as shown in the numerator of the parenthesis in expression 3.6, thus it is intuitive to check that EOS with larger L have larger proton fractions at a fixed supra-saturation density. Expression 3.6 suffers important corrections from the higher order terms of the symmetry energy at larger densities.

The proportionality relation between Y_p and L holds when muons are also present in the EOS, which explains why the dUrca threshold is reached at earlier densities for large L EOS, as seen in Figure 3. In this Figure I also show the dUrca threshold when muons also participate in direct Urca processes, that is, at densities where $Y_p \geq \left[Y_n^{1/3} - Y_\mu^{1/3} \right]^3$ and the total dUrca emissivity is $\epsilon = 2\,\epsilon_{\text{Urca}}$, (equation 2.20). As explained in Chapter 2, including dUrca reactions with muons doubles the dUrca emissivity because $\epsilon_{\text{Urca}\,\mu} = \epsilon_{\text{Urca}}$.

In addition to the core equation of state described above, I use the Baym-Pethick-Sutherland (BPS) equation of state [69] as the outer crust EOS and the Negele-Vautherin EOS [70] as the inner crust equation of state. These crust EOS were also provided by my collaborator, prof. Farrukh Fattoyev. They are the standard choice within the literature to describe neutron star crust, but using other crust equations of state would not significantly change the calculated masses, even if it may slightly alter radii predictions [71]. Regarding neutron star cooling, the crust contribution to the neutrino luminosity is considered negligible because I focus on fast cooling processes, in specific, direct Urca reactions, that happen in the neutron star core. Thus, altering the crust EOS would not affect the cooling results significantly.

3.1.1 *Code implementation*

Once the equations of state are determined, I concatenate the lists of crust and core points of energy density, pressure and number density. In this process, some limiting points may be discarded to increase the smoothness of the transitions. Each case is evaluated individually to make sure the resulting list of points is consistent with the regions of influence of each EOS. Then, those points are used as a base to build linear spline interpolations of each of those quantities. Working with interpolations instead of the points themselves is advantageous because it guarantees a faster convergence of the TOV solver. I use the already integrated splrep routine [72] within Scipy, that finds a spline representation of a curve using the FORTRAN routine curfit. The evaluation of points using spline is performed with the splev routine [73], that is also a wrapper around the FORTRAN routine of same name.

3.2 NUCLEAR PAIRING GAP MODELS

Nuclear pairing gap models at high density environments such as neutron star cores are very EOS-dependent, because hard-to-model in-medium effects are crucial to their determination. Some efforts have been taken to consistently calculate superfluidity gap models for a given equation of state, for example, [74], however, it becomes increasingly difficult to model particle interactions at large densities or even to estimate the accuracy of the models used.

An alternative approach to deal with this issue is working with parametrizations of gap models, curves which contain a number of free parameters one can adjust to describe the superfluidity critical temperature as a function of density. These gap model parametrizations are not consistently calculated with the equation of state, but depend on it. For example, a possible parametrization is shown in [32], given by

$$\Delta\left(k_{\mathrm{Fx}}\right)=\Delta_0 \frac{\left(k_{\mathrm{Fx}}-k_0\right)^2}{\left(k_{\mathrm{Fx}}-k_0\right)^2+k_1} \frac{\left(k_{\mathrm{Fx}}-k_2\right)^2}{\left(k_{\mathrm{Fx}}-k_2\right)^2+k_3} \quad , \tag{3.7}$$

where k_{Fx} is the Fermi momentum of the nucleons x and the free parameters are Δ_0, k_0, k_1, k_2 and k_3, shown in table 1 for the proton superconductivity gap models, identified with the prefix "PS", and in table 2, for the neutron superfluidity gap models, identified with the prefix "NT". The nucleons' Fermi momenta are EOS-dependent and can be related to the EOS number densities. References for more details on each gap model are indicated within the tables.

Figures 4 and 5 show each model's energy gap and critical temperature as a function of the Fermi momenta. The accuracy of the gap model parametrizations can be evaluated by comparing their predictions for neutron star cooling with luminosity data or temperature variation measurements. Some studies, for example [23], have used Bayesian techniques to investigate the most likely values for these parameters by fitting the observed luminosities of neutron stars.

3.3 QUARK EOS

In Chapter 5, I discuss quark-hadron hybrid stars as a possible alternative to reproduce the neutrino luminosities of MXB 1659-29 and SAX J1808.4-3625. The quark part of the EOS is modelled by parametrizing the speed of sound, following [89, 90]. Its energy density is given by

Table 1: Proton superconductivity gap models parameters and main references. Adapted from [32].

Name	Δ_0 (MeV)	k_0 (fm^{-1})	k_1 (fm^{-2})	k_2 (fm^{-1})	k_3 (fm^{-2})	Reference
PS AO	14	0.15	0.22	1.05	3.8	[75]
PS BCLL	1.69	0.05	0.07	1.05	0.164	[76]
PS BS	17	0.0	2.9	0.8	0.08	[77]
PS CCDK	102	0.0	9.0	1.3	1.5	[78]
PS CCYms	35	0.0	5.0	1.1	0.5	[79]
PS CCYps	34	0.0	5.0	0.95	0.3	[79]
PS EEHO	4.5	0.0	0.57	1.2	0.35	[80]
PS EEHOr	61	0.0	6.0	1.1	0.6	[81]
PS T	48	0.15	2.1	1.2	0.8	[82]

Table 2: Neutron superfluidity gap models parameters and main references. Adapted from [32].

Name	Δ_0 (MeV)	k_0 (fm^{-1})	k_1 (fm^{-2})	k_2 (fm^{-1})	k_3 (fm^{-2})	Reference
NT AO	4.0	1.2	0.45	3.3	5.0	[83]
NT BEEHS	0.45	1.0	0.40	3.2	0.25	[84]
NT EEHO	0.48	1.28	0.1	2.37	0.02	[85]
NT EEHOr	0.23	1.2	0.026	1.6	0.0080	[81]
NT SYHHP	1.0	2.08	0.04	2.7	0.013	[86]
NT T	1.2	1.55	0.05	2.35	0.07	[87]
NT TTav	3.0	1.1	0.60	2.92	3.0	[88]
NT TToa	2.1	1.1	0.60	3.2	2.4	[88]

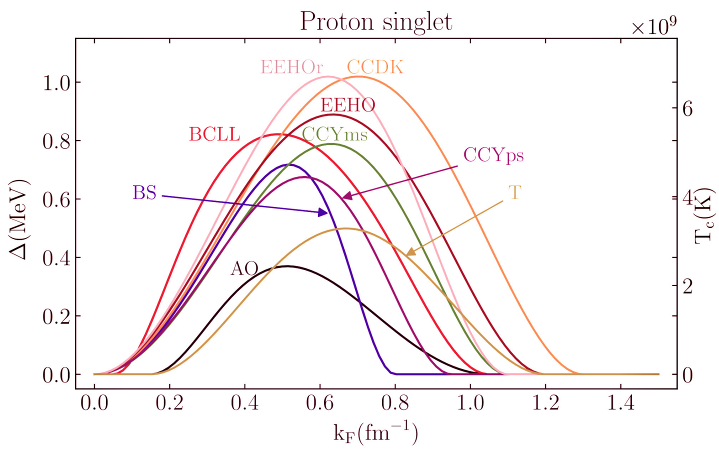

Figure 4: Energy gap (Δ) and critical temperature (T_c) as a function of proton Fermi momenta for all proton superconductivity gap models investigated in this work.

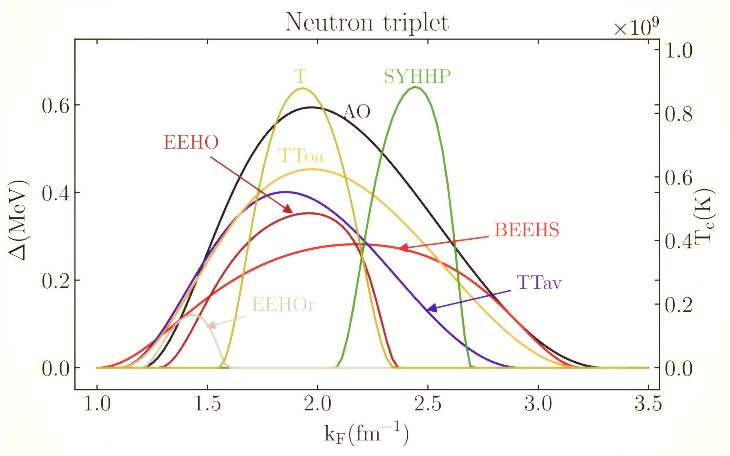

Figure 5: Energy gap (Δ) and critical temperature (T_c) as a function of neutron Fermi momenta for all neutron superfluidity gap models investigated in this work.

$$
\begin{aligned}
\epsilon(p) &= \epsilon_{\text{nucleonic}}(p),\ p < \mathrm{p}_{\text{trans}}, \\
\epsilon(p) &= \epsilon_{\text{nucleonic}}(\mathrm{p}_{\text{trans}}) + \Delta\epsilon + \mathrm{c}_{\mathrm{s}}^{-2}(p - \mathrm{p}_{\text{trans}}),\ p \geq \mathrm{p}_{\text{trans}},
\end{aligned} \tag{3.8}
$$

and number density, by

$$
\begin{aligned}
n(p) &= n_{\text{nucleonic}}(p),\ p < \mathrm{p}_{\text{trans}}, \\
n(p) &= n_t \sqrt{\frac{\epsilon(p) + p}{\epsilon_{\text{nucleonic}}(p_{\text{trans}}) + p_{\text{trans}}}},\ p \geq \mathrm{p}_{\text{trans}}, \\
\text{where } n_t &= \frac{(p_{\text{trans}} + \epsilon_{\text{nucleonic}}(p_{\text{trans}}) + \Delta\epsilon)\, n_{\text{nucleonic}}(p_{\text{trans}})}{p_{\text{trans}} + \epsilon_{\text{nucleonic}}(p_{\text{trans}})}.
\end{aligned} \tag{3.9}
$$

The parameters of transition pressure $(\mathrm{p}_{\text{trans}})$, energy jump $(\Delta\epsilon)$ and speed of sound $(\mathrm{c}_{\mathrm{s}})$ are free to adjust. Following [91, 92], I take $\mathrm{c}_{\mathrm{s}} = c$ to explore the maximum number of possible hybrid equations of state compatible with astrophysical observations, but this value tends to be smaller for quark EOS, some examples shown in [27]. A Maxwell construction is used to build the phase transition, so the pressure is continuous, but the equations above predict a jump both in energy density and number density at the transition. The size of typical energy density jumps considered for the hybrid EOS investigated in this work is illustrated in Figure 6.

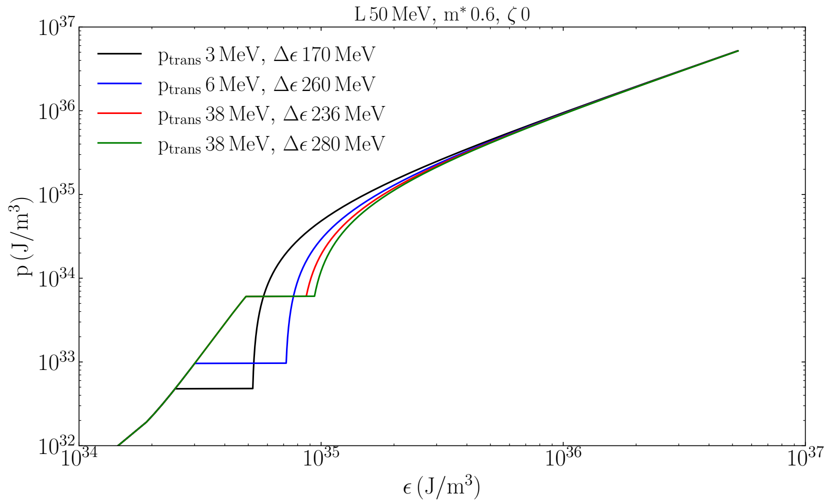

Figure 6: Pressure and energy density (in J/m^3) of all hybrid EOS built with nucleonic EOS L 50 MeV, m^* 0.60, ζ 0. Curves of different colors represent different phase transition pressures and energy density jumps $\Delta\epsilon$.

This parametrization does not offer estimates for microphysical quantities in the quark phase, such as electron fractions or quark masses, so, for consistency with the quark dUrca emissivity used in the next chapters, I make some assumptions. I take that there are only up and down quarks in the quark phase, whose masses are small enough not to affect the quark emissivity, and the electron fraction $Y_e = 10^{-5}$. I also estimate the strong coupling constant to be $\alpha = 0.12$, unchanging with density.

3.3.1 *Phase transition construction*

The nucleonic equations of state used as a base to the hybrid EOS are identified by their slope of symmetry energy, L, effective masses $m^* = m_{\text{Dirac}\,n,p}/m_{\text{vacuum}\,n,\,p}$ and ζ. The parameter ζ controls the nucleonic EOS at large densities and the maximum mass of neutron stars has been proven very sensitive to it [93], thus, I hypothesized it would also be relevant to the quark phase transitions. To include a diverse set of nucleonic EOS, I worked with combinations of relatively small and large L of 50 and 90 MeV, two possible effective masses m^*, 0.55 and 0.60, and two values of ζ, 0 and 0.02. The mass-radius diagrams for all of the possible EOS built with those parameters are shown in Figure 7. Henceforth, specific hybrid EOS will be identified by the values of the nucleonic EOS

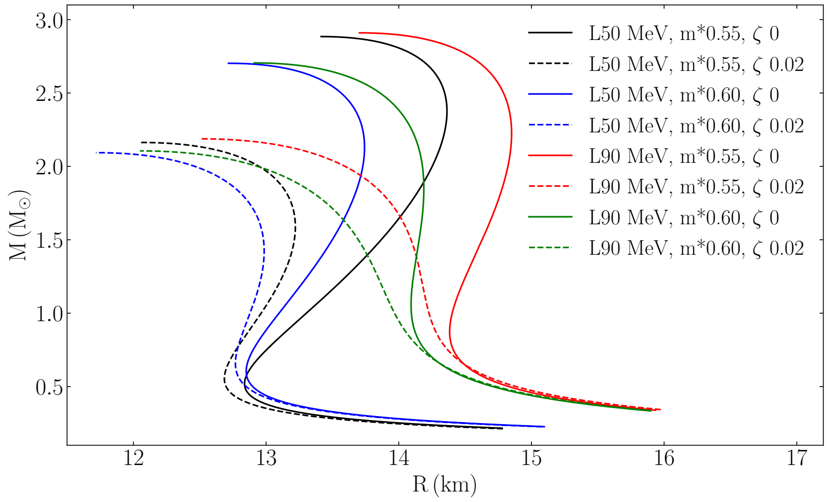

Figure 7: Mass-radius curves of several nucleonic EOS. Dashed lines represent EOS with $\zeta = 0.02$.

parameters, L, m^* and ζ, and the phase transition parameters p_{trans} and $\Delta\epsilon$, for example, the hybrid EOS L 50 MeV, m^* 0.60, ζ 0, p_{trans} 6 MeV, $\Delta\epsilon$ 260 MeV.

I chose four of those nucleonic equations of state to build quark phase transitions. They are: L 50 MeV, m^* 0.60, ζ 0; L 50 MeV, m^* 0.60, ζ 0.02; L 90 MeV, m^* 0.55, ζ 0.02 and L 90 MeV, m^* 0.60, ζ 0.02. They were chosen so that by comparing them in pairs, I can check the effect of a given parameter on the results of the cooling calculations.

To obtain the values of p_{trans} and $\Delta\epsilon$ compatible with all astrophysical data constraints, I create the diagrams of Figures 8, 9, 10 and 11, using the contours provided by [92]. They illustrate the regions on the p_{trans} versus $\Delta\epsilon$ diagrams resulting in neutron stars that fit the observed GW170817 tidal deformability (in blue), mass and radius NICER contours (in green) and whose maximal mass is at least of 2 M$_\odot$ (in red). They also indicate which combinations of p_{trans} and $\Delta\epsilon$ result in compact stars with mass-radius curves that include twin stars (in grey). Note that the color contours often overlay one another, darkening the tones of the colors one observes.

Twin stars are neutron stars whose mass-radius curve presents two branches, so that stars with same mass but different radii are possible. This phenomenon signals a phase transition, however not all neutron stars with phase transitions manifest it [2]. An example of mass-radius curves for twin stars is shown in Figure 12, for hybrid EOS built from nucleonic L 50 MeV, m^* 0.60, ζ 0 EOS.

In this research I focus on hybrid stars that are also twin stars because of the increasing possibilities of detecting them, as discussed in [94]. Furthermore, forcing the existence of

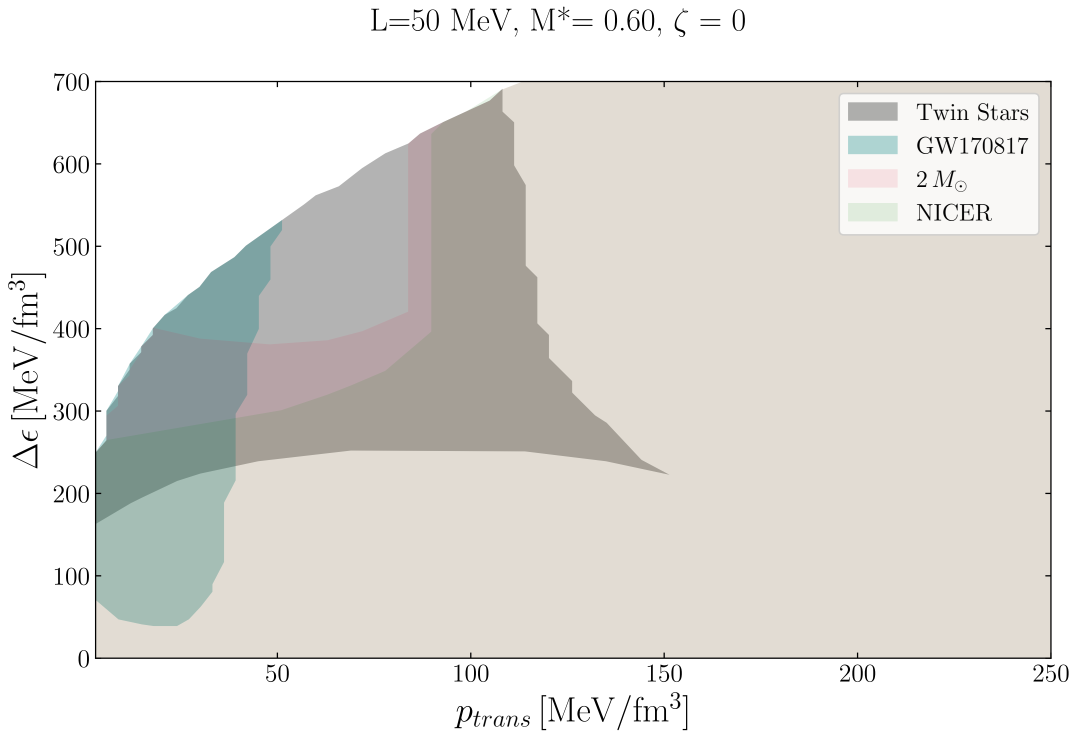

Figure 8: Pressure and energy jump at the phase transition for hybrid twin stars compatible with astrophysical constraints, built with L 50 MeV, m^* 0.60, ζ 0 nucleonic EOS.

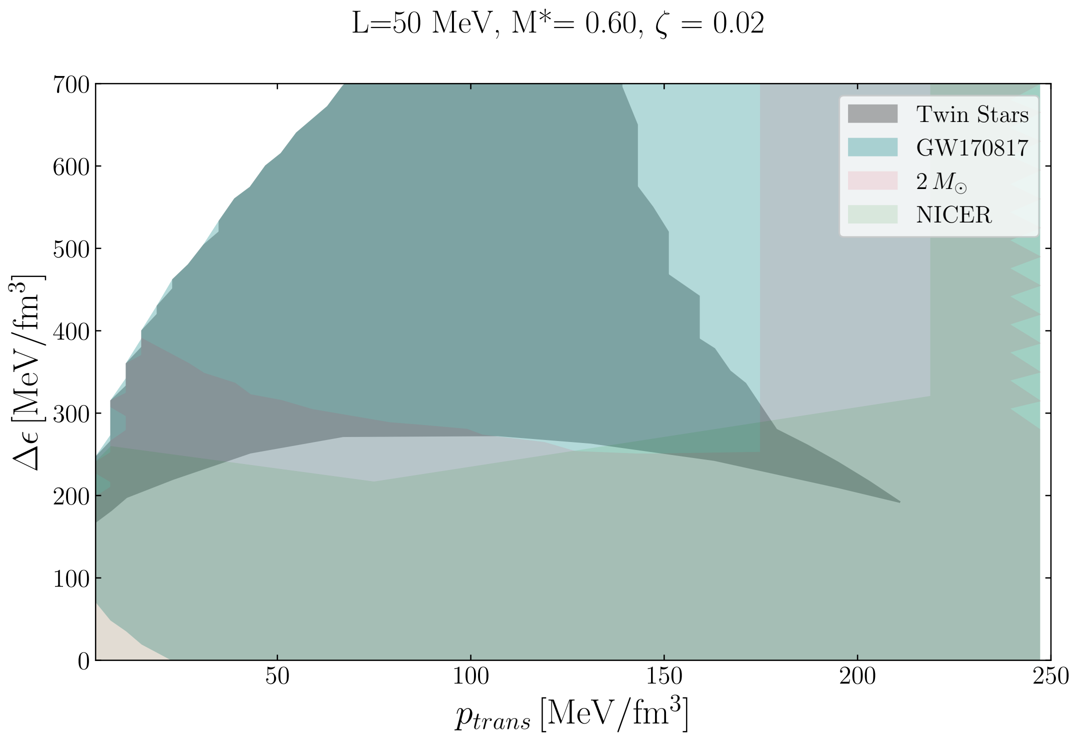

Figure 9: Same as 8, but for hybrid stars built with L 50 MeV, m^* 0.60, ζ 0.02.

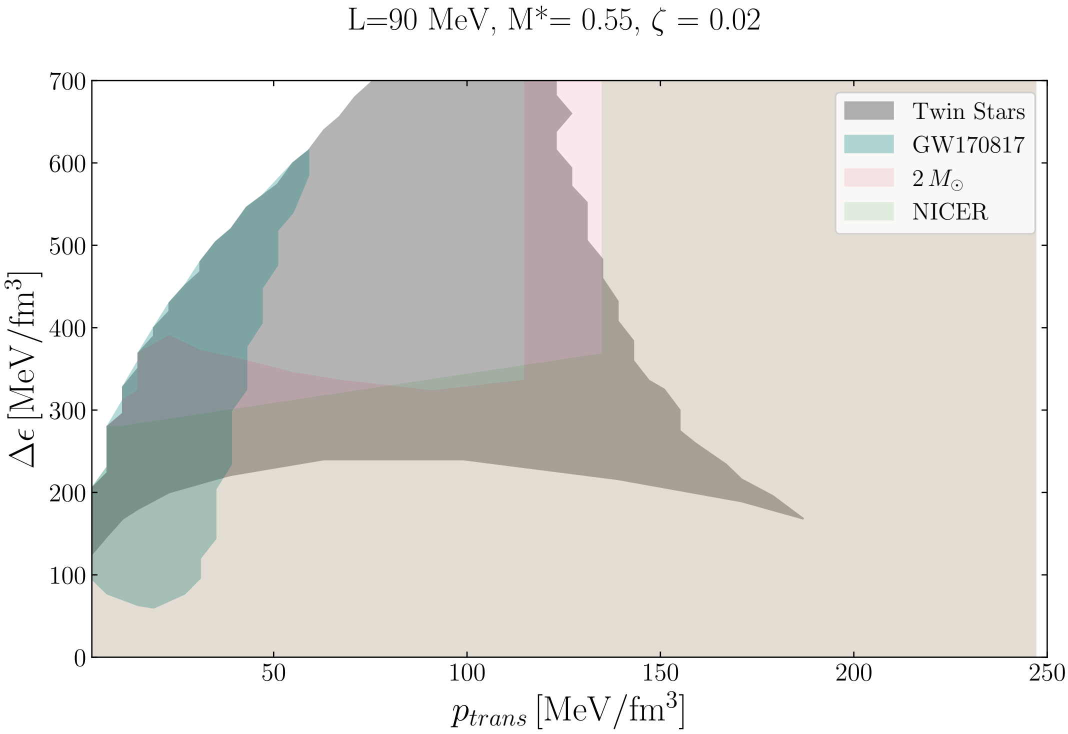

Figure 10: Same as 8, but for hybrid stars built with L 90 MeV, m^* 0.55, ζ 0.02.

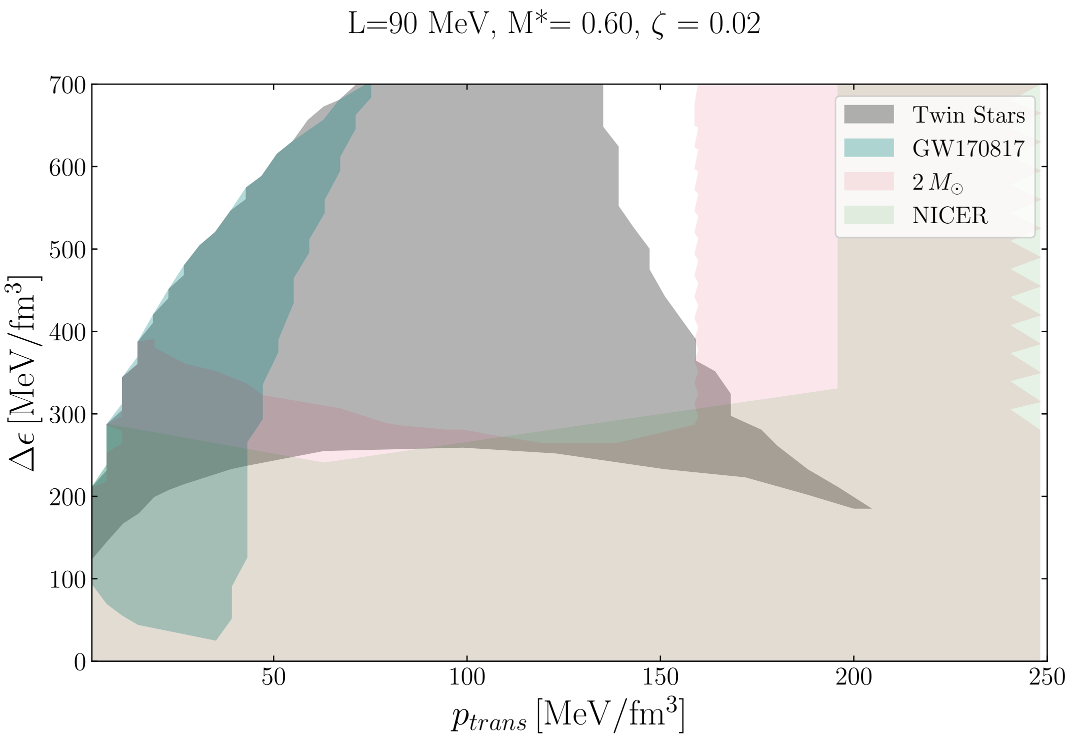

Figure 11: Same as 8, but for hybrid stars built with L 90 MeV, m^* 0.60, ζ 0.02.

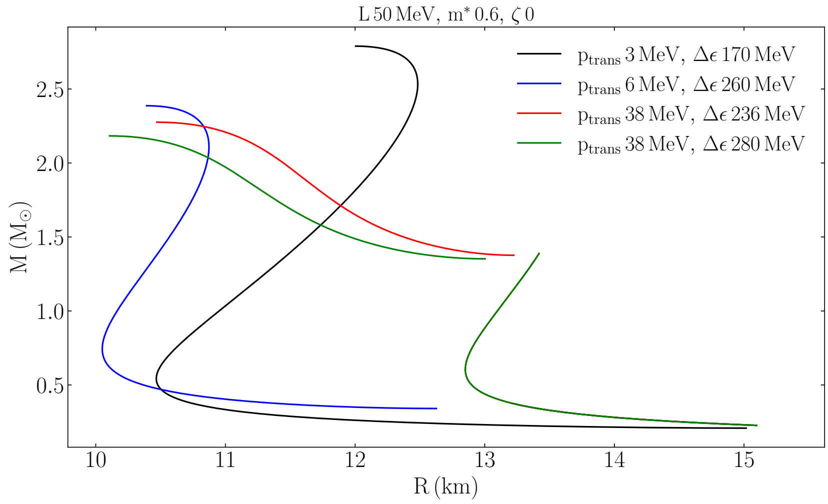

Figure 12: Mass-radius curves of all hybrid stars built with L 50 MeV, m^* 0.60, ζ 0 nucleonic EOS. Different colors represent different phase transition parameters.

twin stars is not the most restricting constraint for most EOS investigated here. Instead, it is the tidal deformability measured by GW170817, which strongly limits the transition pressure values. Thus, relaxing the twin star requirement would not significantly increase the transition densities of the hybrid stars, except for the L 50 MeV, m^* 0.60, ζ 0.02 EOS, whose larger phase transitions are already disfavored because of the cooling calculation results, as will be discussed in Chapter 5.

To probe the widest possible range of phase transition densities, which are determined by the value of p_{trans}, I choose the smallest and largest transition pressures overlapping all areas in the diagrams of Figures 8, 9, 10 and 11. For the largest density phase transition of L 50 MeV, m^* 0.60, ζ 0 I also varied the value of $\Delta\epsilon$. For most EOS I could build phase transitions compatible with all astrophysical constraints going from n_{sat} to around $2\,n_{\text{sat}}$. The L 50 MeV, m^* 0.60, ζ 0.02 EOS, that has the lowest maximum mass of all nucleonic equations of state, allowed larger phase transition densities, up to around $4\,n_{\text{sat}}$.

3.3.2 *Code implementation*

To incorporate the hybrid equations of state in the code, I initially proceed as detailed in section 3.1.1, and concatenate the nucleonic core part of the EOS with its crust part. I use the same crust EOS as before. The quark part of the equation of state is analytically calculated, given a large enough range of pressure values. To solve the TOV equations, I repeat the procedure described in Chapter 2, making sure I work with a linear interpolation of the table of points describing the equation of state, instead of the points themselves, to facilitate the numerical convergence of the TOV results. This interpolation is performed as explained in section 3.1.1.

Then, I calculate the mass-radius curve for each hybrid EOS and find their maximum mass. Twin stars present an unstable region between the two mass-radius branches. The unstable stars are easily identified by following the trend of mass increase with central pressure, that is, hybrid stars with reducing masses for increasing central pressures are unstable and should be removed from the calculations. The maximum mass hybrid star will be found similarly, by increasing the central pressure in small increments until the total mass decreases. The last hybrid star in the second branch whose mass increased with central pressure is the maximum mass star. I perform this calculation by solving the TOV equations multiple times for 1200 central pressures, increasing from $5 \times 10^{32}\,\mathrm{J/m^3}$ up to $5 \times 10^{37}\,\mathrm{J/m^3}$, or until the maximum pressure is reached.

Finally, when calculating the neutrino luminosities of hybrid stars, I note that a Maxwell phase transition implies that there is no quark-hadron mixed phase. Thus, nucleonic dUrca cooling will only happen at the star's nucleonic core and quark dUrca cooling, at the star's quark core, such that the two cooling processes will not be simultaneously active. To incorporate this restriction in the cooling code, I included an if clause that sets the dUrca emissivities to zero outside their regions of influence, determined by limit densities. I define that the quark emissivity is not zero at $n_{\mathrm{trans}} \leq n \leq n_0$ and the nucleonic emissivity is not zero within the core, that is, at densities $0.8 - 0.5\, n_{\mathrm{sat}} \leq n < n_{\mathrm{trans}}$, depending on the smoothness of the transition between the nucleonic core EOS and the crust EOS and above the dUrca threshold.

Part III

NEUTRON STAR NEUTRINO LUMINOSITIES

With the theoretical framework described previously, we calculate the predicted masses and heat capacities for the cold neutron stars under study. We investigate nucleonic and hybrid equations of state.

4

NEUTRON STAR COOLING WITH NUCLEONIC EQUATIONS OF STATE

In this chapter, I present the results of cooling calculations, in which I simulate direct Urca fast-cooling processes in the neutron star core to reproduce the inferred neutrino luminosities of cold neutron stars MXB 1659-29 and SAX J1808.4-3658. Their most likely effective temperature T_e^∞, envelope composition and neutrino luminosity have already been described in Chapter 2, but for easy reference, are repeated here: for MXB 1659-29, I assume $T_e^\infty = 55$ eV, light element envelope composition and $L_\nu = 3.9^{+4}_{-2} \times 10^{27}$ J/s. For SAX J1808.4-3658, $T_e^\infty = 36^{+4}_{-8}$ eV, light and heavy element envelope composition are both possible and $L_\nu = (1 \times 10^{25} - 1 \times 10^{26})$ J/s.

I start by disregarding the existence of nuclear pairing in section 4.1. In this simplified scenario, I also discuss the percentage of core volume undergoing direct Urca processes for all neutron stars with the expected neutrino luminosity above. Then, I investigate how nuclear pairing affects those results. For ease of interpretation, I consider proton superconductivity and neutron superfluidity individually in section 4.2, then simultaneously in section 4.3, and I simulate less efficient fast-cooling processes in the no-pairing and both-pairings scenarios in section 4.4.

4.1 NO NUCLEAR PAIRING

I calculate the dUrca neutrino luminosity for neutron stars with all of the EOS of the FSUGold2 family under study with $\zeta = 0.0256$, described in Chapter 3, which are henceforth identified with the value of their symmetry energy slope parameter L. For each EOS, I build neutron stars with different masses by varying their central pressures between $p_0 = 1 \times 10^{33}$ J/m^3 and the maximum pressure $p_{\max}$, which still leads to a stable neutron star and determines the maximum mass m_{max} allowed by that EOS. Figure 13 illustrates that procedure with the vertical green points indicating the total mass (left) and central number density (right) of each neutron star considered in one of those calculations, for the $L66$ EOS. With this procedure I can obtain a general picture of the total neutrino luminosity and heat capacity as a function of neutron star mass and volume. Later, to find the neutron star with the specific inferred neutrino luminosity of each source, I solve an optimization problem which returns the corresponding central pressure of the searched neutron star. I use the already integrated Scipy routine optimize.brentq [42, 95], that finds a function's root with Brent's method, with an absolute error of $2 \times 10^{-12}\,\text{J}/\text{m}^3$ and relative error of 8.9×10^{-16}.

When I vary the central pressure to obtain a general picture of the properties of several neutron stars, I also include those that lie below the direct Urca threshold, indicated by the orange line in Figure 13. These stars have $L_\nu = 0\,\text{J/s}$ in this simplified framework that does not include slow cooling processes such as modified Urca reactions. Hence, I do not use them to investigate neutrino luminosity, but only heat capacity. Some of the neutron stars considered lie below the threshold of minimum neutron star mass ever observed, $M_{\text{min}} \approx \text{M}_\odot$ [14], a value also consistent with smallest neutron star mass obtained in core-collapse supernova simulations, around $M_{\text{min}} \approx 1.2\,\text{M}_\odot$ [96]. Thus, even though I assume neutron stars with masses smaller than solar mass are likely unrealistic, I display those results for completeness.

Neutron star dUrca neutrino luminosity curves for three EOS are shown in Figure 14, where effective temperature $T_e^\infty = 55$ eV. Lower L EOS present a smaller range of neutron star masses in that Figure because their direct Urca thresholds are obtained at larger central densities, that is, within heavier neutron stars. Therefore, for the $L48$ EOS, only neutron stars with masses $M \geq 1.85\,\text{M}_\odot$ have fast-cooling processes, whereas for the $L105$ EOS, that is the case for all sources with masses $M \geq 0.8\,\text{M}_\odot$. For intermediate L EOS, the dUrca threshold lies between these extremes, which is the case of the $L69$ EOS, for which all neutron stars with masses above $M \approx 1.4\,\text{M}_\odot$ will cool fast. This trend would suggest that neutron star cooling observations favour small L EOS, because both intermediate and large L ones predict high neutrino luminosity for most neutron stars, thus they would have difficulties reproducing the low neutrino luminosities of hot

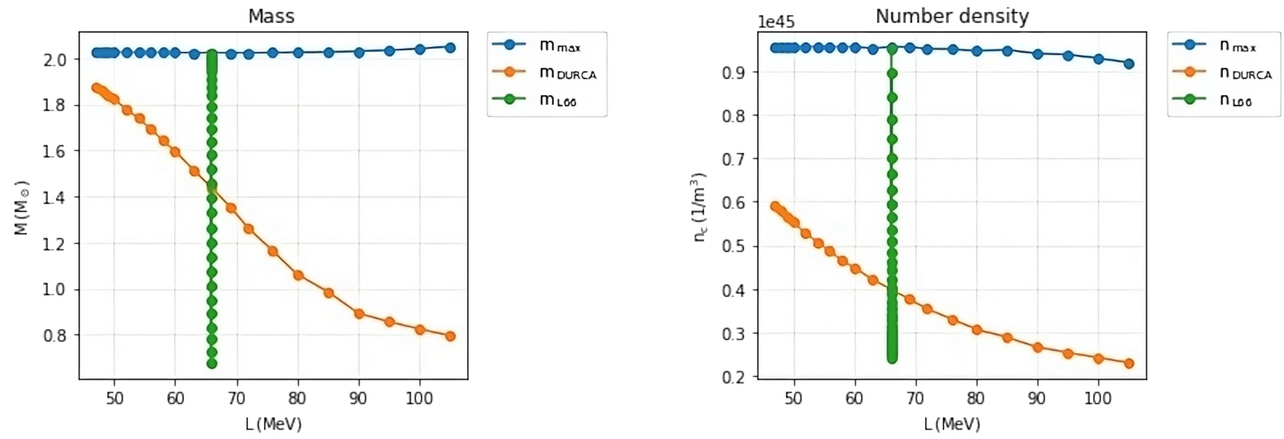

Figure 13: Total masses (left) and central number densities (right) of neutron stars investigated, for *L*66 EOS (green vertical points). The EOS dUrca thresholds are represented by the orange curves and the maximum values of mass and central densities, by the blue curves.

neutron stars, expected to cool slowly. The inclusion of nuclear pairing, to be discussed in sections 4.2 and 4.3, changes this conclusion. In Figure 14, the horizontal black line is a reference to the approximate location of the most likely inferred neutrino luminosity for source MXB 1659-29. That value is on the lower end of the neutrino luminosity curves for all EOS, indicating it is close to the dUrca threshold. A color map plot of neutrino luminosities for all EOS under study and same effective temperature is shown in Figure 15. This type of plot presents a good visualization scheme for the order of magnitude of the calculated dUrca neutrino luminosities in the no-pairing case and how, usually, they are much larger than the values inferred for the sources under study, that are closer to the regions in shades of blue.

By solving the optimization problem to find exactly which neutron stars present the MXB 1659-29 inferred neutrino luminosity, I obtain Figure 16. The solid blue line represents the neutron stars with the required luminosity and their corresponding total masses. The light blue shadow around that line encompasses the lower and upper limits of inferred neutrino luminosity for that source. In the lower plot, one can see the percentage of the core volume under direct Urca processes, which goes from approximately 0.1 to 0.2% for $L\,47$ EOS and from 0.7 to 2.5% for $L\,112$ MeV, at most, in agreement with the predictions of the authors of [29], who have estimated a value of 1% for that quantity. This number illustrates the cooling efficiency of direct Urca processes and suggests that

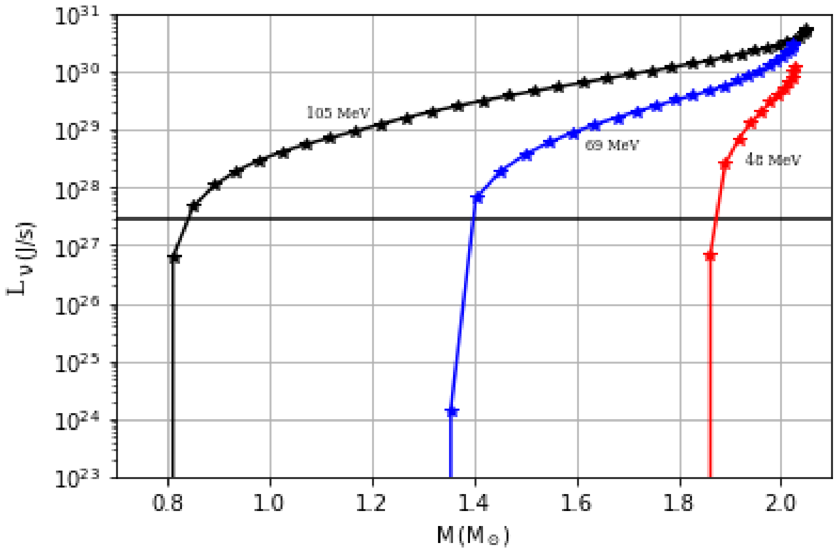

Figure 14: Total neutrino luminosity versus total mass for the EOS with $L48$ (red), $L69$ (blue) and $L105$ (black). The horizontal black line marks the approximate value of the most likely neutrino luminosity for MXB 1659-29.

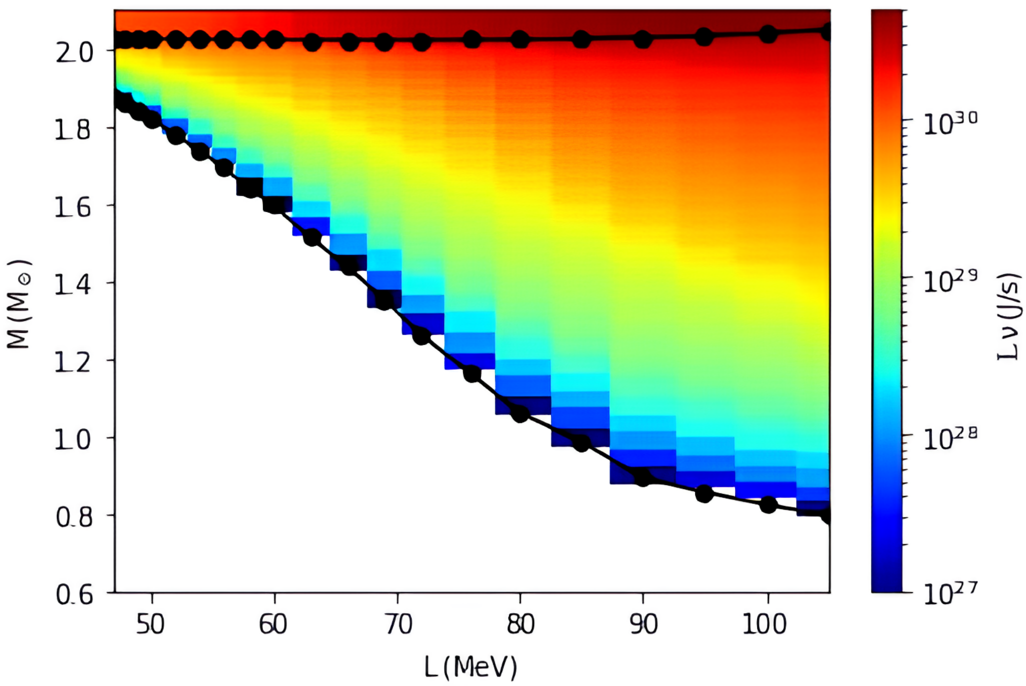

Figure 15: Color map of total neutrino luminosity as a function of the total mass and L for all the EOS under analysis. The dUrca threshold is the black curve on the bottom and the maximum mass curve, the one on the top.

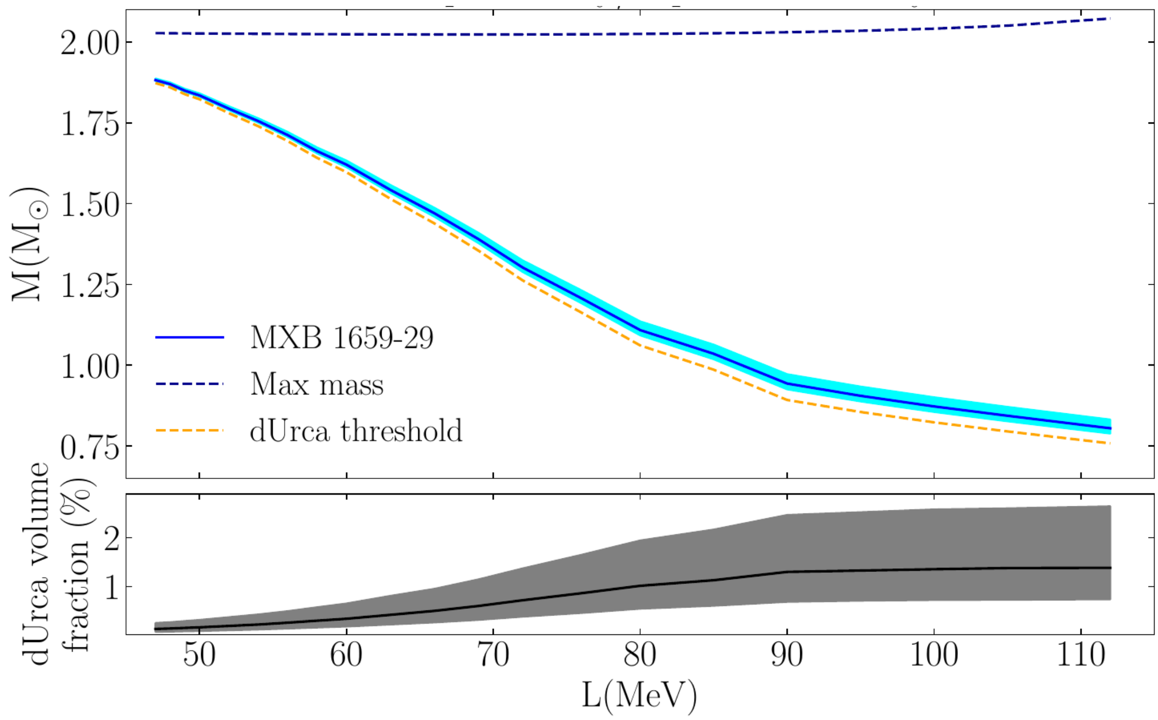

Figure 16: (Upper plot) Total masses of the neutron stars with the inferred neutrino luminosity of MXB 1659-29 as a function of L. The solid blue line represents the most likely value of the mass and the blue region around it, its 1σ lower and upper limits. The dashed orange line on the bottom is the dUrca threshold and the dashed blue line on the top is the maximum mass. (Bottom plot) Percentage of core volume under direct Urca reactions for the neutron stars displayed above.

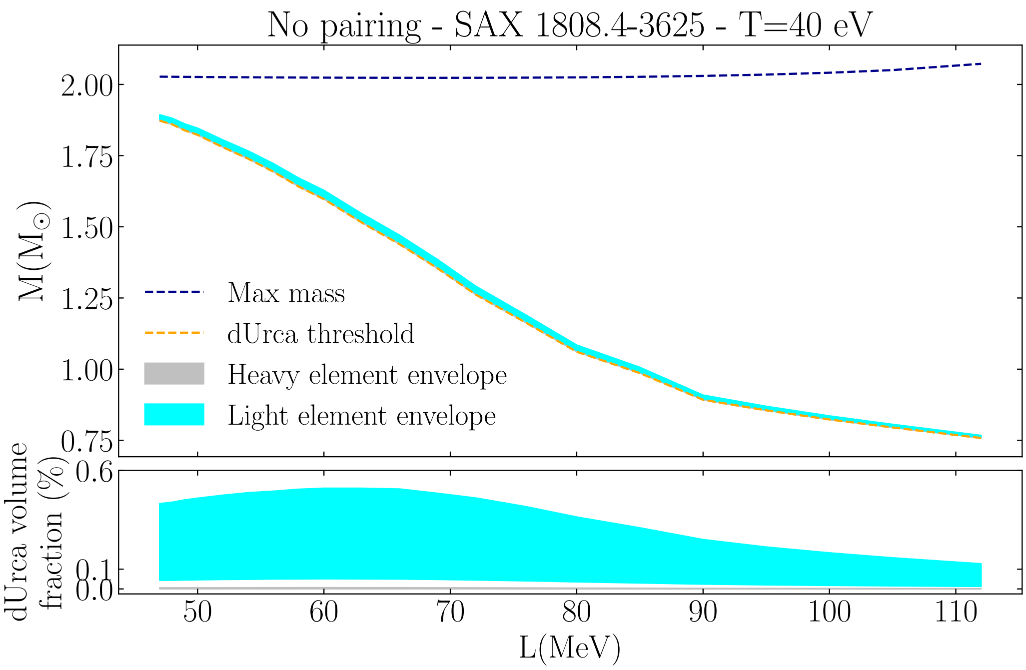

Figure 17: (Upper plot) Total masses of the neutron stars with the inferred neutrino luminosity of SAX J1808.4-3658 for all EOS under study, assuming $T_e^\infty = 40$ eV. The blue area encompasses the lower and upper limits of its most likely inferred neutrino luminosity with light element envelope, whereas the gray area shows the same results for heavy element envelope. The dashed orange line on the bottom is the dUrca threshold and the dashed blue line on the top is the maximum mass. (Bottom plot) Percentage of core volume undergoing direct Urca reactions for the neutron stars displayed above. Blue area assumes light element envelope composition and gray, heavy element composition.

even lower surface luminosities would be attainable to those EOS, with larger volume fractions under dUrca processes.

To check whether colder neutron stars are reproducible with larger dUrca volume fractions, I investigate the neutron star in the binary system SAX J1808.4-3658. The plots on Figures 17, 18 and 19 show the predicted masses of neutron stars with this source's inferred neutrino luminosity for all EOS, considering the upper limit, most likely value and lower limit of temperature, respectively. In all cases, I investigated two scenarios of envelope composition and I display the percentage of core volume under dUrca processes on the lower part of the Figure. Similarly to the MXB 1659-29 case, the neutron stars with the inferred luminosity lie very close to the dUrca threshold, except when $T_e^\infty = 28$ eV, with light element envelope. For all temperatures, a heavy element envelope, although able to reproduce the searched luminosity, seems unlikely to be the best

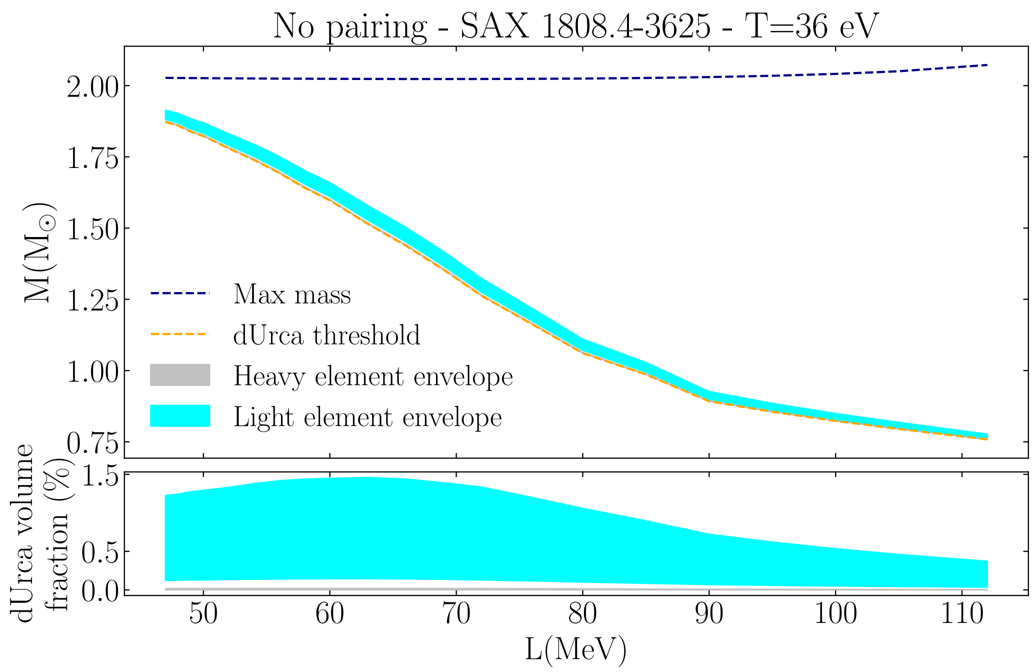

Figure 18: Same as figure 17, but for $T_e^\infty = 36$ eV.

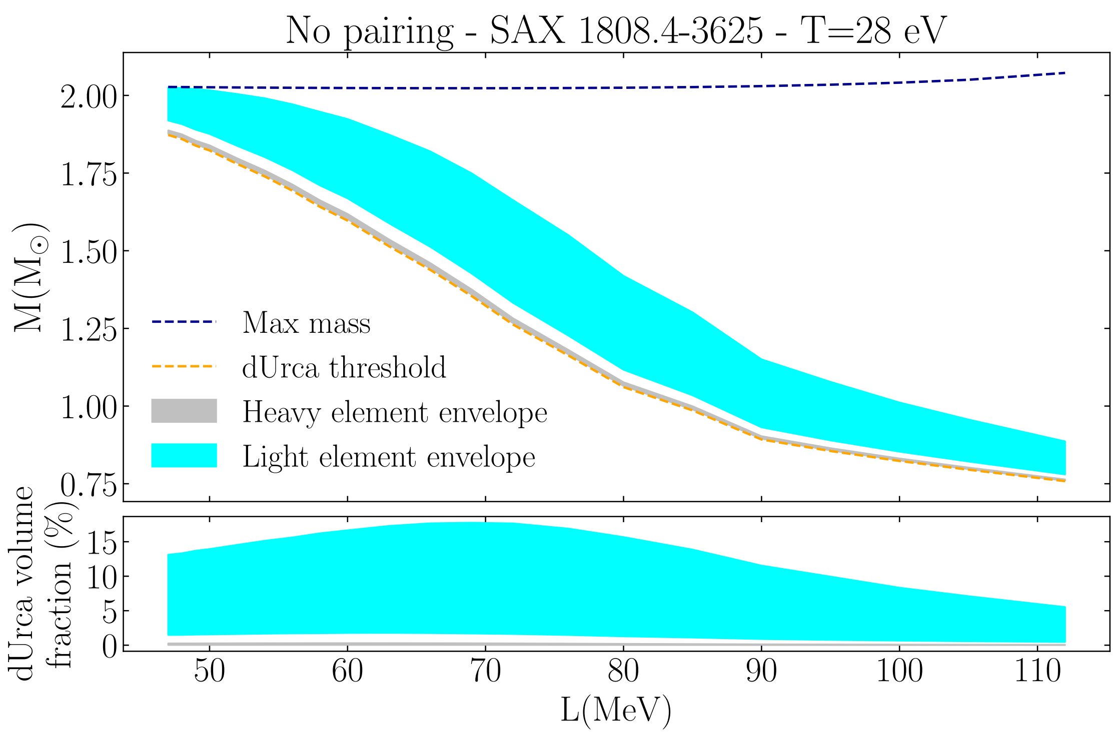

Figure 19: Same as figure 17, but for $T_e^\infty = 28$ eV.

fit for this source, because it consistently predicts a very tiny dUrca core volume fraction and mass range for a relatively large variation of neutrino luminosity, of one order of magnitude: $L_\nu = (1 \times 10^{25} - 1 \times 10^{26})$ J/s. In other words, it seems unrealistic that all neutron stars within this neutrino luminosity range would have masses so close to one another. Arguably, the range of possible values of neutrino luminosity range over many orders of magnitude

The heat capacity of the neutron stars under study has also been investigated. To all neutron stars with $T_e^\infty = 55$ eV, that generated neutrino luminosity plot in Figure 15, their corresponding heat capacities are displayed in Figure 20, where the black dotted line marks the maximum masses for each EOS. With the calculated heat capacities and dUrca neutrino luminosities for neutron stars with a given effective temperature, one can verify the predictions of expression 2.39 to check whether a measurement of temperature variation during quiescence would discriminate between EOS. In Figure 21, the diagonal lines correspond to surface temperature variations due to neutrino cooling over a decade in quiescence, $\Delta T/T$, of 1% and 16%, whereas the horizontal lines are the values of heat capacity against neutrino luminosity for $L47$ and $L105$ EOS. Therefore, in the no-pairing scenario, and trusting the neutrino luminosities for MXB 1659-29 are $L_\nu = 3.9^{+4}_{-2} \times 10^{27}$ J/s, marked by the vertical shaded region, temperature variations larger than 1% in the quiescence time interval of 10 years would not be consistent with the EOS investigated. This conclusion was obtained by noting that, in Figure 21, the horizontal lines representing the EOS calculations only intersect with the $\Delta T/T = 1\%$ diagonal lines within the shaded region representing the inferred neutrino luminosities. In other words, those EOS are only able to simultaneously produce those luminosities and reduce the temperature by 1% or less in that time interval, at least without nuclear pairing. If the temperature variation in this time frame is smaller than 1%, it could indicate that this neutron star EOS has a small L or it could be evidence for strong nuclear pairing, as will be seen in the next section.

Overall, all EOS are compatible with both MXB 1659-29 and SAX J1808.4-3658 inferred neutrino luminosities. Furthermore, I verified the claim that around 1% of the core volume supports dUrca processes for neutron stars with MXB 1659-29's neutrino luminosity, using realistic EOS without nuclear pairing, and I showed how expression 2.39

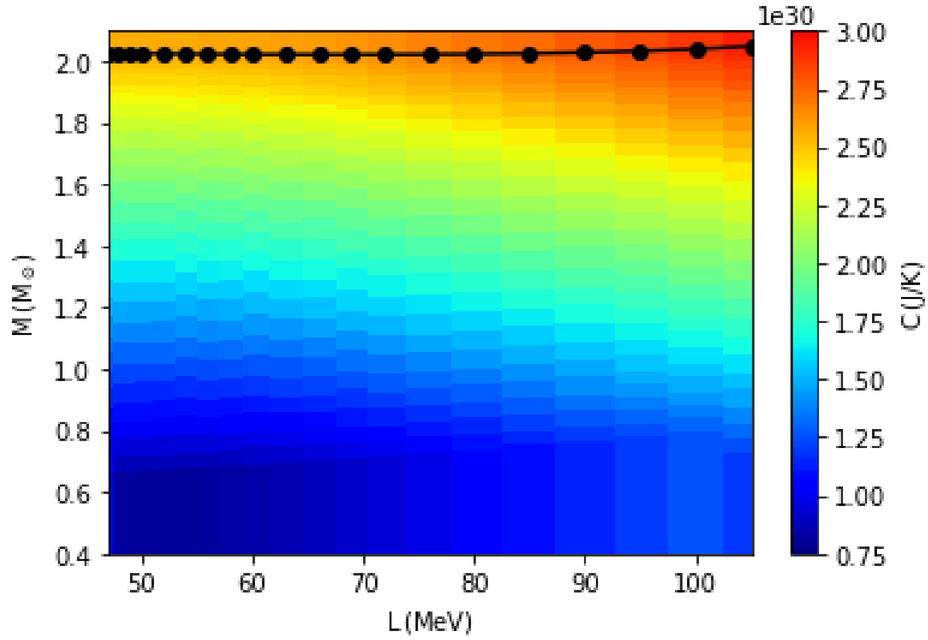

Figure 20: Color map of total heat capacity versus total mass for all the EOS under analysis. The maximum masses are represented by the black line on the top.

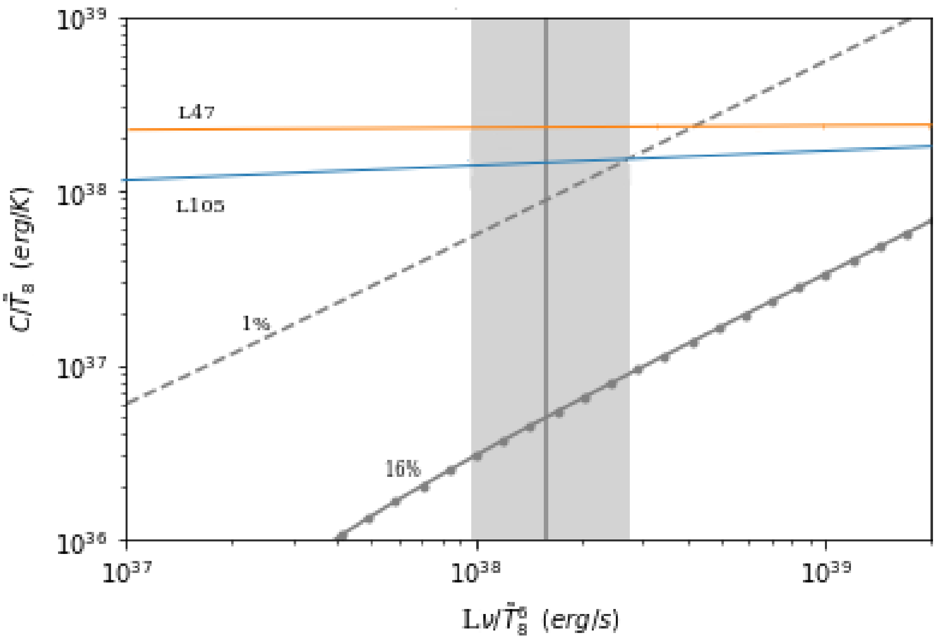

Figure 21: Total heat capacity divided by the normalization factor $\tilde{T}_8 = \tilde{T}/10^8\,K$ versus the normalized neutrino luminosity for all neutron stars created by $L47$ (orange curve) and $L105$ EOS (blue curve). Predictions of expression 2.39 for $\Delta T/T = 1\%$ (dashed line) and $\Delta T/T = 16\%$ (dashed dotted line) are also shown. The vertical grey line represents the most likely neutrino luminosity for MXB 1659-29 and the grey area around it, its $1\,\sigma$ lower and upper limits.

can be useful in discriminating between EOS, with a measurement of temperature variation for transiently-accreting neutron stars in quiescence. Nonetheless, given the very small range of predicted masses obtained in these calculations, I found this scenario unrealistic. In the next section, I include neutron and proton pairings to see their effect in the cooling calculation.

4.2 INDIVIDUAL PROTON OR NEUTRON NUCLEAR PAIRING

As explained in Chapter 2, nuclear pairing reduces the heat capacities and the efficiency of direct Urca reactions, therefore reducing the neutrino luminosities of the neutron stars under superfluidity or superconductivity. These reduction rates are a function of the critical temperatures of each gap model, which, according to the gap model parametrization described in Chapter 3, depend on the EOS number densities. Therefore, in reproducing the neutrino luminosities of MXB 1659-29 and SAX J1808.4-3658, with superfluid or superconducting matter within neutron stars, it is crucial to know the opening and closing densities of their gap models for each EOS, that is, the densities where the neutron star interior temperature is smaller than the critical temperature of the gap, thus, the nuclear pairing channel is active. In this section, I search for neutron stars with MXB 1659-29's neutrino luminosity assuming either neutron or proton nuclear pairing models are active. A more realistic scenario would consider both pairings simultaneously, but I use this approximation as a preliminary study on the characteristics of the nuclear pairing models. The calculations for SAX J1808.4-3658 neutrino luminosities are reserved for section 4.3.

In Figure 22, all gap model critical temperatures for $L95$ EOS in a neutron star with $M = 1.48\,\mathrm{M}_{\odot}$ are shown. I study the formation of nuclear Cooper pairs only in the core of neutron stars, thus, the densities represented in that Figure correspond to the core densities only, where the highest value of number density is the central n, where $n(0) = \mathrm{n}_0$. Some of the gap models open and close for densities lower than the dUrca threshold, for example, NT EEHOr, thus they do not impact on the calculation of the neutrino luminosity. Those gap models are said to have "early openings and closings". On the other hand, there are gap models with "late openings", such as NT SYHHP in

Figure 22, whose critical temperature becomes larger than the neutron star's interior temperature for densities larger than the dUrca threshold. Those kind of gap models may reduce the neutrino luminosity of heavier neutron stars while leaving lighter neutron stars' luminosities unaffected. For example, for the EOS represented in Figure 22, neutron stars with central number density $n = 2\,n_{\rm sat}$ would not present NT SYHHP P_2^3 neutron pairing. It is also useful to define the "strength" of a gap model, that is, how much a pairing model will reduce a neutron star's heat capacity and neutrino luminosity in comparison to the not-paired case. In this work, I consider gap models that are active in most of the neutron star volume as "strong" gap models, that is, I quantify the influence of a given gap model based on the width rather than the amplitude of its critical temperature curve as shown in Figure 23. Hence, when comparing proton superconductivity and neutron superfluidity gap models, the latter are stronger, especially NT BEEHS, NT TTav, NT TToa and NT AO. In the literature, the strength of a gap model is a combination of its width and amplitude, but for the very cold neutron stars studied here, with $T_e^\infty \approx 3 - 6 \times 10^5$ K $\approx$ central temperature $T_c \approx 10^6 - 10^7$ K, I observed that $\tau = T/T_c$ quickly approaches zero except around the gap model's opening and closing densities, thus the gap model width is the determinant factor of its strength.

Nuclear pairing gap models openings and closings for all EOS can be summarized in plots such as the one in Figure 23. I represent, for each EOS, its dUrca threshold (yellow dashed curve) and maximum mass (blue dashed curve) as well as the corresponding neutron star masses at which the proton and neutron gap models close, shown respectively in dashed and solid colorful curves, for all neutron stars' effective temperature $T_e^\infty = 55$ eV. Not all gap models are present in that Figure because either they are only active for very low neutron star masses, $M \leq \mathrm{M}_\odot$, which is the case for PS BS, PS CCYps and NT EEHOr, thus they will not affect the neutrino luminosity or heat capacity calculations much, or they are active for all the volume of all neutron stars, such as NT AO, NT TTOA and NT BEEHS. One advantage of representing gap models opening and closing curves as in Figure 23 is that one can easily see the range of neutron star masses that will be affected by each nuclear pairing. For example, for neutron superfluidity gap model NT EEHO and $L \leq 55$ EOS, all neutron stars with total mass $M \leq 1.75\,\mathrm{M}_\odot$ will be superfluid, but because these stars did not reach dUrca threshold, nuclear pairing

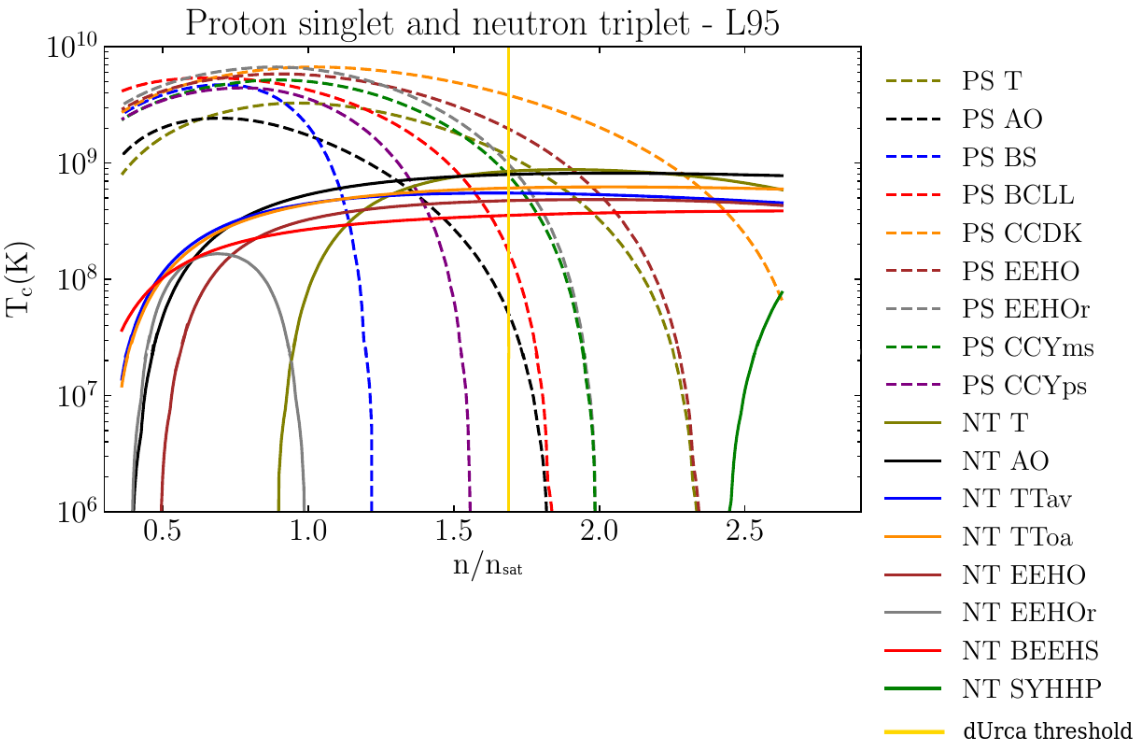

Figure 22: Critical temperature curves of all nuclear pairing gap models as a function of number density normalized by saturation density n_{sat}, for a neutron star with $M = 1.48\,\mathrm{M}_{\odot}$ and $L95$ EOS. All proton superconductivity gap models are displayed with dashed lines and neutron superfluidity ones, with solid lines. The vertical yellow line marks the dUrca threshold.

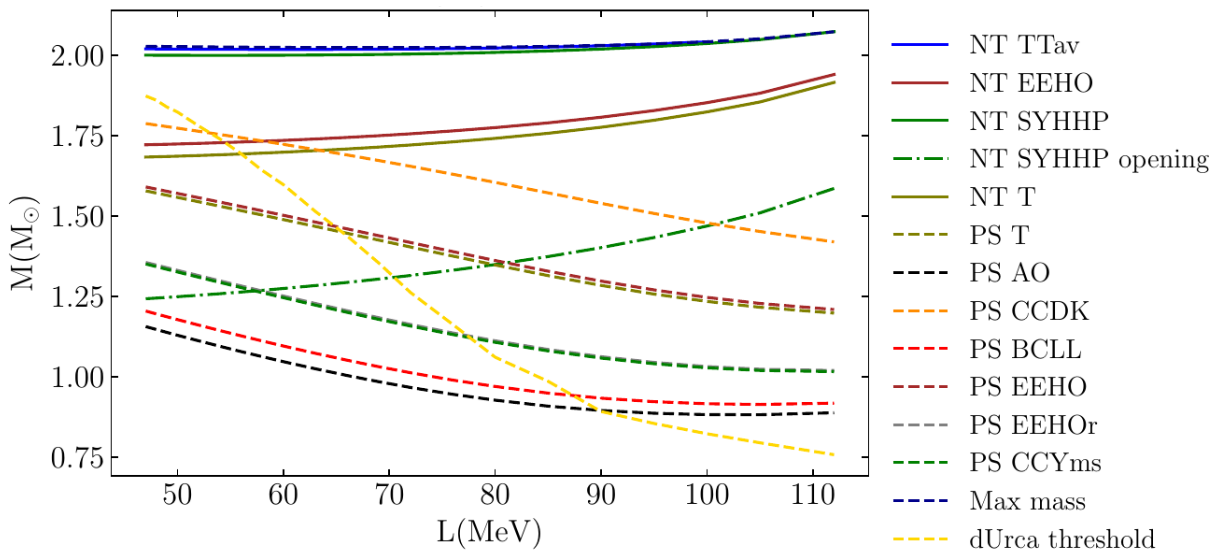

Figure 23: Nuclear pairing closing curves for each EOS as a function of neutron star mass. All proton superconductivity gap models are displayed with dashed lines and neutron superfluidity ones, with solid lines. The dashed yellow line marks the dUrca threshold and the dashed blue line, the maximum masses for all EOS.

will not affect their dUrca luminosity and its effects will only be seen in the reduction of their heat capacity. A particularly interesting neutron gap model is NT SYHHP, whose late opening predicts that light neutron stars, with $M \leq 1.25 - 1.55\,\mathrm{M}_\odot$ for, respectively, $L \leq 70 - 112$ EOS, will not present neutron pairing. Its closing, around $M \geq 2\,\mathrm{M}_\odot$, indicates that heavy neutron stars might have unpaired neutrons in their innermost core. This nuclear pairing gap model is the best example of how a small variation in neutron star mass might significantly change its neutrino luminosity and heat capacity, if it crosses the nuclear pairing opening or closing curves.

In Figures 24 and 25, one can see a numerical example of the effect of nuclear pairing in dUrca neutrino luminosity, for NT EEHO and $T_e^\infty = 55$ eV. In general, for a given neutron star, its neutrino luminosity might be reduced by several orders of magnitude, depending on the percentage of core volume under superfluidity, as exemplified in Figure 25 for $L48$, $L69$ and $L105$ EOS. In Figure 24, this phenomenon is shown by comparing the luminosities calculated below and above the gap model closing curve (black solid line). The reduction in the dUrca neutrino luminosity thanks to nuclear pairing is also evident by observing the new predicted masses of the neutron stars with the inferred luminosities for MXB 1659-29. For almost all EOS, they are now around $M = 1.8\ \mathrm{M}_\odot$ and lie much

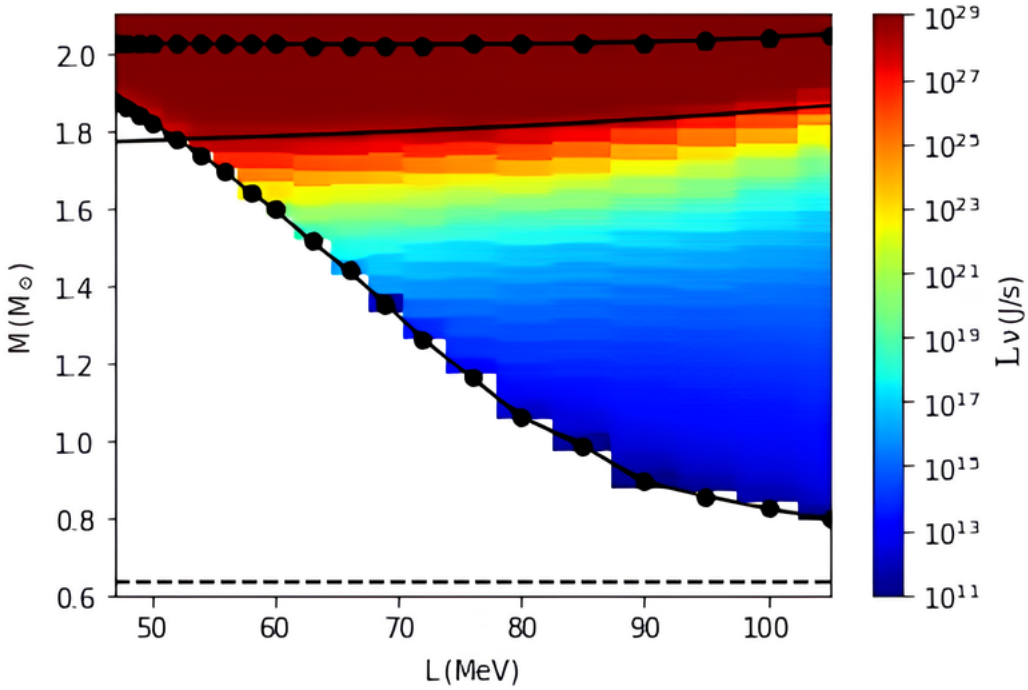

Figure 24: Color map of total neutrino luminosity as a function of total mass for all the EOS investigated under NT EEHO neutron superfluidity. The black dotted line on the top represents the maximum masses and the one on the bottom, the dUrca threshold. The black solid line is the NT EEHO gap model closing curve and the dashed one, its opening curve.

closer to the neutron superfluidity closing mass curve than the dUrca threshold curve when nuclear pairing is involved, that is, for $L \geq 55$ EOS.

The complete mass predictions for neutron stars with MXB 1659-29 neutrino luminosity, for all nuclear pairings, are shown in Figure 26, for proton superconductivity gap models, and in Figure 27, for neutron superfluidity gap models. Comparing the slopes of these curves with the closing curves of nuclear pairings, shown in Figure 23, one can see how most of the masses are either bordering the dUrca threshold curve, for early closing gap models, or bordering the closing curve of the nuclear pairing gap models. In other words, the luminosity searched is found as soon as the dUrca process is active or non-reduced by the formation of Cooper pairs, which again illustrates the effectiveness of direct Urca fast-cooling reactions. An interesting example is the NT SYHHP superfluidity gap model. Because of its late opening, one observes a bi-modal behavior on its mass predictions: for $L \leq 70$ EOS, neutron stars with MXB 1659-29's inferred luminosity are close to the maximum mass stars predicted by these EOS, as well as the closing curve of the gap model. On the other hand, for $L > 70$ EOS, the predicted mass curve follows

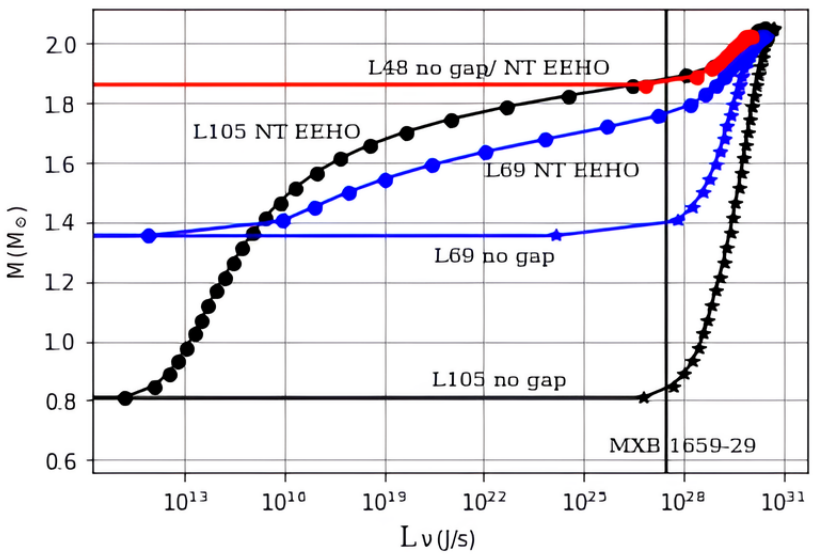

Figure 25: Total neutrino luminosity curves without nuclear pairing (stars) and with NT EEHO neutron superfluidity (circles). The black points represent $L105$ EOS, the blue points, $L69$ EOS and the red ones, $L48$ EOS. In the last case, the superfluid curve is indistinguishable from the no pairing curve in this scale. The vertical line is the approximate value of MXB 1659-29's neutrino luminosity, for reference.

the dUrca threshold curve, because the searched neutrino luminosity is obtained before this superfluidity model becomes active, as shown in Figure 28.

In the scenario investigated in this section, where the neutron star presents either proton superconductivity or neutron superfluidity, almost all EOS are able to reproduce MXB 1659-29's luminosity with any gap model considered. The only exception is NT AO with $L112$ EOS, which reaches the maximum mass before realizing a neutron star with the inferred luminosity. On the other hand, $L \geq 80$ EOS with relatively early closing gap models obtain neutron stars with the inferred luminosity, but they tend to predict masses $M \leq \mathrm{M}_{\odot}$, which are unrealistic. Those gap models are PS BCLL, PS AO, PS CCYps and PS EEHOr for proton superconductivity and NT EEHOR and NT SYHHP for neutron superfluidity. Furthermore, even though most of the EOS and nuclear pairing models are able to reproduce the inferred neutrino luminosities, the range of calculated masses for the $1\sigma\, \mathrm{L}_{\nu}$ values can be too narrow. For example, for all the calculated mass curves on Figure 26, a factor of 2 variation to the most likely neutrino luminosity issues a mass variation of $\Delta M \approx 0.02\,\mathrm{M}_{\odot}$. As in the no-pairing case, I argue that such a small mass range might be unrealistic, which motivates a re-calculation of these neutron star masses under the more realistic scenario of simultaneous proton and neutron nuclear pairing,

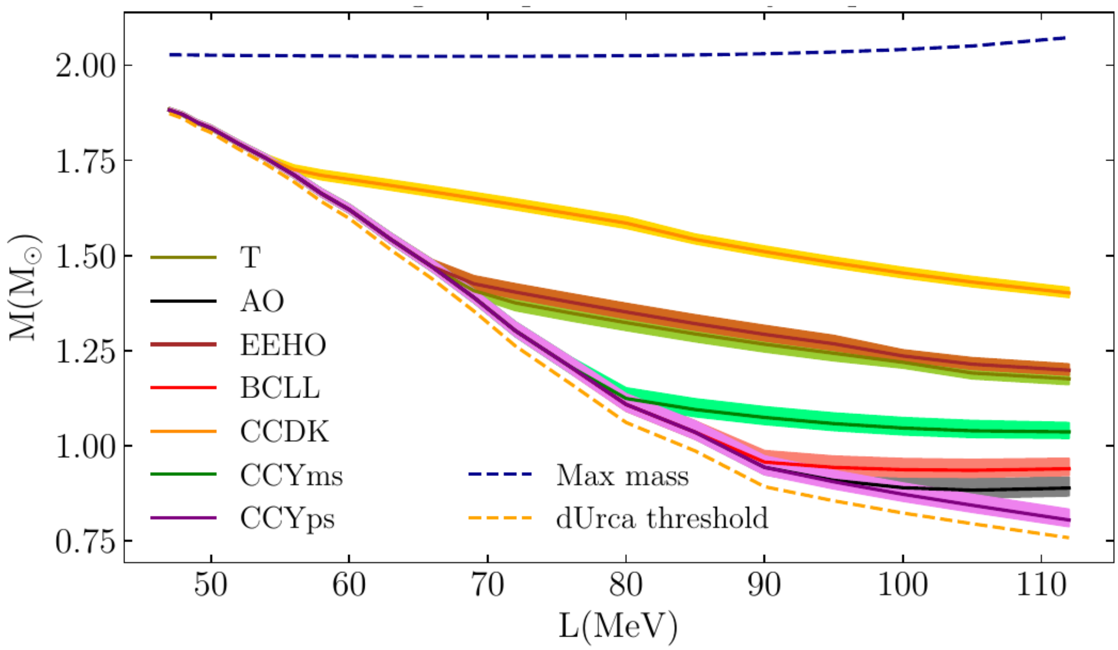

Figure 26: Total masses of the neutron stars with MXB 1659-29's inferred neutrino luminosity for all EOS. The solid lines represent its most likely value and the colored region around them, its 1σ lower and upper limits, for some proton superconductivity gap models. The dashed orange line represents the dUrca threshold and the dashed blue line, the maximum masses. The calculated mass curve for PS BS is not shown but it is indistinguishable from the PS CCYps one.

to be explored in section 4.3. Mass curves that are too close to the maximum mass curve, such as the ones resulting from NT AO, NT TTOA and NT SYHHP for $L \leq 65$ EOS, are also non-ideal, because they suggest that colder neutron stars might not be reproducible with those gap models.

I also calculate the total heat capacities of neutron stars, that are crucial in neutron star cooling calculations and also potentially relevant to discriminate their equation of state, as explained in Chapter 2. Once again the opening and closing densities of each gap model are more important than their amplitudes Δ in this calculation. Even though Δ is an explicit factor in the reduction rate R of the neutron star's heat capacity, the temperatures of the neutron stars under study are so low that comparing them with the gap model critical temperatures is only relevant close to its opening and closing densities. At all other densities, $R \approx 0$ fast enough that the number of protons on the neutron star volume affects the total heat capacity more than variations in R. This phenomenon is clearly observed in Figures 29 and 30, where the color gradient becomes warmer, repre-

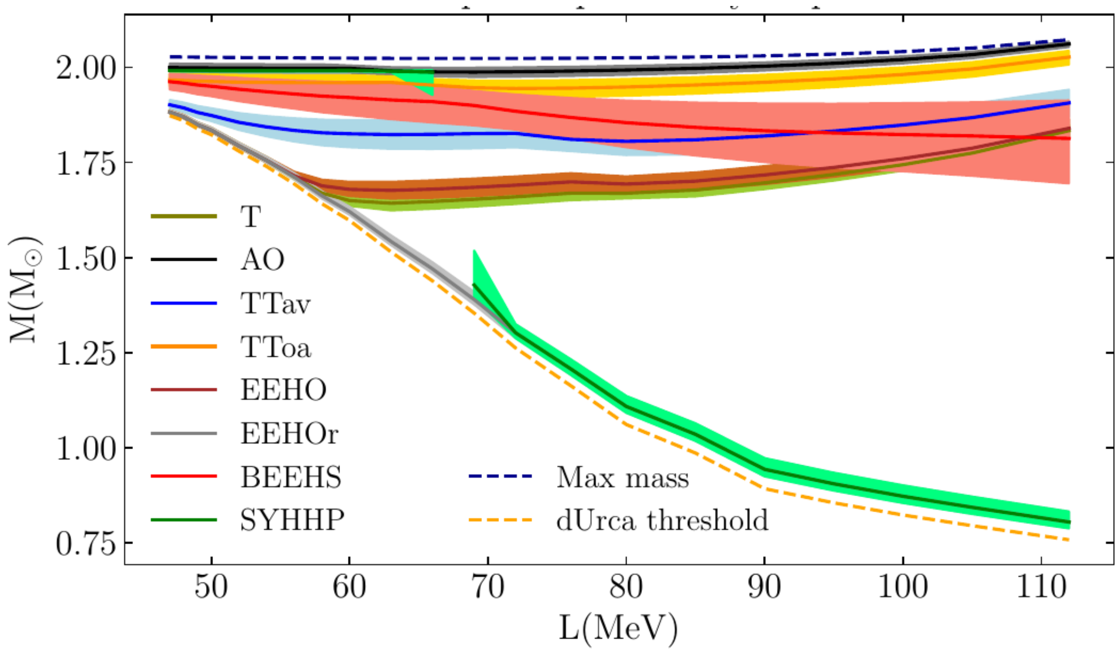

Figure 27: Total masses of the neutron stars with MXB 1659-29's inferred neutrino luminosity for all EOS. The solid lines represent its most likely value and the colored region around them, its 1σ lower and upper limits, for some neutron superfluidity gap models. The dashed orange line represents the dUrca threshold and the dashed blue line, the maximum masses.

senting larger heat capacities, towards the upper right of each plot, which corresponds to the neutron stars with larger proton fractions.

The total heat capacities of the neutron stars with the inferred neutrino luminosities for MXB 1659-29 are shown in Figure 31 for proton superconductivity gap models and Figure 32 for neutron superfluidity ones. Note that in the Figures some heat capacities of nuclear paired neutron stars are larger than not-paired ones, that is, part of the solid colorful curves are above the dashed "no pairing" curve, in apparent contradiction with expression $c'_x = R_x c_x$, for $R_x < 1$, that claims that nuclear pairing reduces the neutron star heat capacity. In fact, this claim is only valid for neutron stars with same mass and the heat capacities displayed in Figure 31 and 32 correspond to neutron stars with same neutrino luminosity, for a given L, but not necessarily same mass. The slope of each curve follows the slope of the closing curves of the gap models shown in figure 23, and in the special case of NT SYHHP, also the slope of its opening curve for intermediate and large L EOS, following the trend observed in Figures 26 and 27.

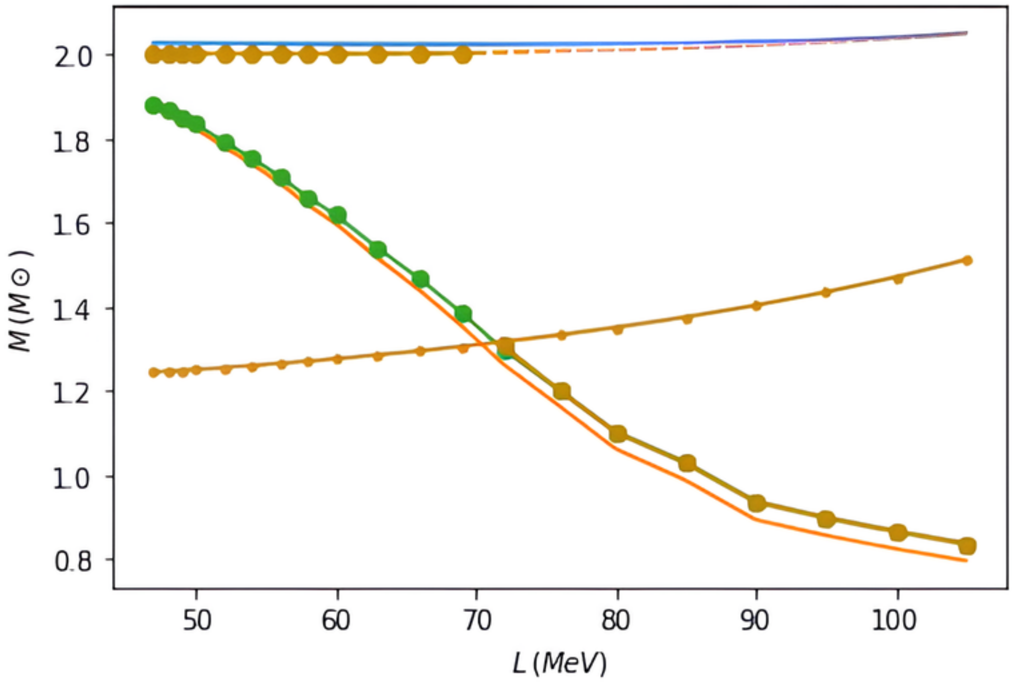

Figure 28: Total masses of the neutron stars with MXB 1659-29's inferred neutrino luminosity for all EOS, without nuclear pairing (green dotted curve) and with the NT SYHHP neutron superfluidity gap model (brown dotted curve). The dashed curve on the top represents this gap model closing curve and the dash-dotted line, with mass values from $1.2 - 1.4\,M_{\odot}$, its opening curve. The solid orange line is the dUrca threshold and the solid blue one, the maximum mass.

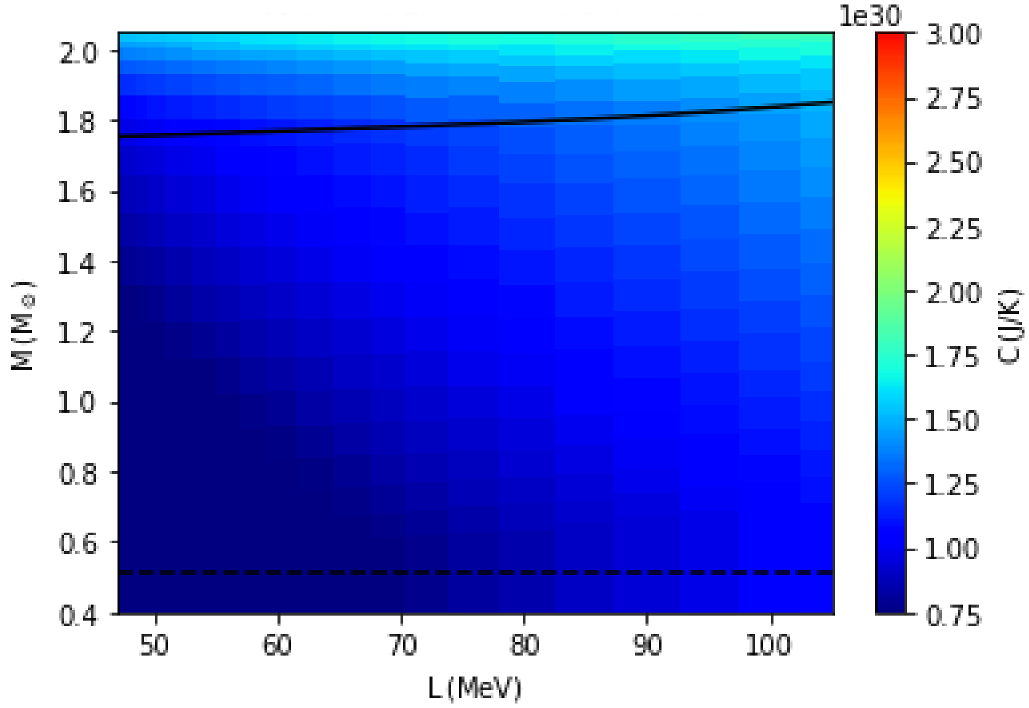

Figure 29: Color map of total heat capacity versus total mass for all the EOS, with NT T neutron superfluidity gap model and $T_e^{\infty} = 55$ eV. The solid line is the NT T gap model closing curve and the dashed one, its opening curve.

Comparing the results of total heat capacity and neutrino luminosity with the predictions from expression 2.39, I obtain Figure 33 for $L47$ EOS and Figure 34 for $L105$ EOS. I display only neutron superfluidity gap models because the heat capacity variations in $\mathrm{C} \times \mathrm{L}_\nu$ plots with proton superconductivity only gap models was too small to be visualized, but the results for that case are qualitatively similar. For both $L47$ and $L105$ EOS, one can observe that a measurement of $\Delta T/T \geq 2\%$ would not match MXB 1659-29's neutrino luminosity, because such a neutron star would require a very low total heat capacity, represented by the y-value where the $\Delta T/T$ curve and the vertical area of inferred L_ν intersect. For $\Delta T/T \geq 2\%$, this intersection would only happen at the horizontal region labelled "Leptons only" in the Figures, corresponding to the hypothetical case where all the heat capacity of the neutron star is provided by leptons, that is, all protons and neutrons are organized as Cooper pairs. Such a scenario is unrealistic, however, a temperature variation of $\Delta T/T \approx 1\%$ would be feasible for the strongest gap models considered here, which suggests that larger temperature variations smaller than 2% could be obtained with even stronger gap models. On the other hand, weak gap mod-

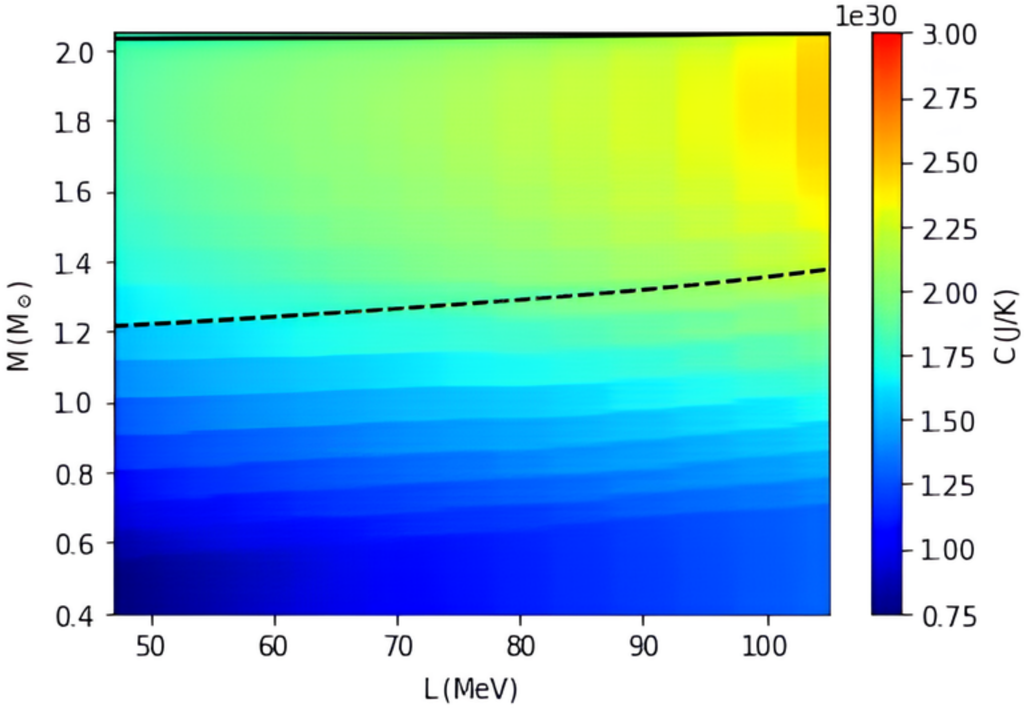

Figure 30: Color map of total heat capacity versus total mass for all the EOS, with NT SYHHP neutron superfluidity gap model and $T_e^\infty = 55$ eV. The solid line on the top is the NT SYHHP gap model closing curve and the dashed one, its opening curve.

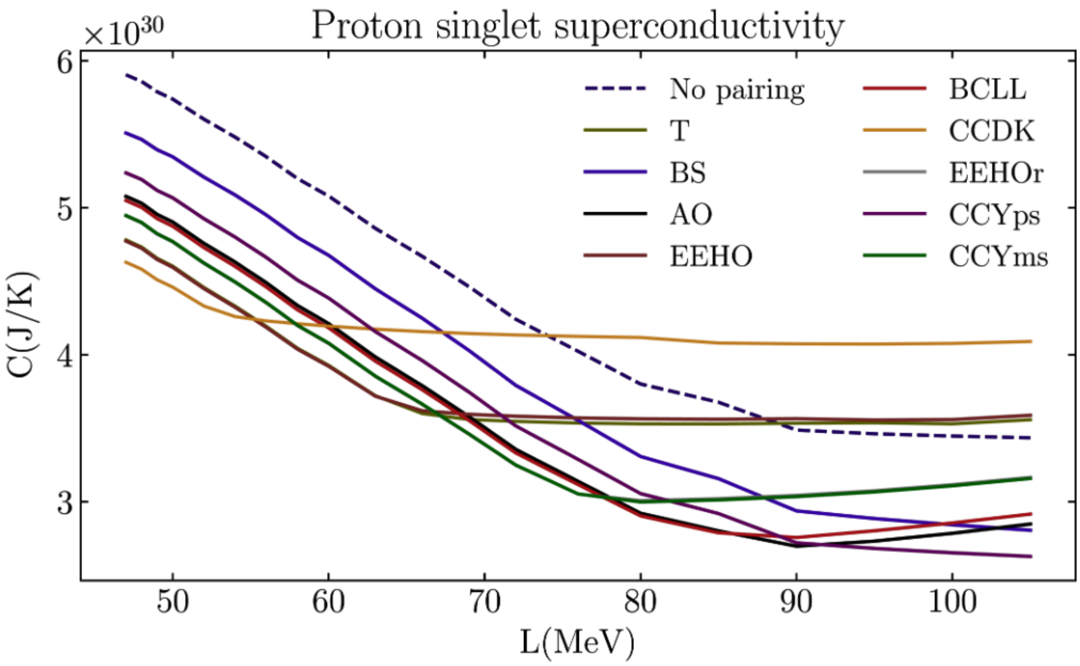

Figure 31: Total heat capacities of the neutron stars with the most likely inferred neutrino luminosity for MXB 1659-29 for all EOS under all proton singlet superconductivity gap models. For reference, the dashed blue line represents the total heat capacities of the neutron stars without nuclear pairing.

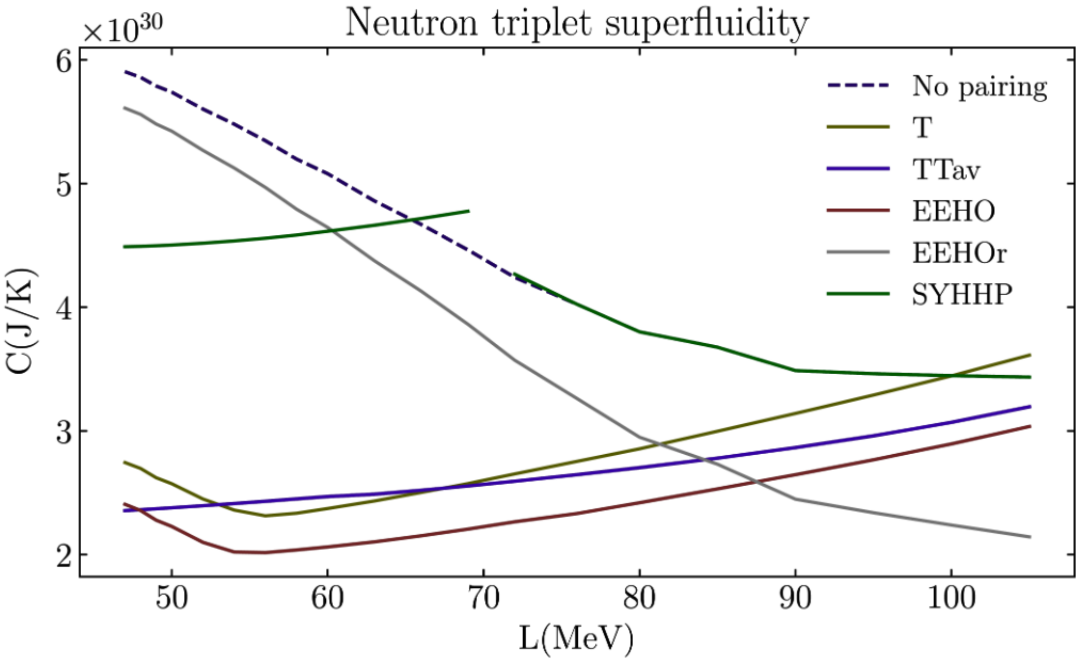

Figure 32: Total heat capacities of the neutron stars with the most likely inferred neutrino luminosity for MXB 1659-29 for all EOS under some neutron triplet superfluidity gap models. For reference, the dashed blue line represents the total heat capacities of the neutron stars without nuclear pairing.

els generate the lowest temperature variation, around 0.5% in both EOS. Hence, it is clear that, for a given EOS, temperature variation measurements in combination with inferred neutrino luminosities can determine whether a neutron star is under weak or strong gap models, therefore helping to investigate neutron star composition and nuclear pairing. The most important difference between the *L*47 and *L*105 plots is the extension of the "Leptons only" area, which is larger for the EOS that predicts a larger mass range of neutron stars with the inferred luminosity, in this case, the *L*105 EOS.

4.3 PROTON AND NEUTRON NUCLEAR PAIRING SIMULTANEOUSLY ACTIVE

In the more realistic case where both proton superconductivity and neutron superfluidity gap models are present and may even be simultaneously active in the neutron star core, I repeat the calculations from the previous section to investigate whether some combinations of proton and neutron nuclear pairing models fail to fit the in-

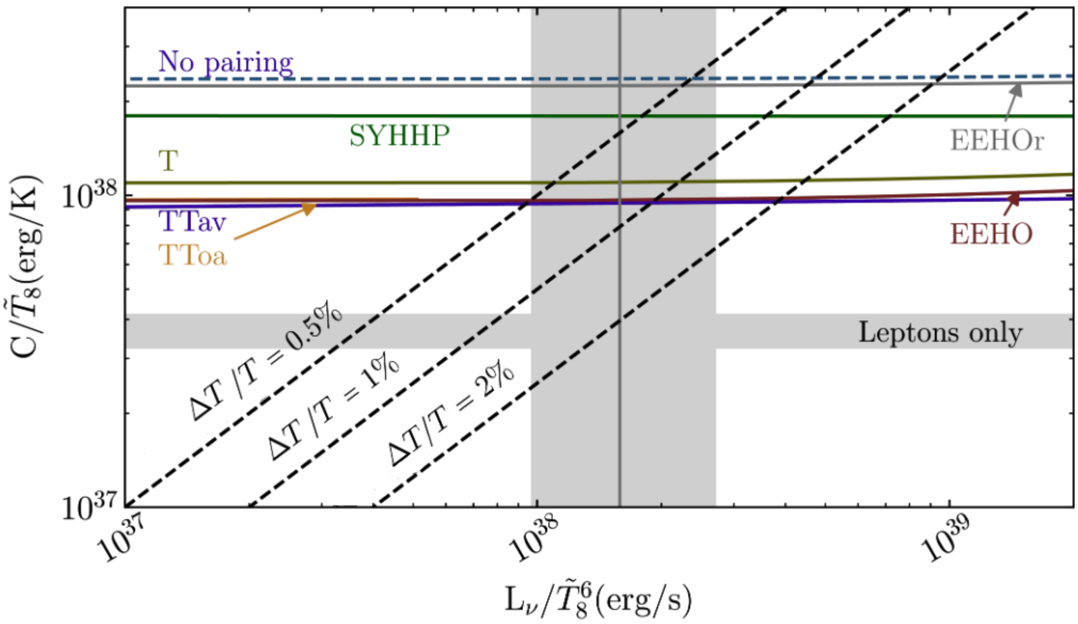

Figure 33: Total heat capacity divided by the normalization factor $\tilde{T}_8 = \tilde{T}/10^8$ K versus the normalized neutrino luminosity for all neutron stars with $L47$ EOS and $T_e^\infty = 55$ eV. $\Delta T/T = 0.5\%$, $\Delta T/T = 1\%$ and $\Delta T/T = 2\%$ curves, from equation 2.39, are also shown. For reference, the dashed blue line represents the case without nuclear pairing and the horizontal grey area labelled "Leptons only" represents the hypothetical case where all nuclei are paired throughout the whole neutron star volume. The vertical grey line represents the most likely neutrino luminosity for MXB 1659-29 and the grey area around it, its 1σ lower and upper limits. The colorful solid lines are the results for realistic neutron superfluidity gap models, labelled in the figure.

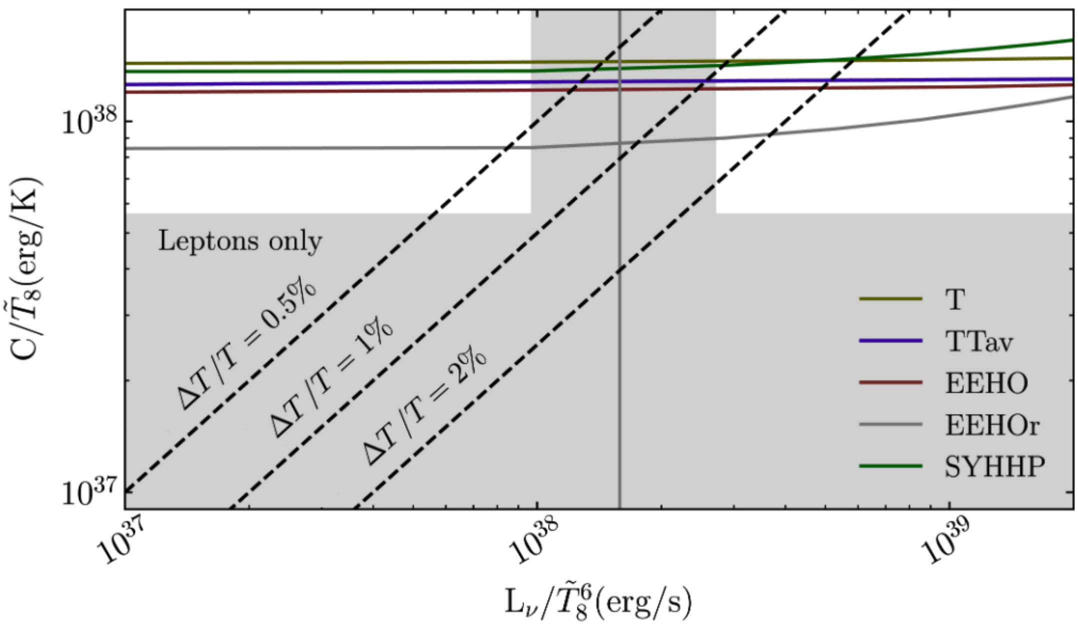

Figure 34: Same as Figure 33, but for $L105$ EOS.

ferred neutrino luminosities of MXB 1659-29 and SAX J1808.4-3658 for a given EOS. I use the approximation that the direct Urca luminosity rate will be reduced by a factor $R_{\text{proton, neutron}} \sim \min\left(R_{\text{proton}}, R_{\text{neutron}}\right)$ when both R_{proton} and $R_{\text{neutron}} < 1$, and I combine the 9 proton superconductivity with the 8 neutron superfluidity gap models under study, resulting in 72 nuclear pairing combinations, to obtain new results for neutron star masses with the inferred luminosities. These results can be classified in three categories:

- Individual gap predominance. It happens when the reduction rate of one gap model is negligible in comparison with the other. In this case, the new calculated mass curve of the neutron stars with the inferred luminosity is equal to the one of the dominating gap model. An example is shown in Figure 35, for PS AO+NT BEEHS, where the neutron gap model dominates. The great majority of the gap model combinations investigated fits in this category, usually with superfluidity models dominating but eventually with superconducting dominance, for strong proton pairing gap models and weak neutron pairing ones.

- Alternation between individual gap predictions. Common when the two reduction rates are comparable within a significant volume of the neutron star, the resulting mass curve alternates between the predictions of the neutron gap model and the proton one. An example is shown in Figure 36, for the PS CCDK+NT EEHO combination, with neutron superfluidity dominance for $L \geq 65$ EOS and proton dominance for $55 \leq L < 65$ EOS. This category usually includes strong proton gap models and weak neutron ones.

- Completely new predictions. Only very few of the neutron and proton gap model combinations result in a predicted mass curve that does not completely overlap with the previous mass predictions for individual gap models. Those are the cases of, for example, PS CCDK+NT BEEHS (Figure 37) as well as PS CCDK+NT SYHHP (Figure 38), for some EOS. This scenario is realized for strong neutron and proton pairing models and particularly with the late opening NT SYHHP gap model.

With the new calculations, it is now possible to obtain MXB 1659-29's inferred neutrino luminosity for all EOS and nuclear pairing combinations. However, regardless of

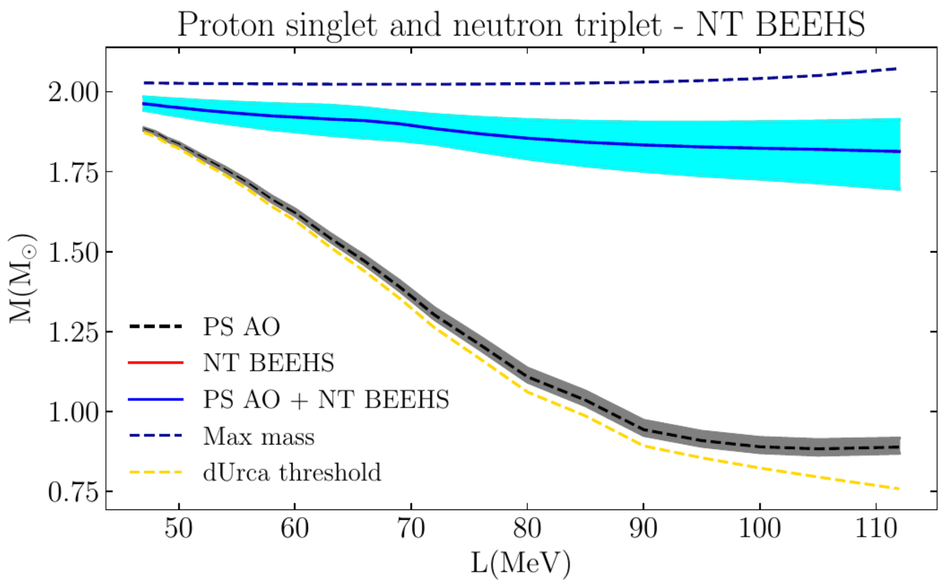

Figure 35: Total masses of the neutron stars with MXB 1659-29's inferred neutrino luminosity for all EOS, with PS AO proton pairing model (grey dashed curve), NT BEEHS neutron pairing model (red solid curve, completely below the blue curve) and their combination PS AO+NT BEEHS (blue solid curve). The dashed orange line is the dUrca threshold and the dashed blue one, the maximum mass.

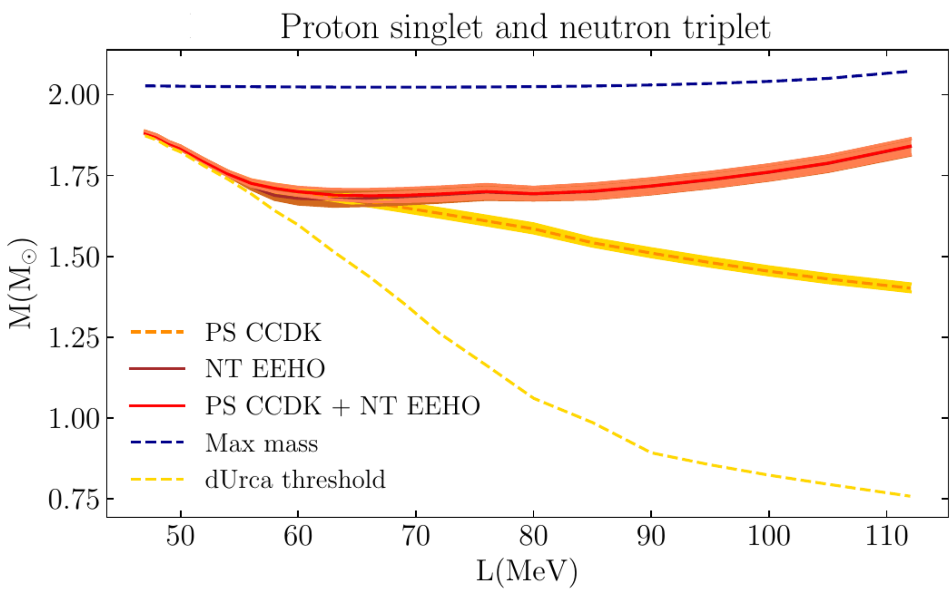

Figure 36: Total masses of the neutron stars with MXB 1659-29's inferred neutrino luminosity for all EOS, with PS CCDK proton pairing model (yellow dashed curve), NT EEHO neutron pairing model (brown solid curve) and their combination PS CCDK+NT EEHO (red solid curve). The dashed orange line is the dUrca threshold and the dashed blue one, the maximum mass.

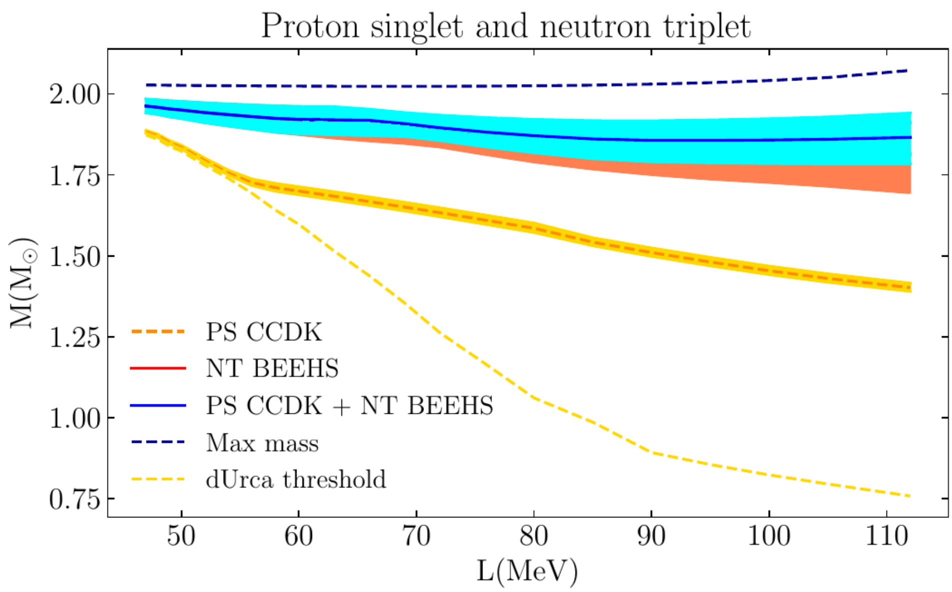

Figure 37: Total masses of the neutron stars with MXB 1659-29's inferred neutrino luminosity for all EOS, with PS CCDK proton pairing model (yellow dashed curve), NT BEEHS neutron pairing model (red solid curve) and their combination PS CCDK+NT BEEHS (blue solid curve). The dashed orange line is the dUrca threshold and the dashed blue one, the maximum mass.

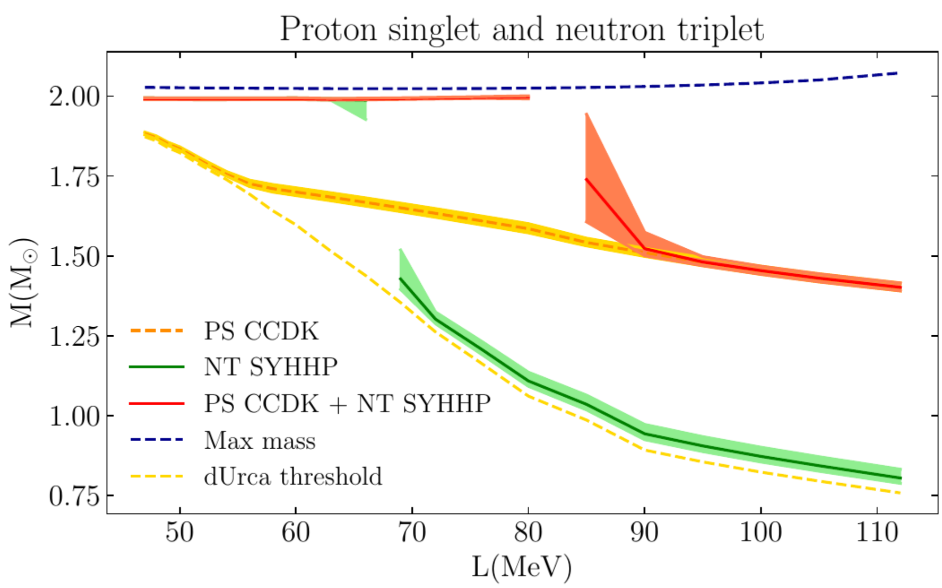

Figure 38: Total masses of the neutron stars with MXB 1659-29's inferred neutrino luminosity for all EOS, with PS CCDK proton pairing model (yellow dashed curve), NT SYHHP neutron pairing model (green solid curve) and their combination PS CCDK+NT SYHHP (red solid curve). The interruption in the PS CCDK and NT SYHHP curves correspond to EOS with which I did not work, for example, $80 < L < 84$ MeV EOS. The dashed orange line is the dUrca threshold and the dashed blue one, the maximum mass.

the category in which the new mass curve fits, in the overwhelming majority of the cases, its mass range $\Delta M \approx 0.02\,\mathrm{M}_\odot$ for the 1σ neutrino luminosity variation around the most likely value remains the same. As in the previous section, there are also a few of the gap model combinations that predict larger mass ranges, for example, PS AO+NT BEEHS with $\Delta M \approx 0.2\,\mathrm{M}_\odot$ for large L EOS. In all those cases, I conclude that the calculated mass predictions from the previous section were very good approximations with similar results to the mass curves of the combined nuclear pairings, especially the neutron superfluidity only predictions (Figure 27), that usually dominate over the proton gap model ones when combined. A very few interesting exceptions exist, such as the red curve in Figure 38, that represents the gap model combination PS CCDK+NT SYHHP, with an increase in mass range for $L85$ and, in a smaller scale, for $L90$ EOS, not seen in the PS CCDK or NT SYHHP only calculations. These cases have been thoroughly investigated to check which factors are determinant in increasing the predicted neutron star mass ranges, that is, for each neutron star in this situation, I have checked the evolution of dUrca neutrino emissivity as a function of density as well as the effective neutron and proton masses, electron fraction and $m(r)/r$ factor as a function of density. The goal of these investigations has been to determine whether the mass range increase is mainly a feature of the EOS microphysics or neutron star structure effects, such as the amount of core volume under nuclear superfluidity. I summarize the main results below.

Figure 39 displays the accumulated dUrca luminosity at several neutron star radii $r < R$ for PS CCDK+NT SYHHP, with $L80$, $L85$ and $L90$ EOS. The neutron stars shown in that plot have MXB 1659-29's inferred luminosity at $r = R$. One observes that a smoother increase in the neutrino luminosity as a function of radius is correlated with the EOS presenting a larger mass range in Figure 38. This reduction in neutrino luminosity specifically for those EOS is caused by the interaction of the two gap model's reduction rates, shown in Figure 40 for $L85$ EOS. In that Figure, I note that, for the whole neutron star core, the dUrca neutrino emissivity is always reduced, $R_{\text{proton, neutron}} < 1$, even more strongly at its outermost part, which compresses the largest part of its volume. Another way of visualizing the interplay between the proton and neutron nuclear pairing luminosity reductions is by comparing the accumulated dUrca luminosity in Figures 41 and 42, for several nuclear pairing scenarios where the total neutrino luminosity

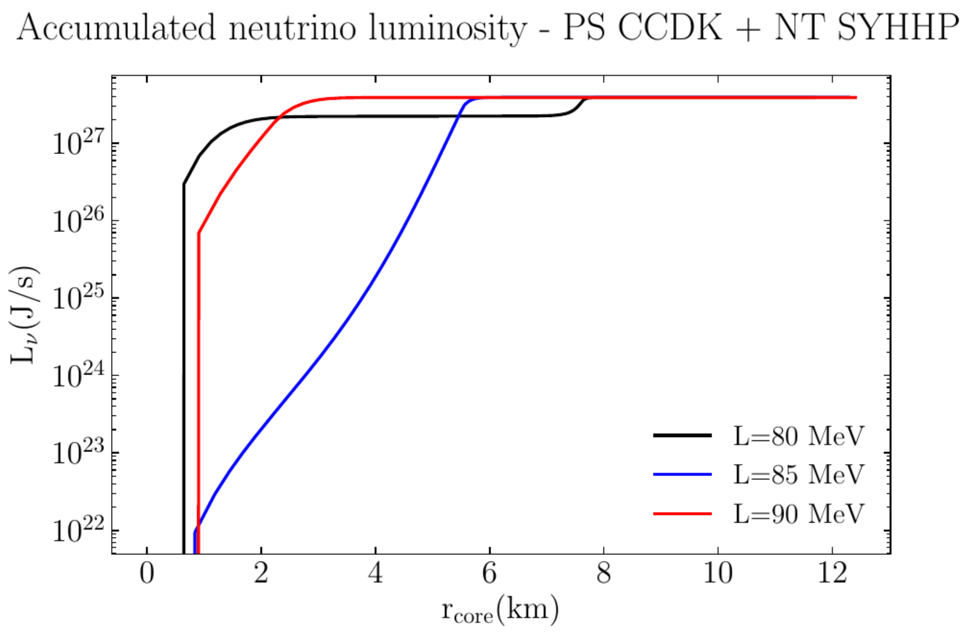

Figure 39: Accumulated dUrca neutrino luminosity as a function of radii for the PS CCDK+NT SYHHP combination in neutron stars with total neutrino luminosity equal to MXB 1659-29's most likely value, for $L80$, $L85$ and $L90$ EOS.

equals MXB 1659-29's most likely inferred luminosity. In those Figures it becomes even more evident that the most important factor differentiating $L85$ and $L90$ with the PS CCDK+NT SYHHP combination is the percentage of core volume under NT SYHHP influence. In other words, Figures 38 - 42 have shown in many ways that an increased range in the predicted masses for the neutron stars with the searched luminosities can be accomplished with nuclear pairing suppression of dUrca emissivity, but only for specific EOS and gap model combinations.

This conclusion can be extended to SAX J1808.4-3658 simulations, with some examples shown in Figure 43, for light element envelope composition, and Figure 44, that displays two nuclear pairing combinations in a heavy elements envelope. Once again I was able to obtain this source's inferred neutrino luminosity limits with all EOS, but, for this neutron star, not with all nuclear pairing combinations. The ones able to fit the inferred luminosity data of $L_\nu = (1 \times 10^{25} - 1 \times 10^{26})$ J/s predict a small mass range for the neutron stars. A light element envelope composition leads to higher surface temperature, implying lower neutrino luminosities for the neutron star, as seen in Figure 45. Therefore, strong pairing gap models with a light element envelope cannot always reproduce SAX J1808.4-3658's neutrino luminosity. On the other hand, a heavy element envelope needs

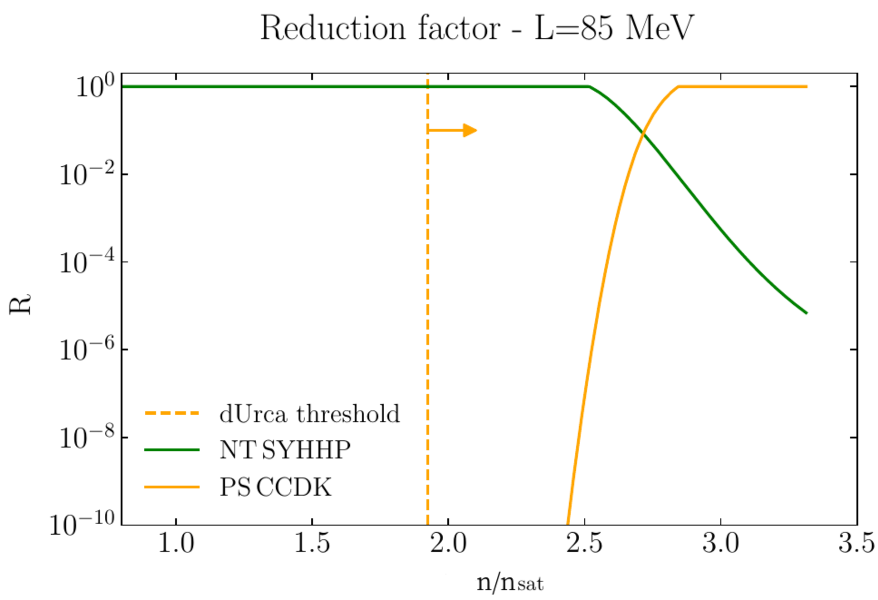

Figure 40: Reduction rates of dUrca neutrino emissivity for proton superconductivity gap model PS CCDK (yellow curve) and neutron superfluidity gap model NT SYHHP (green curve) for the neutron star with MXB 1659-29's most likely inferred neutrino luminosity with *L*85 EOS. The vertical dotted line is the dUrca threshold and the arrow indicates the densities for which dUrca processes are allowed.

strong nuclear pairings to fit the source's inferred luminosities and show a significant increase in mass range predictions when compared to the not-paired case, as seen in Figure 44. Using weak nuclear pairing model combinations with a light element envelope or strong nuclear pairing models with a heavy element envelope, this source's neutrino luminosities can be reproduced for all temperatures $T_e^\infty = 36^{+4}_{-8}$ eV.

All the results described in this section confirm the importance of including both nuclear pairing models in neutron star luminosity calculations and simultaneously accounting for their reduction rates in dUrca emissivity, because one cannot always predict which reduction rate will dominate for all EOS and all neutron star volumes. On the other hand, the fact that neutron superfluidity gap models tend to dominate in the dUrca emissivity calculations suggest that other quantities must be studied alongside neutrino luminosity, such as heat capacity, to fully determine the influence of nuclear pairing in neutron stars. As an example of the importance of this consideration, I repeat the calculation of equation 2.39 to include nuclear pairing combinations. I obtain Figures 46 and 47, for *L*47 and *L*112.7 EOS respectively, showing that now $\Delta T/T = 2\%$ can be consistent with observations for weak nuclear pairing combinations and large L or

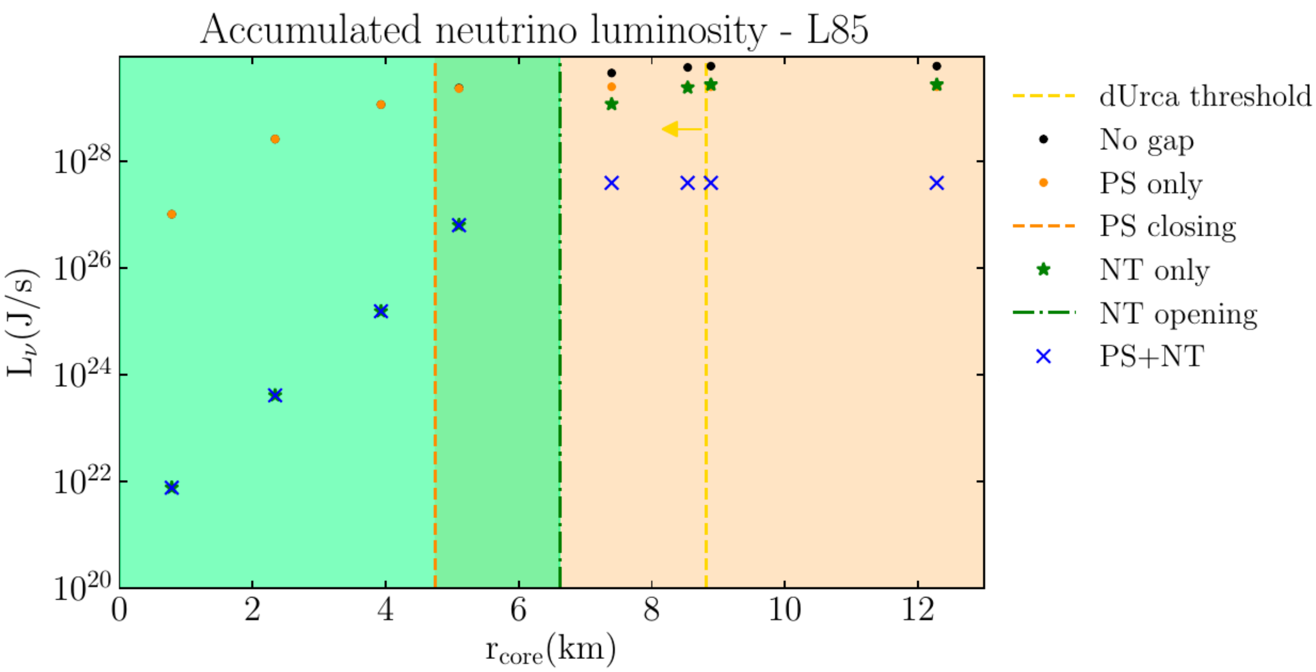

Figure 41: Accumulated dUrca neutrino luminosity at selected radii for the neutron stars with total neutrino luminosity equal to MXB 1659-29's most likely value, with *L*85 EOS. Black circles indicate the no-pairing case and orange circles, the PS CCDK-only case. The pink shaded area corresponds to the region where the PS gap model is active and the dotted orange line, its closing radius. The NT SYHHP-only case is shown by the green stars and the green shaded area corresponds to the region where it is active, while the vertical green dot-dashed line marks its opening radius. The blue "×"s display the results of the PS CCDK+NT SYHHP combination. The vertical yellow dashed line is the dUrca threshold and the arrow indicates the radii for which dUrca processes are allowed.

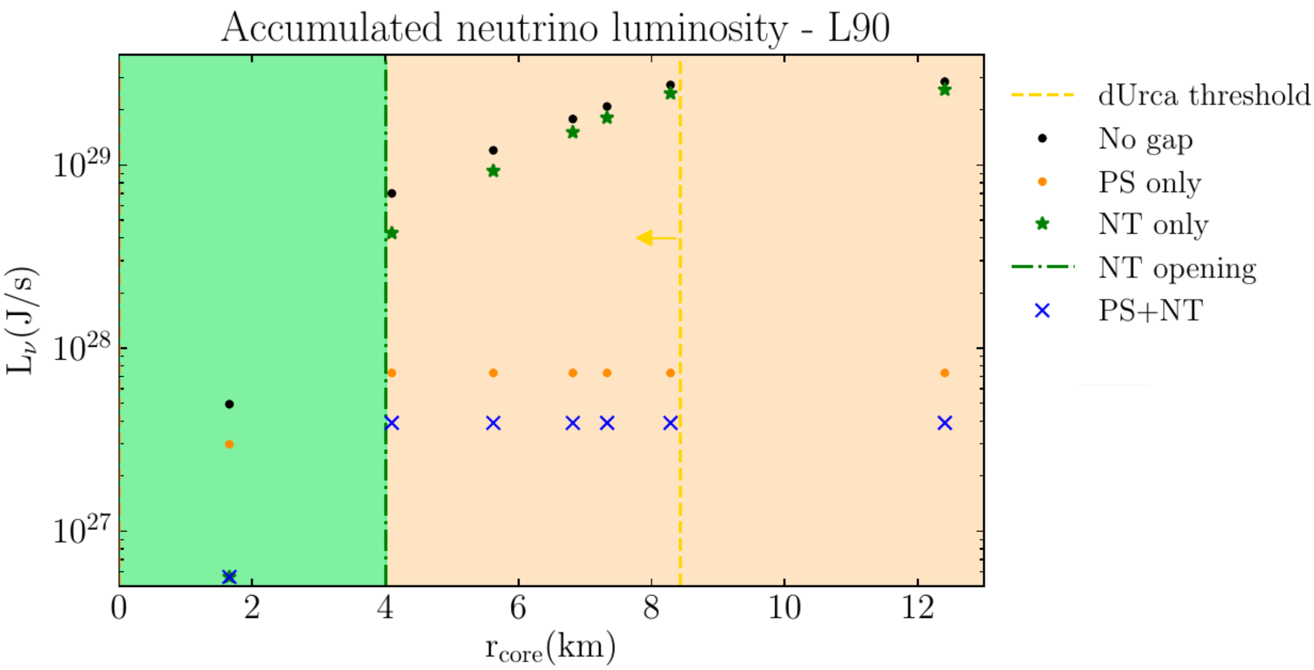

Figure 42: Same as Figure 41, but for *L*90 EOS.

strong nuclear pairing combinations and small L. Accounting for the cumulative reduction in heat capacity provided by nuclear pairing, one can obtain lower heat capacities with similar neutrino luminosities, once again attesting to the importance of probing several observable or inferred quantities simultaneously when studying neutron stars.

For both neutron stars studied here, all L EOS were able to reproduce the inferred neutrino luminosities, given a suitable nuclear pairing combination. Nonetheless, I observed that dUrca reactions are extremely effective and tend to cool the neutron star too fast, even including the emissivity reduction provided by nuclear pairing. Thus, in the next section, I proceed to investigate whether less effective dUrca processes could provide a more natural description of the neutrino luminosities of cold neutron stars.

4.4 SIMULATING LESS EFFICIENT REACTIONS

4.4.1 $Q < 1$

As a preliminary step towards the calculation of less effective dUrca reactions, I initially do not explicitly include in the cooling calculations additional dUrca cooling rates, for

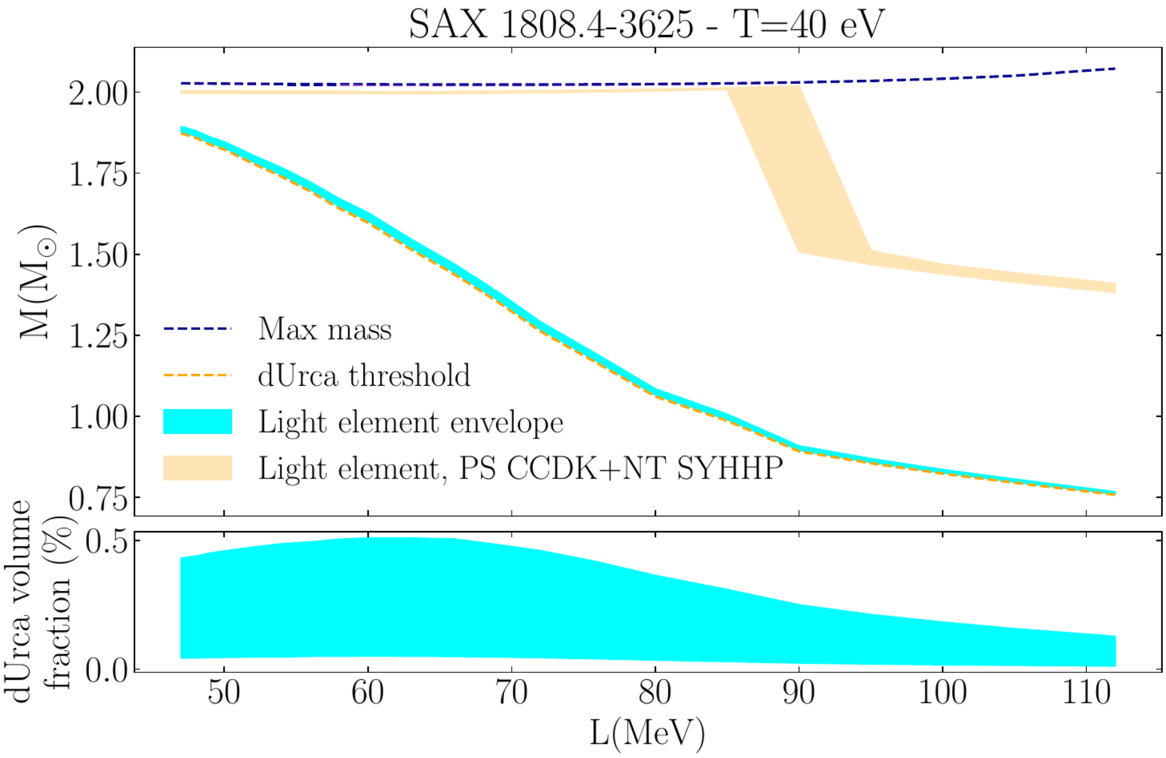

Figure 43: (Upper plot) Total masses of the neutron stars with the inferred neutrino luminosities of SAX J1808.4-3658 for all EOS under study, assuming $T_e^\infty = 40$ eV. The blue area encompasses the lower and upper limits of its most likely inferred neutrino luminosity without nuclear pairing and assuming a light element envelope, whereas the pink area represents the predicted masses of neutron stars with the same envelope composition and neutrino luminosities but with PS CCDK+NT AO nuclear pairing. The dUrca threshold is the dashed orange line on the bottom and the dashed blue line on the top is the maximum mass. (Bottom plot) Percentage of core volume under direct Urca reactions for the non-paired neutron stars with light element envelope composition.

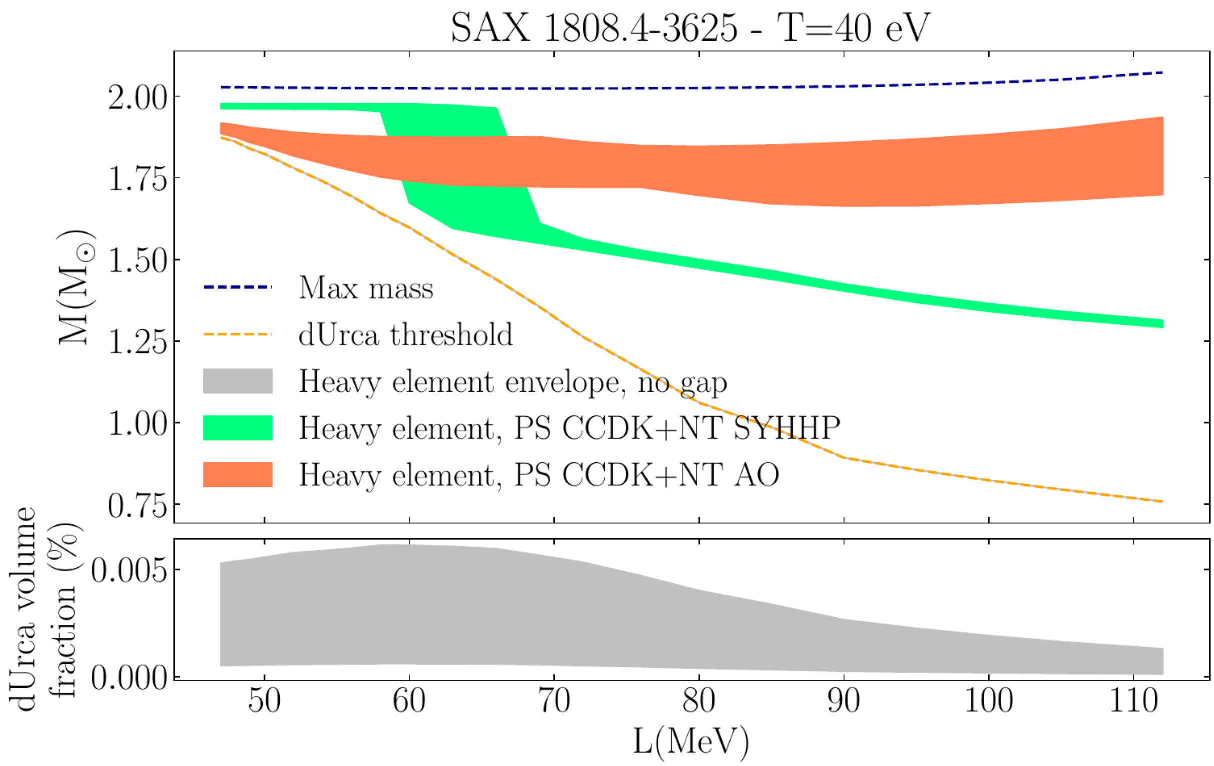

Figure 44: (Upper plot) Total masses of the neutron stars with the inferred neutrino luminosities of SAX J1808.4-3658 for all EOS under study, assuming $T_e^\infty = 40$ eV and a heavy element envelope composition. The dUrca threshold is the dashed orange line on the bottom and the dashed blue line on the top is the maximum mass. The grey area, bordering the dUrca threshold, encompasses the lower and upper limits of its most likely inferred neutrino luminosity without nuclear pairing whereas the red and green areas represent the predicted masses of neutron stars with the same neutrino luminosities but with PS CCDK+NT AO and PS CCDK+NT SYHHP nuclear pairing respectively. (Bottom plot) Percentage of core volume under direct Urca reactions for the non-paired neutron stars.

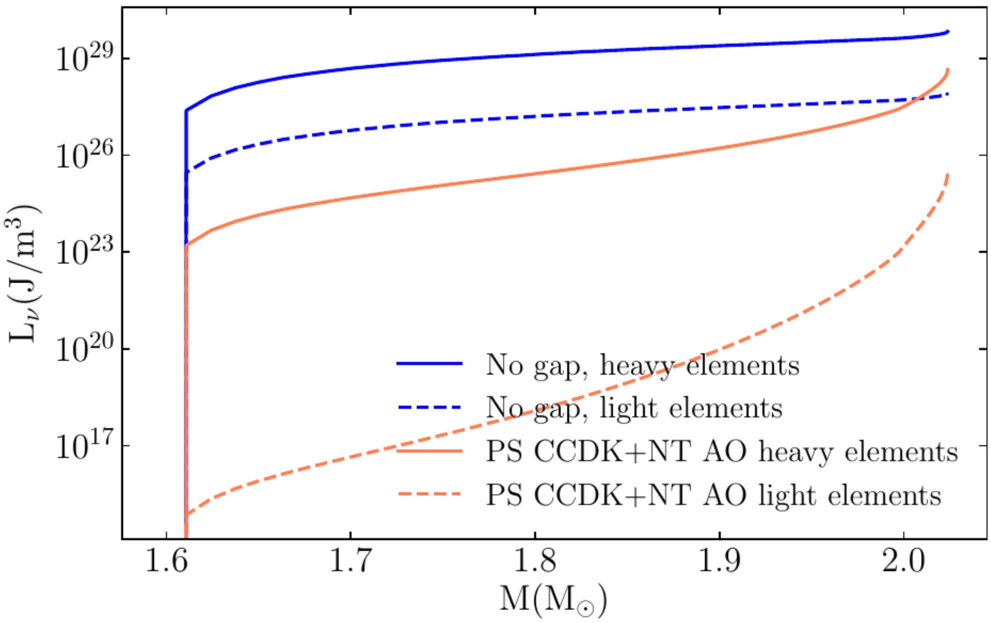

Figure 45: Total neutrino luminosity curves for neutron stars with $L60$ and $T_e^\infty = 40$ eV, with heavy element envelope without nuclear pairing (solid blue curve), with PS CCDK+NT AO pairing combination (solid red curve), with light element envelope without nuclear pairing (dashed blue curve) and with PS CCDK+NT AO pairing combination (dashed red curve).

example, of delta-resonances, hyperons or free quarks. Instead, I simply simulate the effect a smaller dUrca emissivity would have in the calculated mass curves by assuming the new $\epsilon'_{\mathrm{Urca}} = Q\,\epsilon_{\mathrm{Urca}}$, where $Q < 1$ and ϵ_{Urca} corresponds to the dUrca emissivity with or without nuclear pairing. This is an oversimplification, firstly because assuming the existence of smaller dUrca emissivities as a result of other particles cooling reactions demands that these particles are also properly included in the neutron star EOS. Secondly, these new cooling channels also have their own dUrca thresholds, which most likely will not be the same I calculated for nucleonic dUrca with $npe\mu$ matter. Finally, the existence of additional dUrca cooling channels does not preclude nucleonic dUrca cooling, such that a proper calculation would include all existing dUrca processes. Despite these sources of error, this approximation has been useful to set limits on the minimum effectiveness a dUrca process by itself can have to reproduce the inferred neutrino luminosity of cold neutron stars. Because of the qualitative nature of this investigation, it suffices to study the patterns in the reproduction of one of the neutron stars, hence I only display the results for MXB 1659-29 in this section.

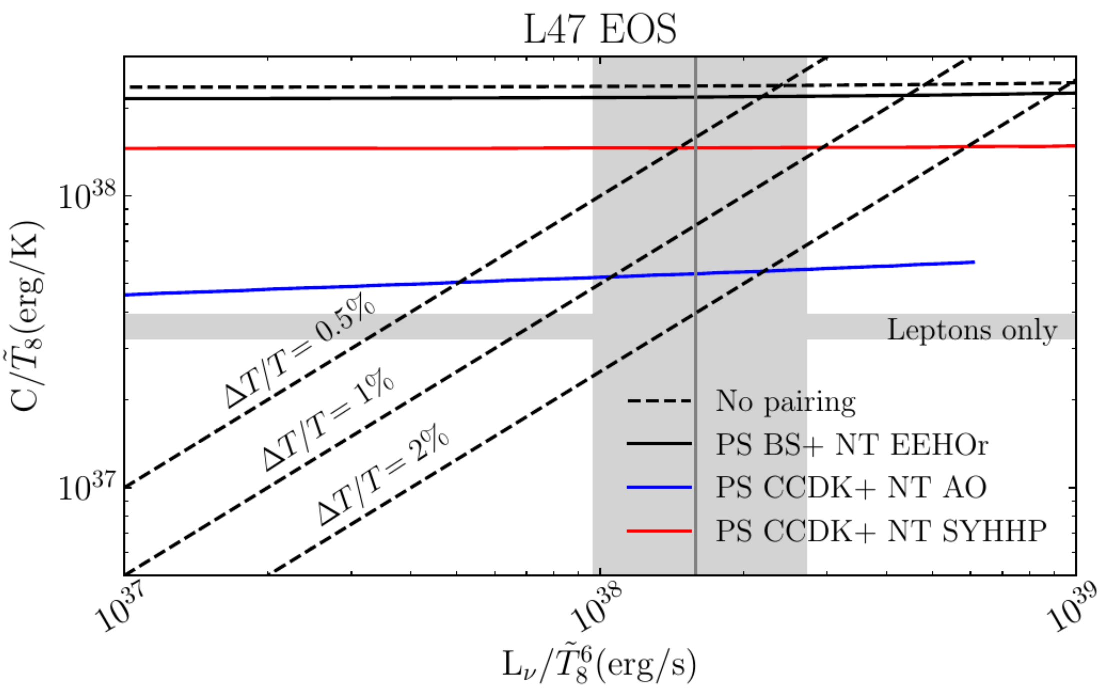

Figure 46: Total heat capacity divided by the normalization factor $\tilde{T}_8 = \tilde{T}/10^8$ K versus the normalized neutrino luminosity for all neutron stars with $L47$ EOS and $T_e^\infty = 55$ eV. $\Delta T/T = 0.5\%$, $\Delta T/T = 1\%$ and $\Delta T/T = 2\%$ curves, from equation 2.39, are also shown. For reference, the dashed black line on top represents the case without nuclear pairing and the horizontal grey area labelled "Leptons only" represents the hypothetical case where all nuclei are paired throughout the whole neutron star volume. The vertical grey line represents the most likely neutrino luminosity for MXB 1659-29 and the grey area around it, its 1σ lower and upper limits. The colorful solid lines are the results for combinations of proton and neutron pairing gap models, labelled in the Figure.

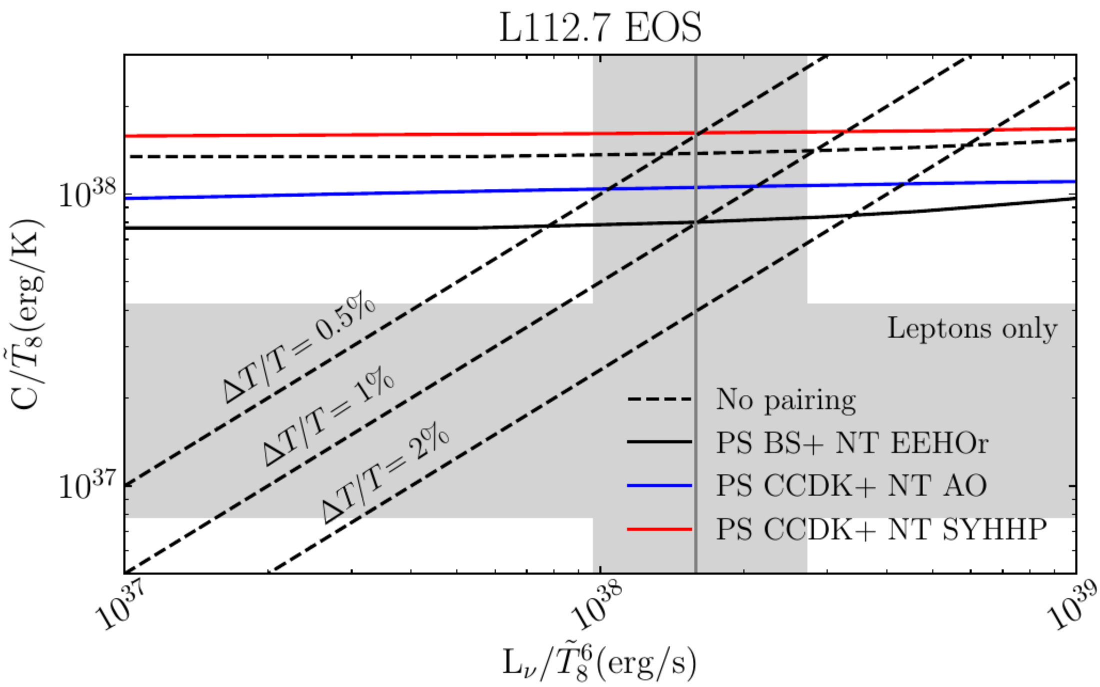

Figure 47: Same as Figure 46 but for $L112.7$ EOS

Starting with $Q = 0.1$, I obtain Figures 48, 49 and 50 for the no-pairing, proton superconductivity only and neutron superfluidity only scenarios. The increase in mass range for neutron stars with MXB 1659-29's neutrino luminosity, shown in those Figures, is evident when compared with the $Q = 1$ results on sections 4.2 and 4.3. Furthermore, the increase of the dUrca volume fraction, displayed in the bottom plot of Figure 48, from around 1% to up to 20%, suggests that a not-so-small Q could need a too large fraction of core volume involved in dUrca reactions to reproduce the neutrino luminosities searched, being unattainable for those EOS. That Figure also suggests that larger L EOS could accommodate less efficient dUrca reactions more easily than small L EOS, that is, smaller Q could fit MXB 1659-29's neutrino luminosity only with large L EOS.

Those patterns are also observed when proton superconductivity and neutron superfluidity are added. With nuclear pairing, not only the range of predicted neutron star masses increases, but also all mass curves are also shifted upwards, indicating larger neutron star masses are required overall. In this context, strong gap models have difficulty reproducing the neutrino luminosity data when $Q < 1$, especially for large L EOS.

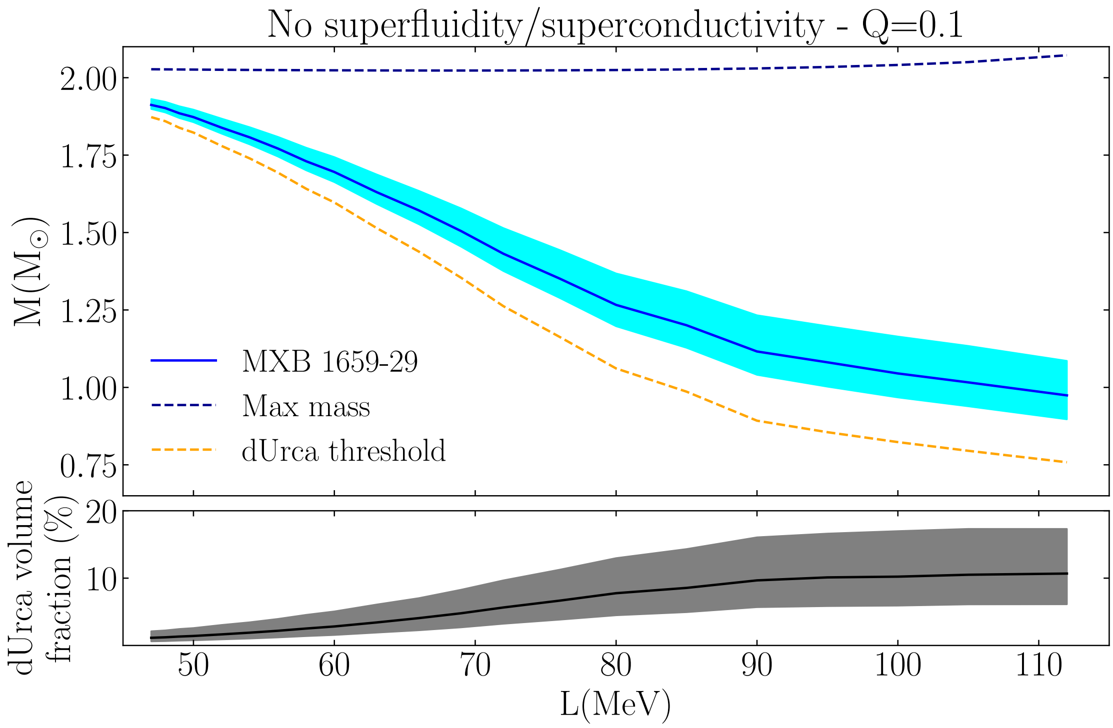

Figure 48: (Upper plot) Total masses of the neutron stars with the $1\,\sigma$ inferred neutrino luminosities of MXB 1659-29 for all EOS under study, with dUrca emissivity reduced by the factor $Q = 0.1$, without nuclear pairing. The dUrca threshold is the dashed orange line on the bottom and the dashed blue line on the top is the maximum mass. (Bottom plot) Percentage of core volume under direct Urca reaction for the neutron stars displayed above.

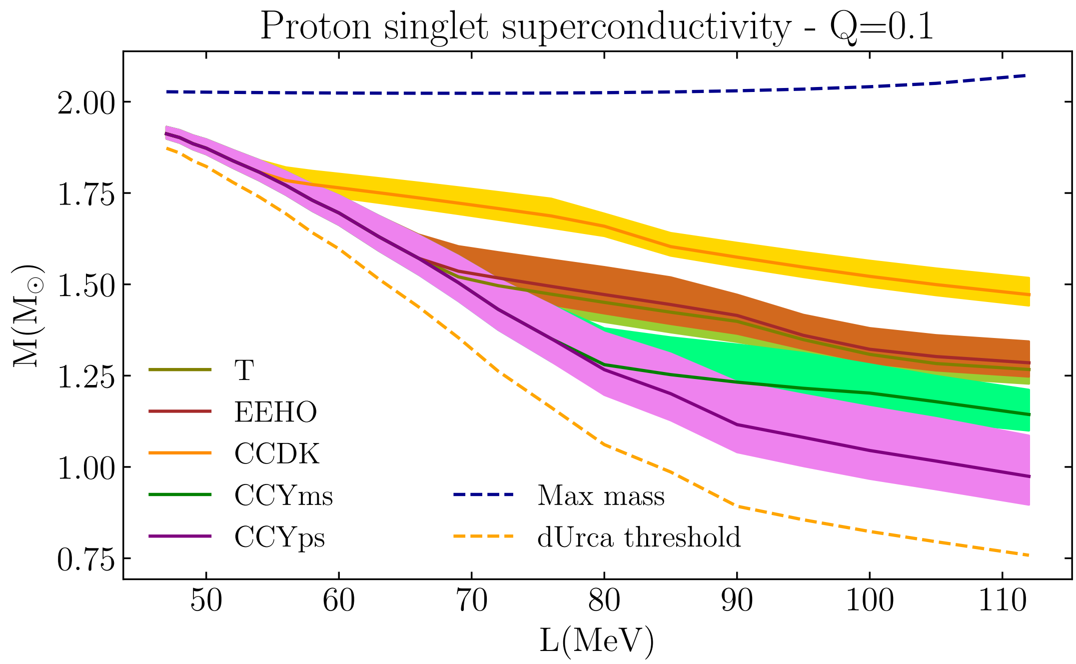

Figure 49: Total masses of the neutron stars with MXB 1659-29's $1\,\sigma$ inferred neutrino luminosity for all EOS. The solid lines and colored region around them represent the mass predictions for some proton superconductivity gap models, with dUrca emissivity reduced by a factor $Q = 0.1$. The dashed orange line is the dUrca threshold and the dashed blue line, the maximum masses. Mass predictions for the proton gap models not shown are under the displayed curves.

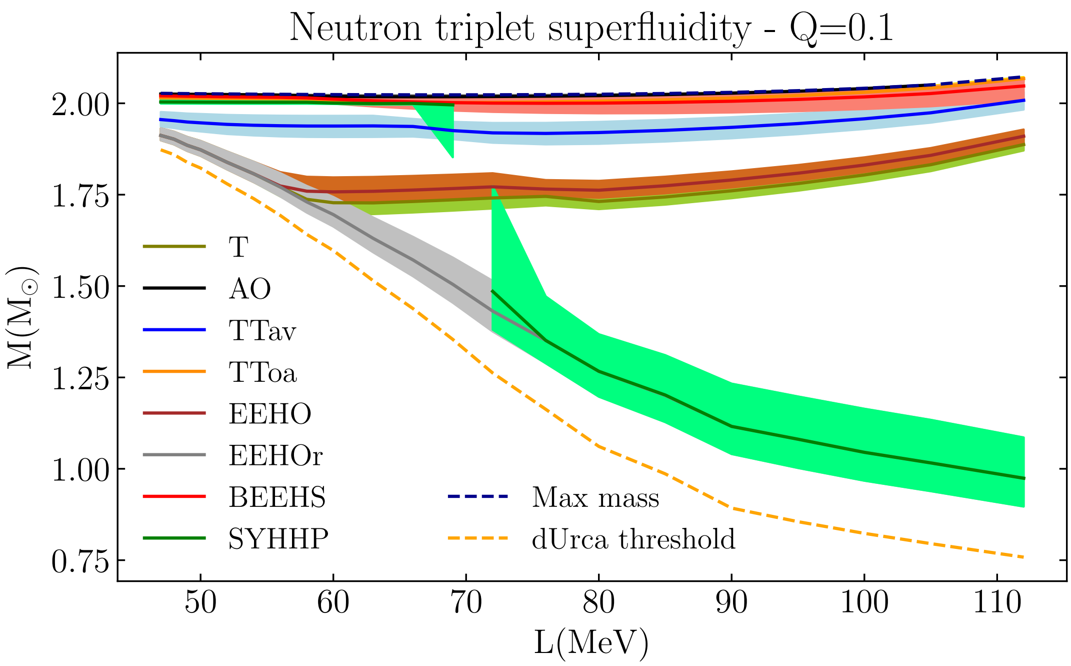

Figure 50: Total masses of the neutron stars with MXB 1659-29's 1 σ inferred neutrino luminosity for all EOS. The solid lines and colored region around them represent the mass predictions for all neutron superfluidity gap models, with dUrca emissivity reduced by a factor $Q = 0.1$. The dashed orange line is the dUrca threshold and the dashed blue line, the maximum masses.

The total range of allowed Q values is shown in Figure 51, considering no nuclear pairing, for $L47$ and $L112.7$ EOS. Under the conditions I performed this calculation, $L47$ EOS is unable to reproduce the upper and lower limits of MXB 1659-29's inferred neutrino luminosity if $Q < 0.6$. Lower values of Q may partially fit this data until the predicted mass reaches the maximum mass of the EOS, when around 10% of its core is involved in dUrca reactions, the maximum value allowed by the dUrca threshold. A similar trend is observed for the $L112.7$ EOS, with minimum Q allowed of 0.01, corresponding to approximately 50% of core volume involved in dUrca reactions. Even though the core volume percentage was calculated based on the nucleonic dUrca threshold, it could be interpreted as the core volume occupied by a given particle responsible for a less effective dUrca process, for example, near massless quarks, whose dUrca threshold coincides with their onset density. This interpretation is still bound to the error sources described at the beginning of this section, but its qualitative behavior might be accurate, raising the question of whether hybrid quark-hadron cooling is consistent with the luminosity

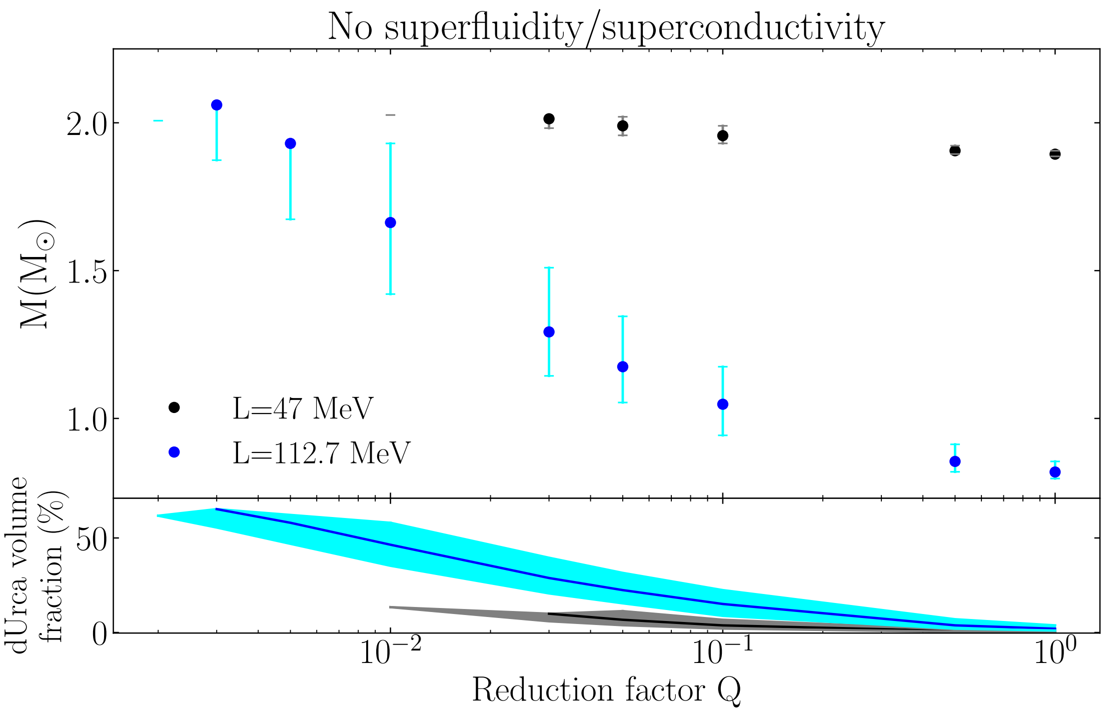

Figure 51: (Upper plot) Total masses of the neutron stars with MXB 1659-29's inferred neutrino luminosities (circles) and $1\,\sigma$ upper and lower limits (error bars), for $L47$ EOS (black) and $L112.7$ EOS (blue), with various dUrca emissivity reduction factors $Q < 1$. (Bottom plot) Percentage of core volume under direct Urca reaction for the neutron stars displayed above, for $L47$ EOS (black) and $L112.7$ EOS (blue).

of cold sources, to be investigated in subsection 4.4.2 and, with a more realistic EOS, in Chapter 5.

For completeness, I also simulate less effective dUrca processes with combinations of proton and neutron nuclear pairing models, some examples shown in Figures 52, for $L47$ EOS, and 53, for $L112.7$ EOS. This kind of simulation can be useful to qualitatively describe how nuclear pairing of particles other than neutrons and protons might affect the neutron star's dUrca luminosity. Depending on the gap model combination and EOS, smaller values of Q may increase or decrease the calculated mass range for neutron stars with MXB 1659-29's neutrino luminosity. Similarly to the results in section 4.3, the neutron star volume fraction under each pairing will be determinant to the increase or decrease in mass range, but as a rule of thumb, strong nuclear pairing gap models tend to decrease the predicted mass range with lower Q. A reduction in emissivity requires larger neutron star volumes under dUrca processes to obtain the same luminosity, which

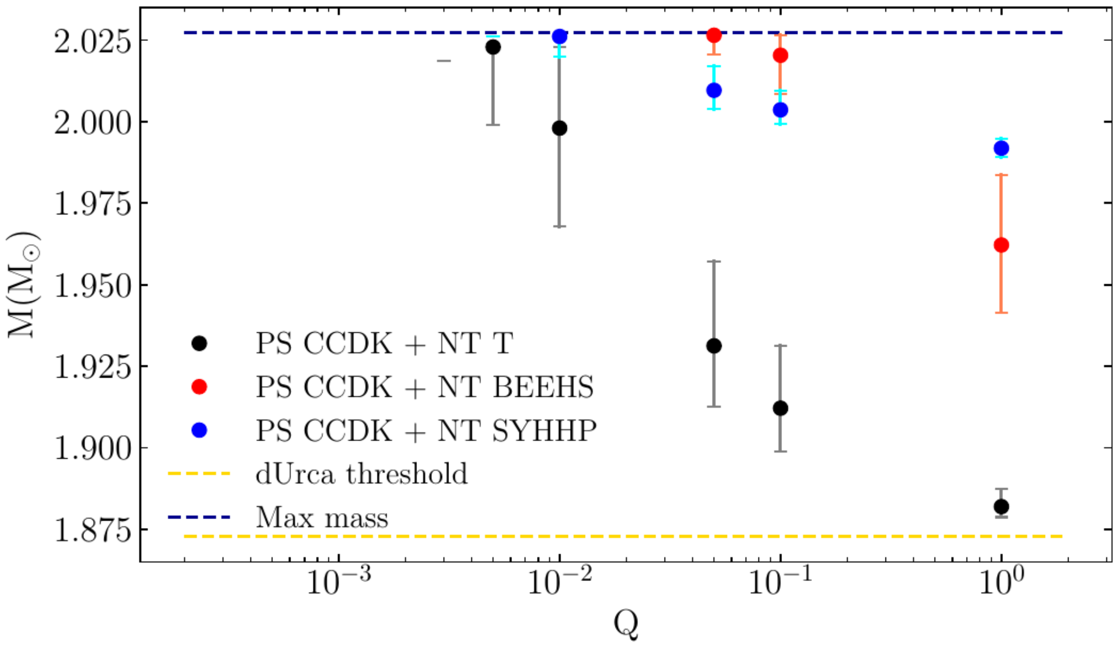

Figure 52: Total masses of the neutron stars with MXB 1659-29's inferred neutrino luminosities (circles) and 1σ upper and lower limits (error bars), for $L47$ EOS with various dUrca emissivity reduction factors $Q < 1$. Three different nuclear pairing combinations are shown: PS CCDK+NT T (black), PS CCDK+NT BEEHS (red) and PS CCDK+NT SYHHP (blue). The orange line is the dUrca threshold and the blue line, the maximum mass of that EOS.

might be impossible to reach, especially when the dUrca emissivity is already reduced by nuclear pairing.

Investigating less efficient dUrca processes is particularly interesting because their cooling signatures might be observable. In other words, cold neutron stars might only be naturally reproduced if they contain non-nucleonic particles and this situation could be checked by performing this kind of study. If eventually one succeeds in simultaneously measuring the neutron star luminosities and masses, the calculations performed here could help determining whether the equation of state is nucleonic, hadronic (that is, with heavy nucleons) or a quark-hadron hybrid. With this motivation, I integrate quark dUrca processes in the next section.

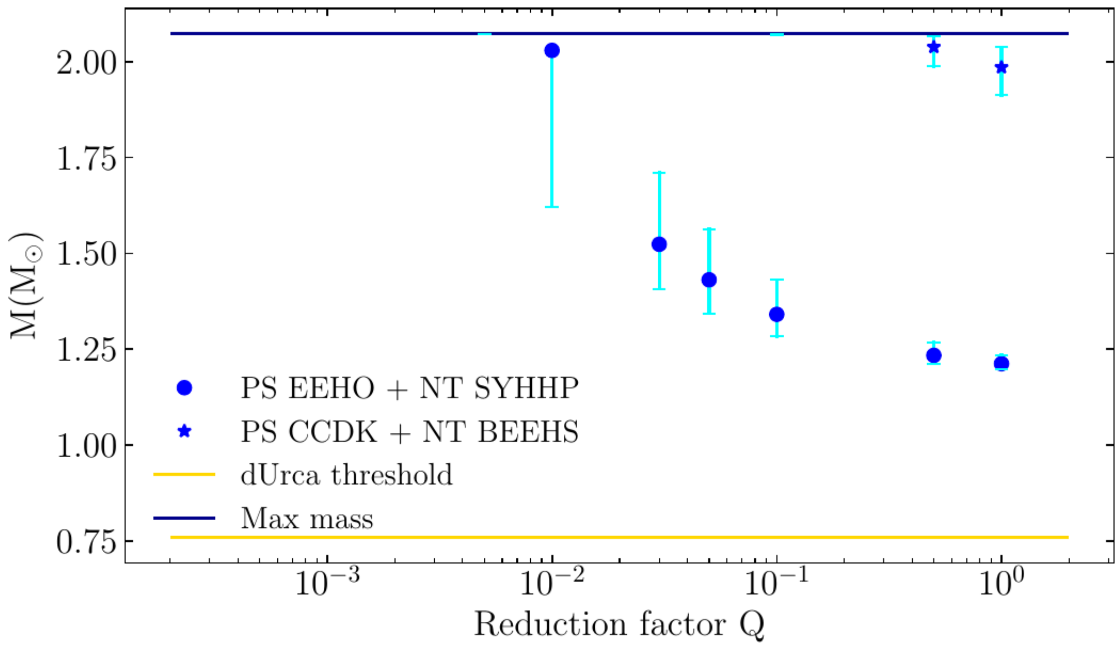

Figure 53: Same as Figure 52, but for $L112.7$ EOS and nuclear pairing combinations of PS EEHO+NT SYHHP (circles) and PS CCDK+NT BEEHS (stars).

4.4.2 *Quark dUrca*

As previously mentioned, a more realistic calculation of dUrca processes should include proper expressions for all the direct Urca cooling emissivities. Thus, I include the quark dUrca emissivity (equation 2.26) in the cooling code and investigate the scenario where the neutron star can be described by two independent EOS: one corresponding to the nucleonic part, member of the FSUGold family EOS, and another corresponding to the quark part, which is undetermined and assumed not to play a significant role in the structure of the neutron star. Hence, the TOV equations are solved as before, with the nucleonic EOS, and the effect of the quark EOS is only noted in the neutron star cooling. I take the quark-hadron phase transition density to be a free parameter one can vary, to check whether a given combination of phase transition density and EOS is inconsistent with the luminosity data. In the absence of a quark EOS, I follow the approximations of [57] and take the strong coupling constant $\alpha = 0.1$ and electron fraction $Y_e = 10^{-2}$ to calculate the quark dUrca emissivity. These values are constant through the quark phase in the neutron star core, whereas its mass density, the final ingredient needed for calculating $\epsilon_{\mathrm{q\,Urca}}$, is the nucleonic one. All of these assumptions make this scenario no more realistic than the one described at the beginning of this section, nonetheless it provides a qualitative picture of hybrid neutron stars cooling.

To reproduce MXB 1659-29's inferred luminosity, I first consider quark dUrca processes only, for simplicity, as shown in Figure 54. This scenario mimics the behavior of a hybrid neutron star whose nucleonic EOS is under very strong nuclear pairing. For $L47$, all phase transitions between saturation density $n_{\rm sat}$ and $6\,n_{\rm sat}$ are consistent with data, whereas for $L112.7$, a hybrid neutron star with phase transition at $6\,n_{\rm sat}$ with the searched neutrino luminosity would be heavier than the maximum mass star of that EOS. For both EOS, the earliest phase transition, at saturation density, predicts very light neutron stars, with $M \leq \mathrm{M}_\odot$. It could be an evidence that a phase transition at this density is disfavored, a prediction that also seems consistent with investigations of finite nuclear properties, that have systematically been probed around saturation density, and found consistent with purely nucleonic matter models [97]. Early phase transitions also imply that a large core volume fraction is in a quark phase, thus, undergoing dUrca reactions. Therefore, it could potentially mean that it would be harder for those neutron stars to reproduce the luminosity of even colder sources, that could demand even larger fractions of core volume supporting dUrca processes.

Comparing the previous scenario with the one where both quark and nucleonic dUrca cooling are allowed, I obtain Figures 55 and 56. Figure 55 simulates a first-order quark-hadron phase transition by assuming there are no nucleons in the quark phase, thus, the nucleonic dUrca emissivity starts at the dUrca threshold and ends at the phase transition density. On the other hand, for the results shown in Figure 56, I assume the nucleonic dUrca reaction can also take place in the quark phase, thus simulating a mixed phase of nucleons and quarks. In both scenarios I ignore nuclear pairing for simplicity.

Once again one observes that all phase transition densities are compatible with MXB 1659-29's inferred neutrino luminosity, however, for both the mixed and non-mixed phase, almost all $L112.7$ EOS mass predictions are below solar mass. This result can be explained by comparing these mass predictions with the purely nucleonic ones, without nuclear pairing, in Figure 16. One notes that, unless the phase transition happens around saturation density, the searched neutrino luminosity will be obtained only by the nucleonic dUrca reactions and the effect of the quark dUrca emissivity will be negligible. This

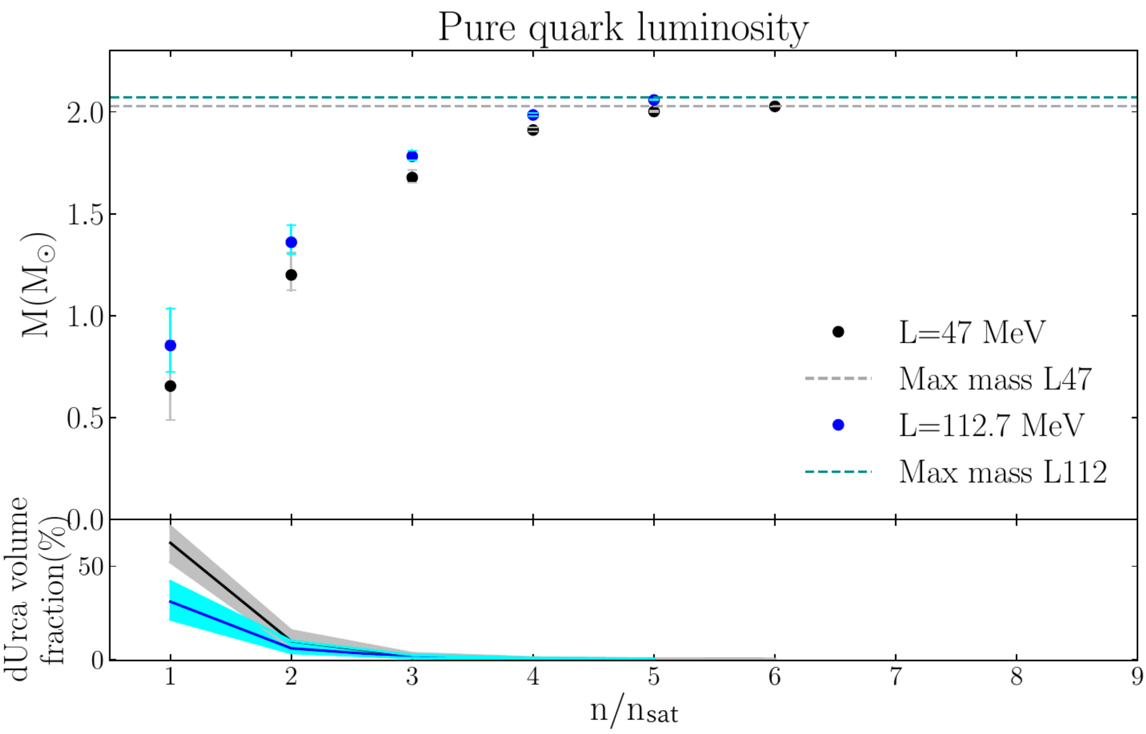

Figure 54: (Upper plot) Total masses of the neutron stars with MXB 1659-29's inferred neutrino luminosities (circles) and $1\,\sigma$ upper and lower limits (error bars) as a function of quark-hadron phase transition density, with quark dUrca neutrino luminosity only. Results for $L47$ EOS and $L112.7$ EOS are respectively shown in black and blue, along with their maximum masses (horizontal lines). (Bottom plot) Percentage of core volume under quark direct Urca reaction for the neutron stars displayed above, for $L47$ EOS (black) and $L112.7$ EOS (blue).

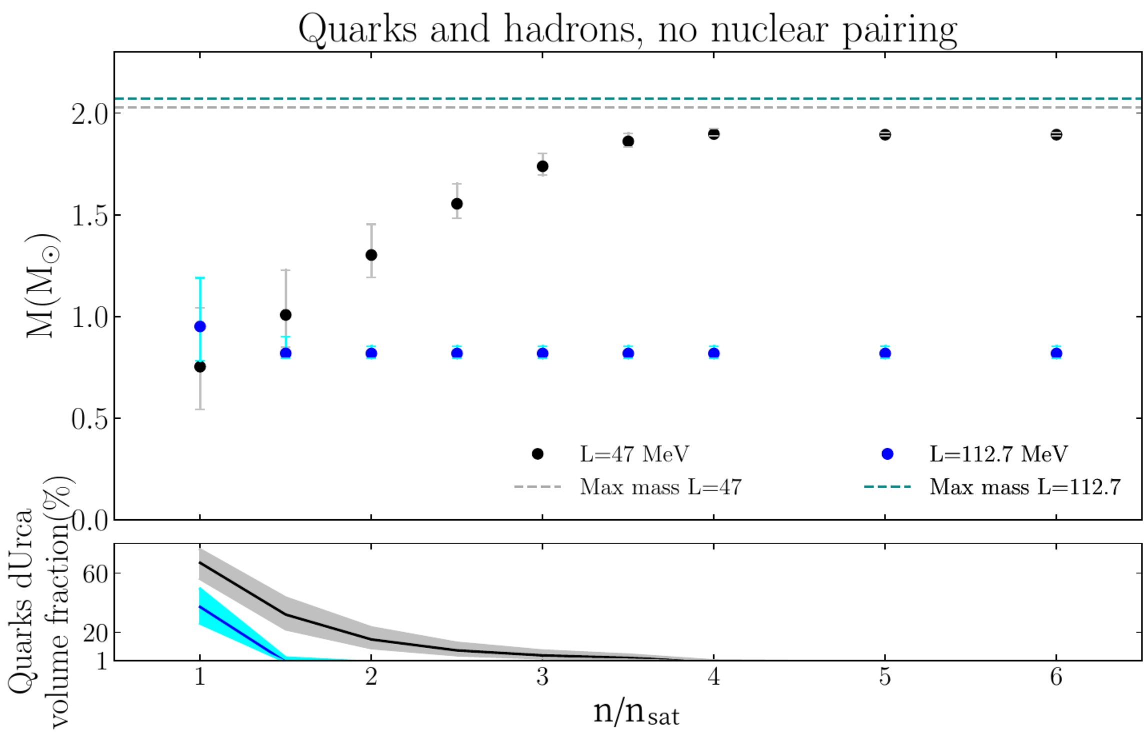

Figure 55: (Upper plot) Total masses of the neutron stars with MXB 1659-29's inferred neutrino luminosities (circles) and $1\,\sigma$ upper and lower limits (error bars) as a function of quark-hadron phase transition density, with both quark and nucleonic dUrca neutrino luminosities. Results for $L47$ EOS and $L112.7$ EOS without nuclear pairing are respectively shown in black and blue, along with their maximum masses (horizontal lines). (Bottom plot) Percentage of core volume under quark direct Urca reaction for the neutron stars displayed above, for $L47$ EOS (black) and $L112.7$ EOS (blue).

situation also happens for phase transitions $n_{\text{trans}} \geq 4\,n_{\text{sat}}$ in $L47$ EOS, that is, all phase transitions larger than the nucleonic dUrca threshold. This pattern can also be seen in the quark volume fractions getting reduced with larger phase transition densities, at the bottom plot on the Figures above. In addition, it explains why the mass predictions for the mixed and non-mixed quark-hadron phase scenarios are almost identical: whenever nucleonic dUrca processes are active, the quark dUrca contributions to the luminosity are very minor and almost undetectable.

Overall, I observe that quark-hadron phase transitions above saturation density could reproduce a cold neutron star neutrino luminosity, with mass $M > \mathrm{M}_\odot$ for all nucleonic EOS under study, taking weak nuclear pairing for small L EOS and stronger nuclear pairing for large L EOS, as seen in Figure 57. Nonetheless, one can only trust the qualitative predictions of this calculation, thus, no constraints on the quark-hadron phase transition

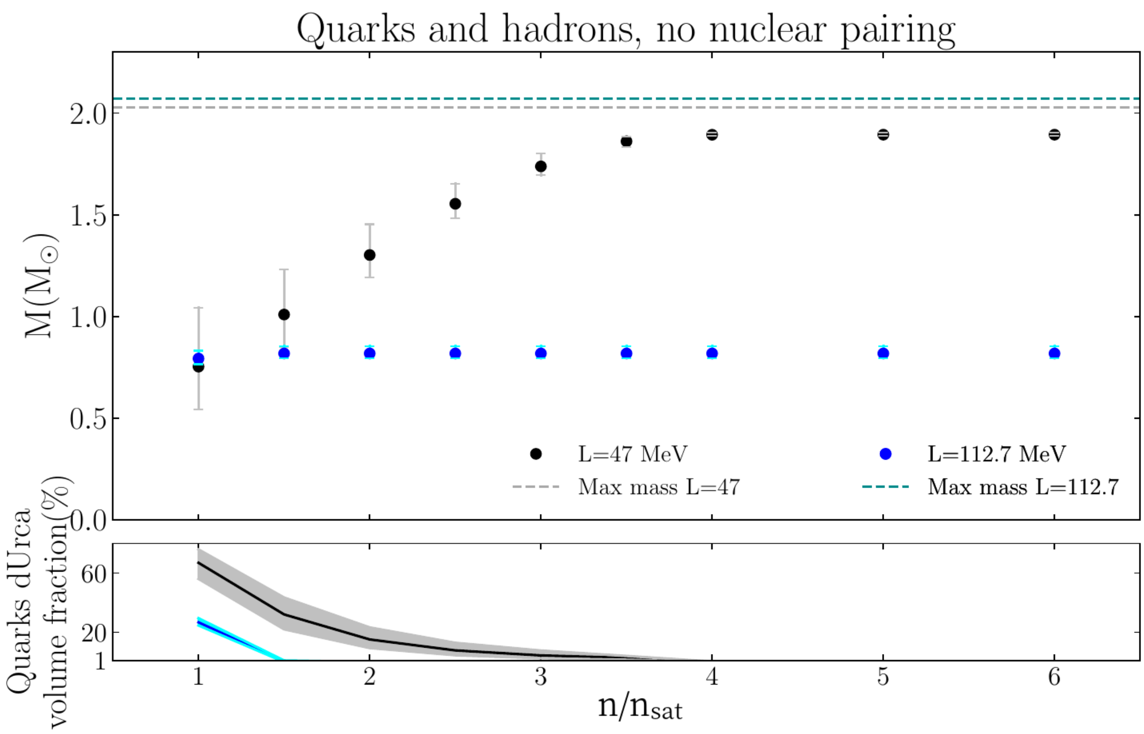

Figure 56: Same as Figure 55, but assuming a quark-hadron mixed phase. Details in the text.

density can be taken from this framework. In the next chapter, a quark EOS is taken into account and these calculations are repeated.

4.5 SUMMARY

In this chapter I confirmed that nucleonic equations of state are compatible with cold neutron star neutrino luminosities. On section 4.1, I showed that result to be true for EOS with several values of the slope of symmetry energy, L, varying from 47 to 112.7 MeV. Despite successfully reproducing the most likely values of neutrino luminosities for the two sources under study, MXB 1659-29 and SAX J1808.4-3658, when nuclear pairing is ignored, all EOS predicted a very small neutron star mass range for a given neutrino luminosity interval. In addition, large L EOS consistently produced neutron stars with total mass smaller than the solar mass when reproducing MXB 1659-29's inferred luminosity. These phenomena have been related to the cooling effectiveness of

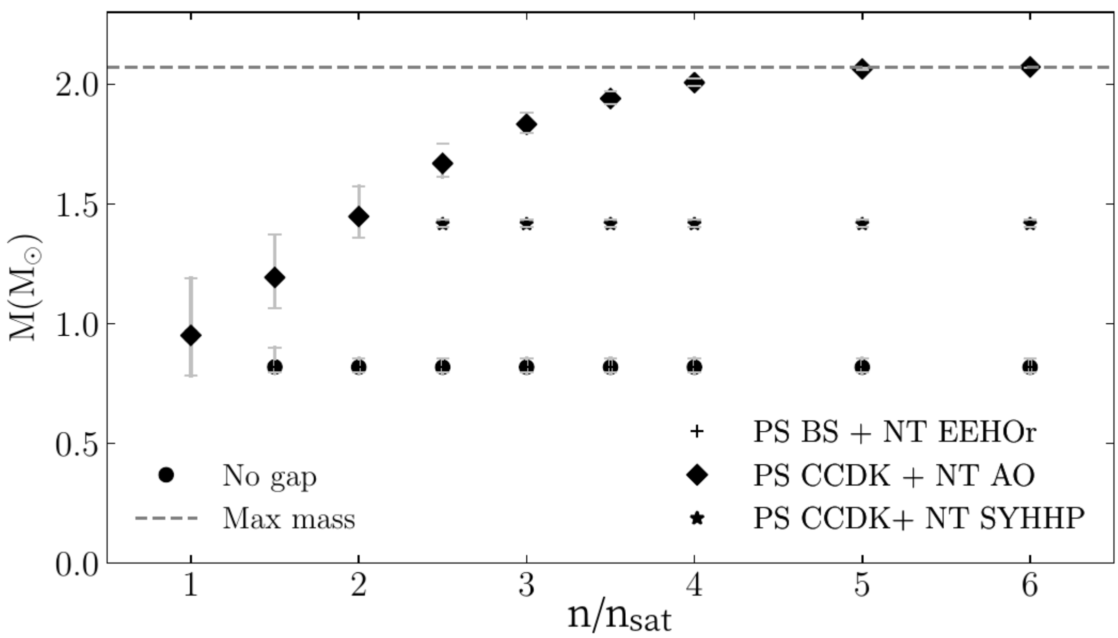

Figure 57: Total masses of the neutron stars with MXB 1659-29's 1 σ inferred neutrino luminosities as a function of quark-hadron phase transition density for $L112.7$ EOS, with both quark and nucleonic dUrca neutrino luminosities, without nuclear pairing (circles), with PS CCDK+NT AO (diamonds) and PS CCDK+NT SYHHP (stars) nuclear pairings. The weak gap model combination PS BS+NT EEHOr (plus signs) provides same results as the no-pairing case. The black dashed line represents the maximum mass for that EOS.

direct Urca reactions, which led to the confirmation of the predictions of [29], that around 1% of the core volume of MXB 1659-29 is submitted to dUrca processes.

The inclusion of nuclear pairing increased the range of predicted neutron star masses for both sources and enlarged the neutron star masses predicted by large L EOS to values above the solar mass for MXB 1659-29. These effects happened especially when the proton or neutron Cooper pairs were present for a large fraction of the neutron star volume, that is, for nuclear pairing gap models active for a large range of densities in the neutron star core. In other words, in section 4.2 I observed that, for the low temperature neutron stars whose neutrino luminosities I reproduced, the width of the nuclear pairing gap models is more important than their amplitude in determining their strength. Hence, the dUrca emissivities reduction rates of the neutron superfluidity gap models usually dominated over the proton superconductivity ones, because the latter tend to extend for larger fractions of the neutron star volume. In this context, one sees in section 4.3 that all L EOS can reproduce both sources' neutrino luminosities, given appropriate nuclear pairing models, but strong proton and neutron gap models are favored for MXB 1659-29 and, for SAX J1808.4-3658, weak nuclear pairings considering a light element envelope or strong pairings for a heavy element envelope.

Hypothetical less efficient dUrca reactions also succeeded in reproducing the neutrino luminosities of both sources. Preliminary calculations in section 4.4 artificially reduced the nucleonic dUrca emissivities while keeping their thresholds. It resulted in increased mass ranges for both sources, suggesting less effective dUrca reactions could be favored over the usual nucleonic dUrca reactions. In section 4.4.2, quark dUrca reactions are incorporated in the calculations. It is a less effective dUrca process whose emissivity is properly included but not its corresponding equation of state. Instead, I approximate that its effect in the neutron star structure is negligible and take the phase transition density as a free parameter. Even though all tested phase transitions, from n_{sat} to $6\,n_{sat}$, successfully reproduced the sources' neutrino luminosities, the low transition density of n_{sat} was excluded for consistently predicting that neutron stars with the inferred neutrino luminosity would be improbably light, with a total mass $M < M_{\odot}$. That prediction is consistent with nuclear properties experiments, that probed densities around saturation and did not find phase transition signatures. Thus, overall, quark dUrca reactions are consistent with cold neutron star luminosities and their reproduction might help constrain the quark-hadron phase transition density, especially for small L EOS. On the other hand, the quark dUrca contribution to the total neutrino luminosity is minimal if the nucleonic EOS has a large L and its effects might go unnoticed or be mistaken for nuclear pairing reductions. These results might change once a realistic quark EOS is considered, as will be done in the next chapter.

5

NEUTRON STAR COOLING WITH HYBRID QUARK-HADRON EQUATIONS OF STATE

In this chapter, I incorporate a quark equation of state, described in Chapter 3, to models of hybrid quark-hadron neutron stars and reproduce the inferred neutrino luminosities of MXB 1659-29 and SAX J1808.4-3658. In section 5.1, I compare the general features of the results of the cooling calculations focusing on the different equations of state, their nucleonic dUrca thresholds, and quark phase transitions. Then, I discuss the predicted masses for the hybrid stars in section 5.2, focusing on the equations of state whose nucleonic part has $L = 50$ MeV in section 5.2.1, and $L = 90$ MeV in section 5.2.2. A brief summary with the main conclusions is given in section 5.3.

5.1 NEUTRINO LUMINOSITY CURVES

Following the procedure described in Chapter 3, I create first-order phase transitions with nucleonic EOS named after their slope of symmetry energy, L, effective masses, m^*, and vector self-interaction coupling ζ. In the nucleonic $L50$ family, I chose L 50 MeV, m^* 0.60, ζ 0 and L 50 MeV, m^* 0.60, ζ 0.02 EOS and in the $L90$ family, L 90 MeV, m^* 0.55, ζ 0.02 and L 90 MeV, m^* 0.60, ζ 0.02 EOS. Their saturation densities, nucleonic dUrca thresholds and maximum masses are given in tables 3 and 4. I include the corresponding dUrca threshold neutron star masses for reference, but once the phase transitions are built, I effectively work with hybrid EOS that can be softer or stiffer than the purely nucleonic one, so both the masses m_{dUrca} and m_{max}, shown in the tables for neutron stars, can change substantially when dealing with hybrid stars.

In tables 5 and 6, I show the parameters of the quark-hadron phase transitions built. The values of the phase transition pressures p_{trans} were chosen from the diagrams in

Table 3: Saturation density (n_{sat}), dUrca threshold density (n_{dUrca}), dUrca threshold mass (m_{dUrca}) and maximum mass without quarks (m_{max}) for L 50 MeV, m^* 0.60, ζ 0 EOS (first line) and L 50 MeV, m^* 0.60, ζ 0.02 EOS (second line).

$n_{\text{sat}}\,(1/fm^3)$	$n_{\text{dUrca}}\,(n_{\text{sat}})$	$m_{\text{dUrca}}\,(M_\odot)$	$m_{\text{max}}\,(M_\odot)$
0.1517	3.51	2.58	2.70
0.1513	3.55	1.87	2.09

Table 4: Same as table 3, but for L 90 MeV, m^* 0.55, ζ 0.02 EOS (first line) and L 90 MeV, m^* 0.60, ζ 0.02 EOS (second line).

$n_{\text{sat}}\,(1/fm^3)$	$n_{\text{dUrca}}\,(n_{\text{sat}})$	$m_{\text{dUrca}}\,(M_\odot)$	$m_{\text{max}}\,(M_\odot)$
0.1463	1.77	1.01	2.19
0.1489	1.78	0.92	2.11

Chapter 3 to obtain hybrid stars compatible with astrophysical data, for the lowest and largest possible density transitions, n_{trans}. For most of the hybrid EOS used in this project, the allowed density range was heavily constrained, with densities from only approximately n_{sat} to $2\,n_{\text{sat}}$ fitting the data. In addition, I have varied the energy density jump at the phase transition, $\Delta\epsilon$, for the hybrid EOS built with the L 50 MeV, m^* 0.60, ζ 0 EOS, with $p_{\text{trans}} = 38$ MeV (table 5, bottom left), to compare its effects in the cooling calculations.

For all EOS, I observe that the phase transition density is an important reference not only because one wants to exclude phase transitions inconsistent with data, but also because comparing it with the dUrca threshold is a simple way to estimate which dUrca processes will be dominant in the hybrid star cooling. Phase transition densities larger than the nucleonic dUrca threshold indicate that nucleonic dUrca processes become active before the phase transition, thus, their larger emissivity will potentially dominate the neutrino cooling. These cases are marked with a star in tables 5 and 6. On the other hand, when the dUrca threshold is larger than the phase transition density, nucleonic dUrca reactions are never allowed and the total neutrino luminosity of the hybrid star is given by quark dUrca reactions only. This is the case of most of the hybrid EOS built in this work.

The neutrino luminosity curves shown in this chapter include only direct Urca reactions. As explained in Chapter 2, fast cooling processes are necessary to reproduce the luminosity of the MXB 1659-29 and SAX J1808.4-3658 neutron stars, so I make an ap-

Table 5: Parameters of the hybrid EOS built with nucleonic EOS L 50 MeV, m^* 0.60, ζ 0 (left) and L 50 MeV, m^* 0.60, ζ 0.02 (right). Transition pressure (p_{trans}) and energy density jump ($\Delta\epsilon$) given in MeV, transition density (n_{trans}) given in terms of saturation density (n_{sat}). The cases where nucleonic dUrca processes are allowed are marked with a star.

L 50 MeV, m^* 0.60, ζ 0	L 50 MeV, m^* 0.60, ζ 0.02
$p_{trans} = 3,\ \ \Delta\epsilon = 170,\ \ n_{trans} = n_{sat}$	$p_{trans} = 5,\ \ \Delta\epsilon = 180,\ \ n_{trans} = 1.2\,n_{sat}$
$p_{trans} = 6,\ \ \Delta\epsilon = 260,\ \ n_{trans} = 1.29\,n_{sat}$	$p_{trans} = 35,\ \ \Delta\epsilon = 241,\ \ n_{trans} = 2.2\,n_{sat}$
$p_{trans} = 38,\ \ \Delta\epsilon = 236,\ \ n_{trans} = 2\,n_{sat}$	$*p_{trans} = 205,\ \ \Delta\epsilon = 200,\ \ n_{trans} = 4.6\,n_{sat}$
$p_{trans} = 38,\ \ \Delta\epsilon = 280,\ \ n_{trans} = 2\,n_{sat}$	

Table 6: Same as table 5, but for nucleonic EOS L 90, m^* 0.55, ζ 0.02 (left) and L 90, m^* 0.60, ζ 0.02 (right).

L 90 MeV, m^* 0.55, ζ 0.02	L 90 MeV, m^* 0.60, ζ 0.02
$p_{trans} = 4,\ \ \Delta\epsilon = 130,\ \ n_{trans} = n_{sat}$	$p_{trans} = 3.2,\ \ \Delta\epsilon = 132,\ \ n_{trans} = 0.9\,n_{sat}$
$*p_{trans} = 36,\ \ \Delta\epsilon = 220,\ \ n_{trans} = 2.18\,n_{sat}$	$p_{trans} = 7,\ \ \Delta\epsilon = 285,\ \ n_{trans} = 1.28\,n_{sat}$
$*p_{trans} = 38,\ \ \Delta\epsilon = 296,\ \ n_{trans} = 2.2\,n_{sat}$	$*p_{trans} = 42,\ \ \Delta\epsilon = 255,\ \ n_{trans} = 2.37\,n_{sat}$

proximation that the influence of other cooling reactions such as modified Urca in this source is negligible. In this context, the generic behavior of the neutrino luminosity versus mass curves when only quark dUrca reactions are active can be seen in Figure 58. For phase transitions around $2\,n_{sat}$ or larger densities, indicated by the red and orange curves in the Figure, the neutrino luminosity monotonically increases, similarly to the nucleonic dUrca luminosity curves seen in the previous chapter. However, hybrid EOS with lower density phase transitions, i.e. the blue and yellow curves with smaller values of p_{trans}, generate a two-peaked curve, with a local maximum obtained for neutron stars with masses $M \leq M_\odot$ and a global maximum for masses $M \geq 2\,M_\odot$. A large fraction of quarks in the neutron star generates those peaks in the luminosity curve, as can be seen by comparing the blue curve in Figure 58 with its corresponding mass-radius diagram in Figure 59. The luminosity peaks when the hybrid stars have a large quark core ratio, that is, when the fraction $(M_{quarks}/R_{quarks})/(M_{total}/R_{total})$ increases, which happens in smaller scale for $M \leq 0.5\,M_\odot$ after the phase transition and, in larger scale, when the star reaches its maximum mass and maximum neutrino luminosity.

Another situation in which the neutrino luminosity versus mass curve does not monotonically increase is when both nucleonic and quark dUrca processes are active. Some examples are shown in the curves with the largest p_{trans} in Figures 60, 61 and 62. In

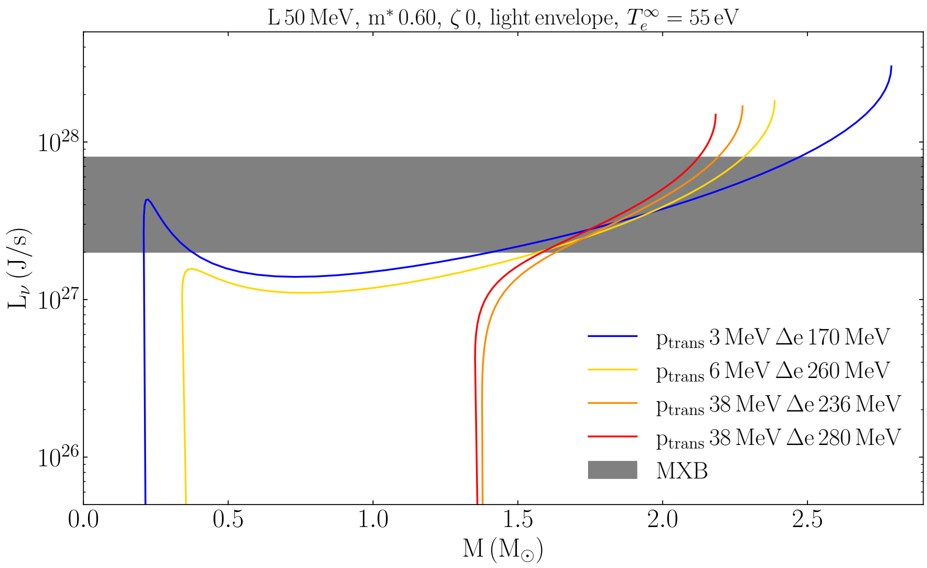

Figure 58: Direct Urca neutrino luminosities (in J/s) and total masses of all stable hybrid stars built with nucleonic EOS L 50 MeV, m^* 0.60, ζ 0, for $T_e^\infty = 55$ eV and light element envelope composition. Solid colorful lines represent different phase transitions, labelled in the Figure, and the horizontal grey area marks the lower and upper limits of MXB 1659-29's inferred neutrino luminosity.

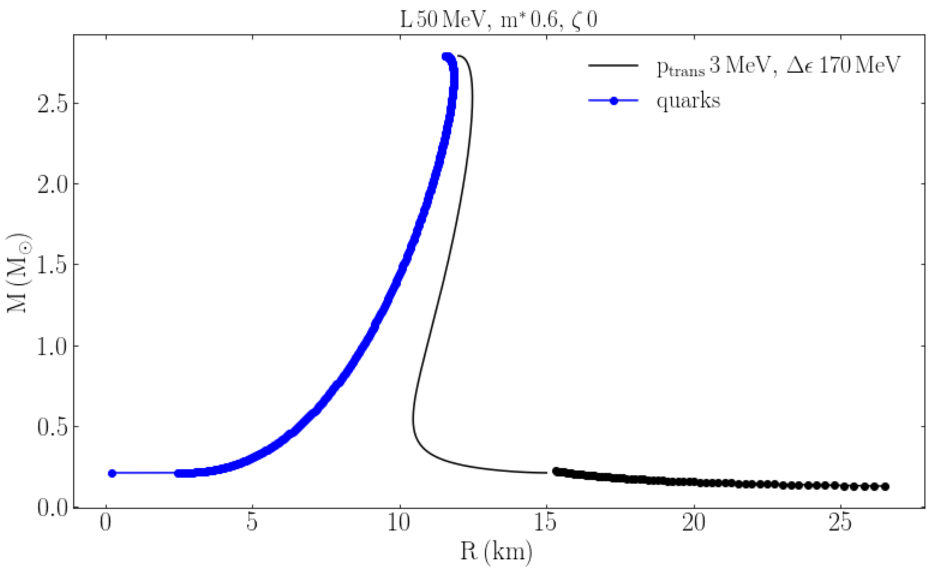

Figure 59: Total masses and radii of all stable hybrid stars with EOS L 50 MeV, m^* 0.60, ζ 0, $p_{trans} =$ 3 MeV, $\Delta\epsilon = 170$ MeV. Black points correspond to stars within the first stable branch of their mass-radius diagram and the solid black line, to stars within its second stable branch. The blue dotted line shows the total mass and radii of the quark core of all the hybrid stars represented.

all these cases, a global neutrino luminosity peak is obtained before the quark phase transition, with nucleonic dUrca processes. The second branch of the luminosity curve is produced by quark dUrca processes only, which tend to achieve lower neutrino luminosities, unless nuclear pairing is included, suppressing the nucleonic dUrca emissivity.

Figures 58, 60, 61 and 62 can also be used to understand the influence of L, m^* and ζ in hybrid stars cooling, taking as an example the effective temperature $T_e^\infty = 55$ eV and a light element envelope composition. Comparing the table entries for L 50 MeV, m^* 0.60, ζ 0.02 and L 90, m^* 0.60, ζ 0.02 EOS, I observe that, as expected, a large L EOS has a lower dUrca threshold. However, the softness of a large L EOS prevents us from building large density quark phase transitions still compatible with astrophysical data. Hence, one ends up observing nucleonic dUrca reactions for hybrid EOS built with both values of L, because one can either build phase transitions at large densities, beyond the dUrca threshold, for small L EOS, or build phase transitions at small densities, that nonetheless are still above the low dUrca threshold of large L EOS. This context explains the difference between the shapes of the neutrino luminosity curves seen in Figures 60 and 62. When the quark phase transition happens for the $L50$ EOS, at a large density, most of the volume of the hybrid star consists of nucleonic matter, hence, quark dUrca domination only happens for the heaviest hybrid stars, such that one can only see its effect at the very end of the luminosity curve. The opposite scenario happens for hybrid stars built with $L90$ EOS, where a large portion of the luminosity curve is dominated by quark dUrca cooling, for all stars with $M \geq 1.4\,\mathrm{M}_\odot$.

The effect of ζ is found comparing the L 50 MeV, m^* 0.60, ζ 0 EOS and the L 50 MeV, m^* 0.60, ζ 0.02 EOS. From table 3, it is evident that ζ strongly affects m_{dUrca} and m_{max}, illustrating its influence in the high density part of nucleonic EOS. That influence can also be seen in the softness of larger ζ EOS, which accommodates larger quark phase transitions, eventually allowing for the onset of nucleonic dUrca processes. Finally, comparing the EOS from table 4, one observes that the effect of m^* in the neutrino luminosity curves is minor and no qualitative difference between the results in Figures 61 and 62 was present.

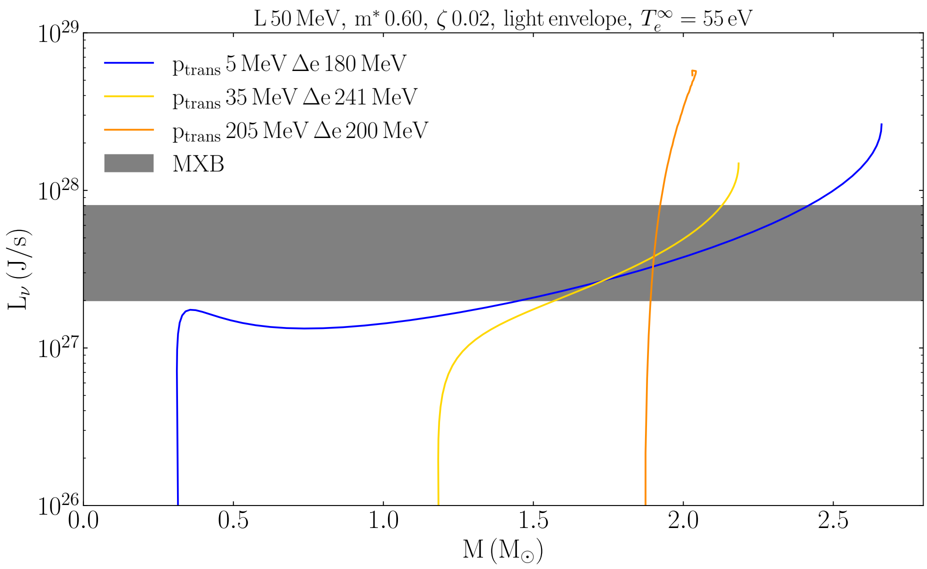

Figure 60: Direct Urca neutrino luminosities (in J/s) and total masses of all stable hybrid stars built with nucleonic EOS L 50 MeV, m^* 0.60, ζ 0.02, for $T_e^\infty = T = 55$ eV and light element envelope composition. Nuclear pairing effects in the nucleonic phase are ignored. Solid colorful lines represent different phase transitions, labelled in the Figure, and the horizontal grey area marks the lower and upper limits of MXB 1659-29's inferred neutrino luminosity.

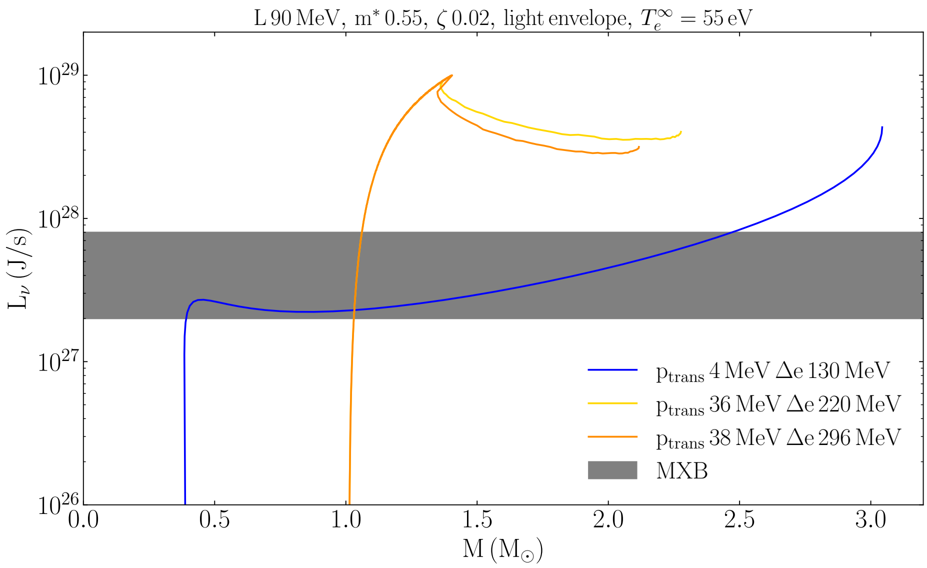

Figure 61: Same as Figure 60, but for hybrid stars built with nucleonic EOS L 90 MeV, m^* 0.55, ζ 0.02.

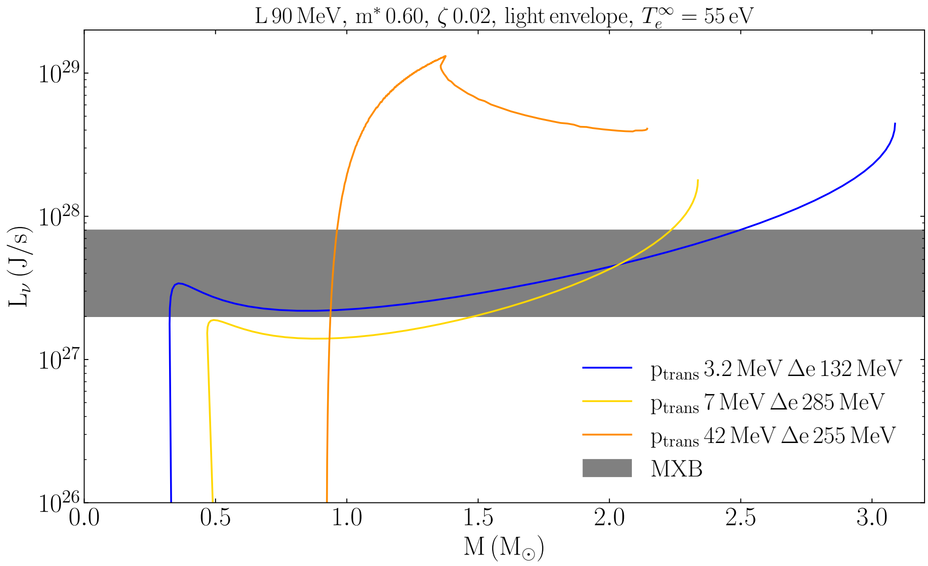

Figure 62: Same as Figure 60, but for hybrid stars built with nucleonic EOS L 90 MeV, m^* 0.60, ζ 0.02.

5.2 HYBRID STAR MASSES

Knowing the total neutrino luminosity of hybrid stars, given a temperature and envelope composition, I repeat the calculations of the previous chapter to reproduce the inferred luminosities of MXB 1659-29 and SAX J1808.4-3658. Depending on the equation of state and quark phase transition density, these luminosities can be reached with quark dUrca processes only, nucleonic dUrca processes only or a combination of them. As in the previous chapter, I calculate the range of masses corresponding to the lower and upper limits of neutrino luminosity for each source and verify whether all EOS fit the cooling data, as well as which phase transitions return the largest mass ranges for a given source. For simplification, I disregard hybrid stars with masses $M < M_\odot$ in this analysis, because I assume they are not realized in nature.

5.2.1 *L50 EOS*

Starting with hybrid EOS with a nucleonic *L*50 part, that represent hybrid EOS with a low L nucleonic phase, I reproduce MXB 1659-29's inferred neutrino luminosity, again assuming $T_e^\infty = 55$ eV and a light element envelope composition. In Figure 63, I display

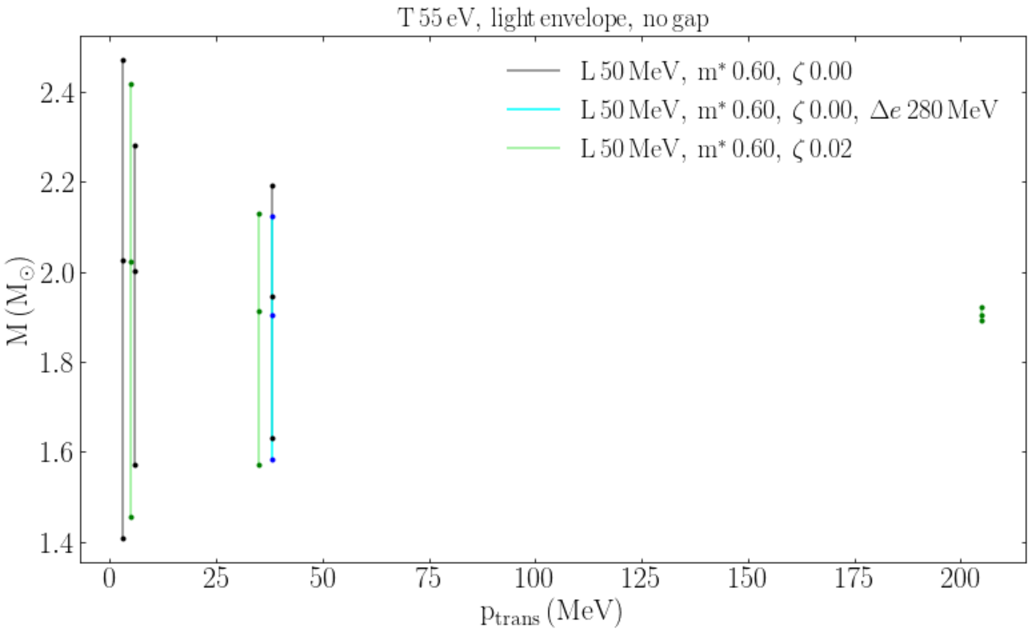

Figure 63: Total masses of the hybrid stars with MXB 1659-29's lower, most likely and upper inferred neutrino luminosities, built with nucleonic EOS L 50 MeV, m^* 0.60, ζ 0 (in black) and nucleonic EOS L 50 MeV, m^* 0.60, ζ 0.02 (in green). The pressure transitions p_{trans} (MeV) are represented in the x-axis and nuclear pairing effects in the nucleonic phase are ignored. The blue line and points mark the special case of L 50 MeV, m^* 0.60, ζ 0, $p_{trans} = 38$ MeV, $\Delta\epsilon = 280$ MeV.

the calculated range of masses of the hybrid stars with the inferred luminosities, aggregating the results of L 50 MeV, m^* 0.60, ζ 0 and L 50 MeV, m^* 0.60, ζ 0.02 in a single Figure. For a given phase transition, the points in the Figure represent the calculated masses of hybrid stars with the upper, most likely and lower limits of neutrino luminosity, in order of decreasing mass.

MXB 1659-29's neutrino luminosity is achieved for all of the constructed quark phase transitions of both $L50$ EOS. The source's inferred luminosities are reached with quark dUrca processes only, except for the L 50 MeV, m^* 0.60, ζ 0.02, p_{trans} 205 MeV EOS, in which it is obtained with nucleonic dUrca processes only. In Figure 63 I show its corresponding hybrid star mass assuming no nuclear pairing is active. The blue range highlighted in the Figure corresponds to the L 50 MeV, m^* 0.60, ζ 0, p_{trans} 38 MeV, $\Delta\epsilon$ 280 MeV EOS, to differentiate it from the results of the $\Delta\epsilon$ 236 MeV phase transition, in black, with same p_{trans}. One observes that a larger $\Delta\epsilon$ makes no qualitative difference to the mass range, only predicting slightly smaller masses to the hybrid star with the inferred luminosity. Comparing the two EOS one also observes that the effect of ζ in the mass range is imperceptible, thus, the pressure transition p_{trans} is the determining factor in the size of the mass range.

Overall, the pattern of smaller mass ranges for larger p_{trans} is clear in Figure 63. Following the reasoning explained in the previous chapter, I interpret that EOS predicting larger mass ranges for a given neutrino luminosity interval are more likely to describe stars with those luminosities. Hence, these results seem to disfavor large quark phase transitions, with $n_{trans} \geq 4\,n_{sat}$, for $L50$ EOS. This pattern is also observed when reproducing SAX J1808.4-3658 neutrino luminosity, for both light and heavy elements envelope compositions. Comparing Figures 64 and 65, displaying the lower and upper limits of T_e^∞ for that source, I observe that EOS with low phase transitions are unable to reproduce the lower limit of SAX J1808.4-3658 neutrino luminosity, if the hybrid star mass $M \geq \mathrm{M}_\odot$, regardless of their effective temperature T_e^∞ and envelope composition. On the other hand, quark phase transitions around $2\,n_{sat}$ and a light element envelope fit the cooling data and predict a reasonable mass range for hybrid stars, for $T_e^\infty = 40 - 36$ eV. The lower temperature limit for that source, of $T_e^\infty = 28$ eV, seems incompatible with its inferred neutrino luminosity for the $L50$ EOS investigated here, with both light and heavy element envelopes.

5.2.1.1 *Nuclear pairing*

Similarly to the results of the previous chapter, the mass range of hybrid stars with the required luminosity is very small when reached with only nucleonic dUrca processes, ignoring nuclear pairing. In this case, adding neutron and proton pairing may increase the calculated mass range, as seen in Figure 66, comparing the no pairing curve (in black), that predicts a mass range of approximately $M = 1.89 - 1.925\,\mathrm{M}_\odot$, and the PS AO+NT TTav curve (in green), with mass range of approximately $M = 1.97 - 2.04\,\mathrm{M}_\odot$. Nonetheless this slight increase in mass range is still considerably smaller than the increase I obtained for the smaller density phase transitions, when quark dUrca reactions happened in a large fraction of the neutron star volume.

Furthermore, including nuclear pairing in the nucleonic phase does not always increase the range of calculated hybrid star masses. This is the case of the other two curves in Figure 66, in which nuclear pairing strongly suppresses the nucleonic dUrca rates

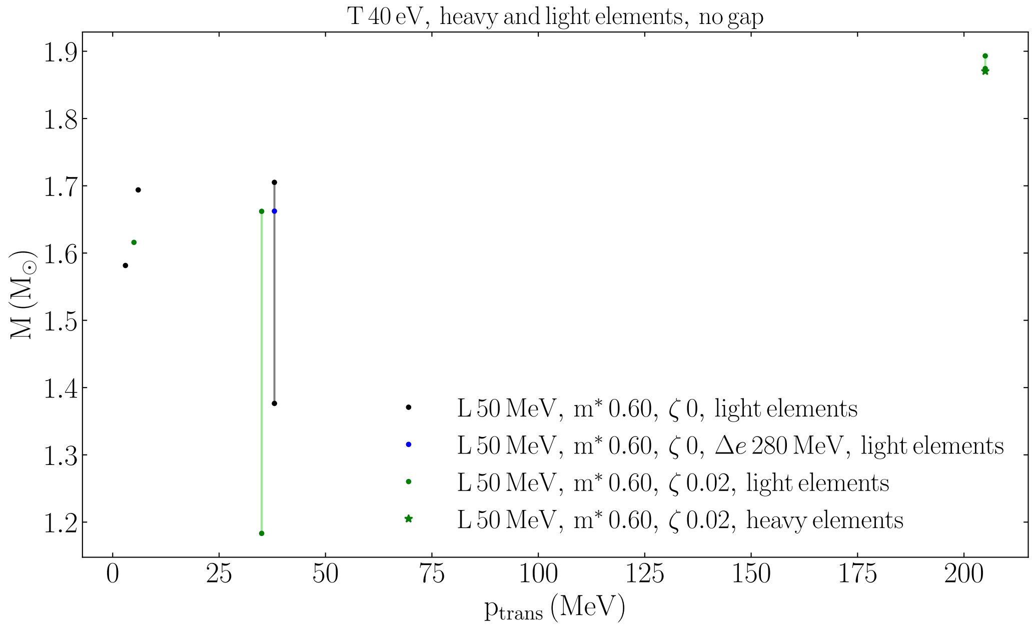

Figure 64: Total masses of the hybrid stars with SAX J1808.4-3658's lower and upper inferred neutrino luminosities, assuming $T_e^\infty = T = 40$ eV and nucleonic EOS L 50 MeV, m^* 0.60, ζ 0 with light elements envelope composition (in black), nucleonic EOS L 50 MeV, m^* 0.60, ζ 0.02 with light elements envelope composition (green points) and nucleonic EOS L 50 MeV, m^* 0.60, ζ 0.02 with heavy elements envelope composition (green stars). The pressure transitions $\mathrm{p_{trans}}$ (MeV) are represented in the x-axis and nuclear pairing effects in the nucleonic phase are ignored. The blue line and points mark the special case of L 50 MeV, m^* 0.60, ζ 0, $\mathrm{p_{trans}} = 38$ MeV, $\Delta\epsilon = 280$ MeV, with light elements envelope composition.

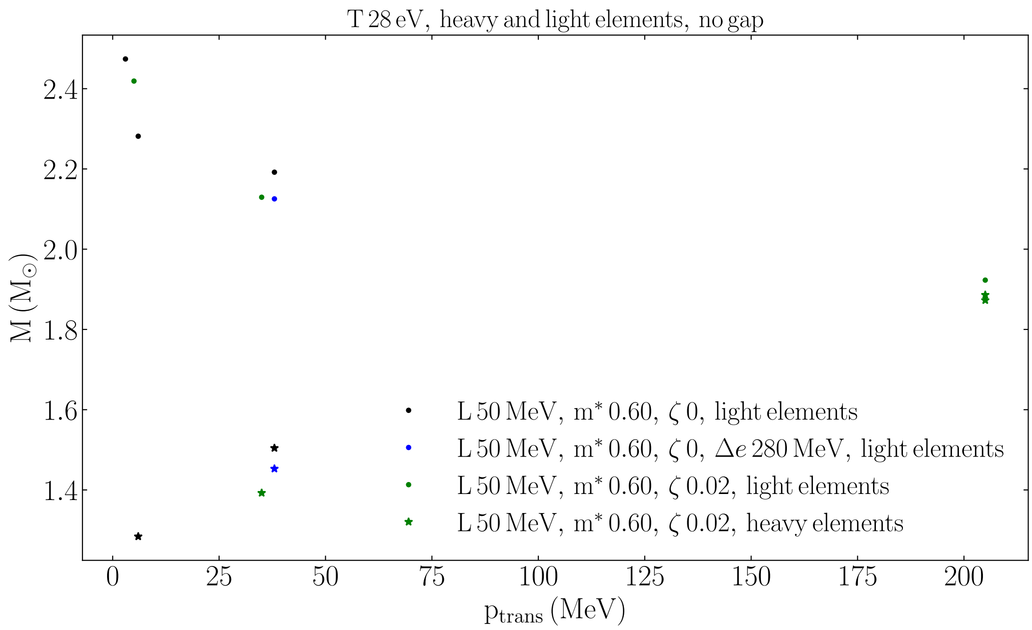

Figure 65: Same as Figure 64, but with $T_e^\infty = 28$ eV.

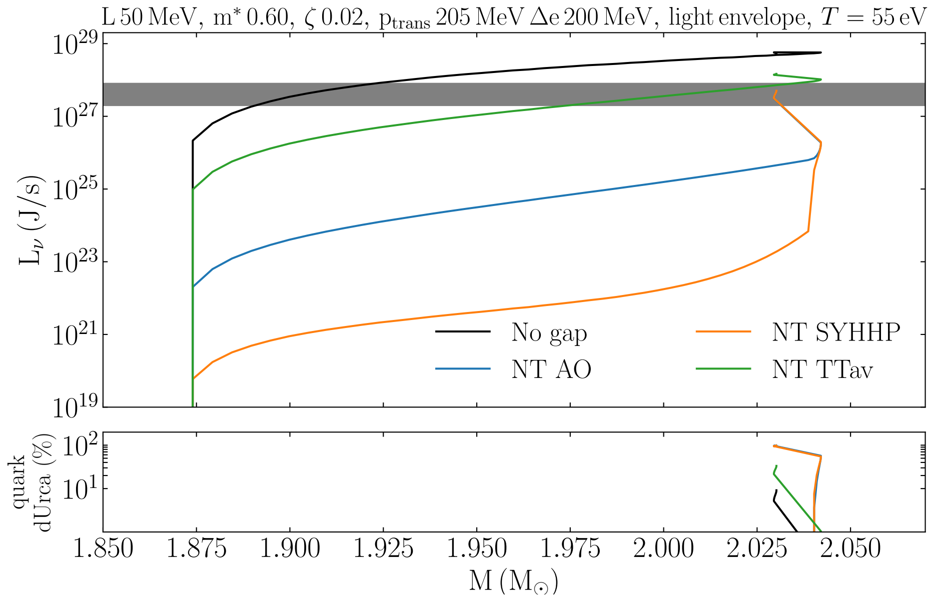

Figure 66: (Upper plot) Total direct Urca neutrino luminosities (in J/s) and total masses of all stable hybrid stars built with nucleonic EOS L 50 MeV, m^* 0.60, ζ 0.02, and phase transition p_{trans} = 205 MeV, $\Delta\epsilon$ = 200 MeV for $T_e^\infty = T$ = 55 eV and light element envelope composition. The black curve represents no nuclear pairing in the nucleonic phase and the colorful curves, combinations of PS AO and different neutron superfluidity nuclear pairing gap models in the nucleonic phase, labelled in the Figure. The horizontal grey area marks the lower and upper limits of MXB 1659-29's inferred neutrino luminosity. (Bottom plot) Percentage of quark dUrca luminosity contribution to the total dUrca luminosity shown above. The PS AO+NT AO combination curve (in blue) lies below the PS AO+NT SYHHP curve (in orange).

and the inferred neutrino luminosities can only be achieved in the quark phase. For this particular EOS, because of its large phase transition density, only very heavy hybrid stars have enough of their volume undergoing quark dUrca processes to reach the upper limit of inferred neutrino luminosity, hence the final result is a reduced mass range that might not even reach the 1σ limits of the sources' neutrino luminosities. The lower dUrca threshold of L90 EOS changes this scenario, as will be seen in the next section.

5.2.2 *L90 EOS*

The softness of the L90 nucleonic EOS leads to overall lower quark phase transition densities for the quark-hadron hybrid EOS, which in this framework represent hybrid EOS with a large L nucleonic phase. They have generated the mass ranges shown in Figure 67,

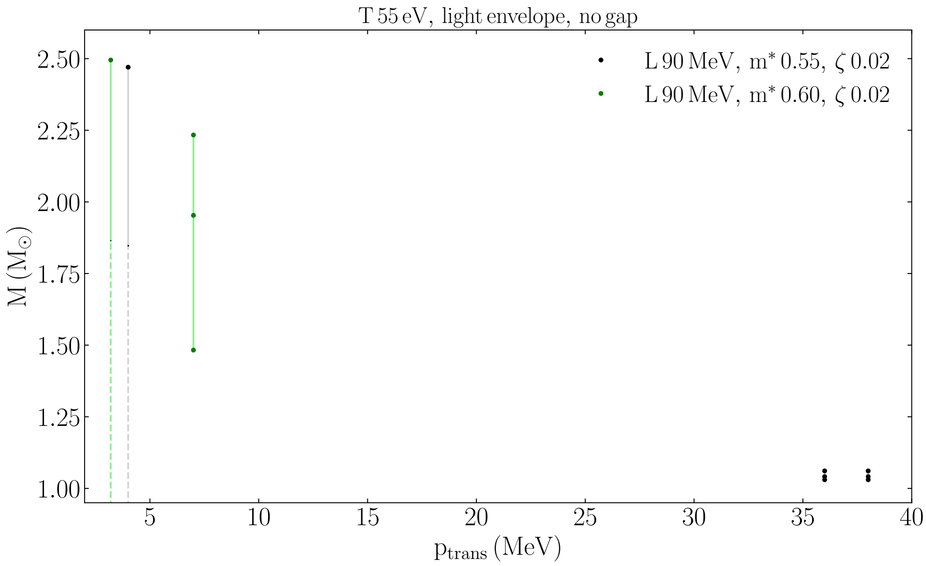

Figure 67: Total masses of the hybrid stars with MXB 1659-29's lower, most likely and upper inferred neutrino luminosities, built with nucleonic EOS L 90 MeV, m^* 0.55, ζ 0.02 (in black) and nucleonic EOS L 90 MeV, m^* 0.60, ζ 0.02 (in green). The pressure transitions p_{trans} (MeV) are represented in the x-axis and nuclear pairing effects in the nucleonic phase are ignored. The dashed lines indicate luminosity limits reached for hybrid stars with masses $M < M_\odot$.

for stars with MXB 1659-29's inferred luminosity. All hybrid EOS with $p_{trans} < 10$ MeV reach the luminosities with quark dUrca processes only, and the hybrid EOS with the smallest phase transitions, $p_{trans} < 5$, even reach the lower limit of neutrino luminosity for stars with $M < M_\odot$, indicated by the dashed lines in this Figure. Hence, the general conclusion that large phase transition densities generate smaller mass ranges, thus, are potentially disfavored, is also valid for $L90$ EOS, especially when nuclear pairing is ignored. This result is particularly evident for the largest phase transition density of L 90 MeV, m^* 0.60, ζ 0.02, with p_{trans} 42 MeV and $\Delta\epsilon$ 255 MeV, not shown in Figure 67, due to its inability to reproduce any of the inferred luminosities for realistic hybrid stars, that is, with masses above the solar mass.

Including nuclear pairing does not change this conclusion, but it tends to increase the range of predicted masses for hybrid stars with large phase transitions, as shown in Figures 68 and 69. A good illustration to explain this phenomenon is seen in Figure 70. It shows that, unlike the $L50$ EOS cases, a major increase in mass range originates from nuclear pairing reduction of nucleonic dUrca emissivity that leads to quark dUrca

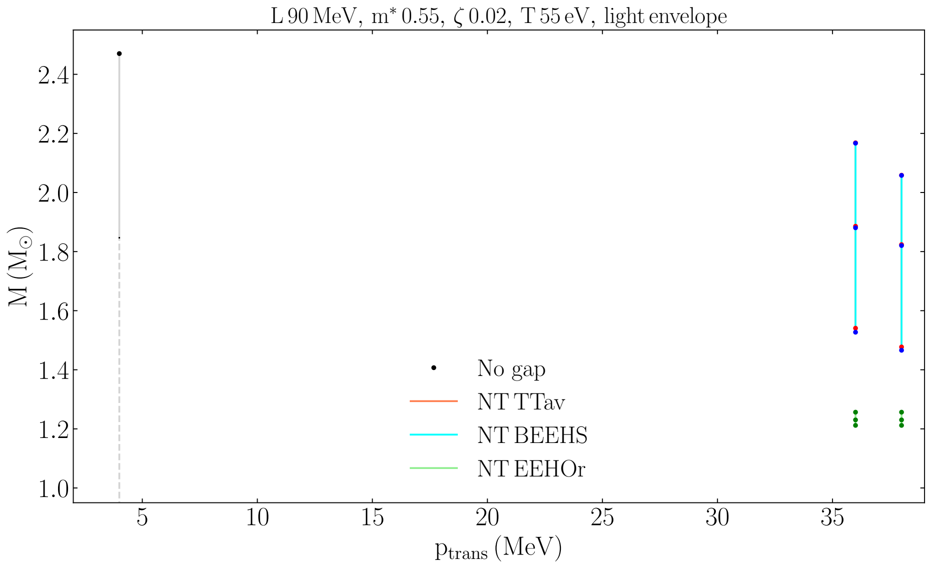

Figure 68: Total masses of the hybrid stars with MXB 1659-29's lower, most likely and upper inferred neutrino luminosities, built with nucleonic EOS L 90 MeV, m^* 0.55, ζ 0.02. The pressure transitions $\mathrm{p_{trans}}$ (MeV) are represented in the x-axis. The black line corresponds to the no-pairing case and the colorful lines, to different combinations of PS AO and NT pairing models, as indicated in the labels. The dashed black line indicates luminosity limits reached for hybrid stars with masses $M < \mathrm{M}_\odot$.

processes dominating for most of the volume of the hybrid star. Hence, strong nuclear pairing models are needed to increase the mass range of hybrid stars with $\mathrm{n_{trans}} \leq 2\,\mathrm{n_{sat}}$.

5.3 SUMMARY

Comparing the results of sections 5.2.1 and 5.2.2, $L90$ hybrid EOS consistently predict larger mass ranges than the ones obtained in Chapter 4 for stars with MXB 1659-29 and SAX J1808.4-3658 inferred neutrino luminosities. This conclusion holds whether or not one includes nuclear pairing in the nucleonic phase, hence, the neutrino cooling results of this chapter suggest hybrid EOS built with large L nucleonic EOS are favored over those with a small L nucleonic EOS. However, $L90$ hybrid EOS only supports small density quark-hadron phase transitions, with $\mathrm{n_{trans}} \leq 2.4\,\mathrm{n_{sat}}$, which suggests that cooling data favours very early quark phase transitions. This general conclusion was already observed studying $L50$ hybrid EOS' mass ranges, thus, it appears not to be specific to a nucleonic equation of state, but instead, to the lower effectiveness of quark dUrca reactions. Nonetheless, known nuclear properties show no evidence of a phase transition at

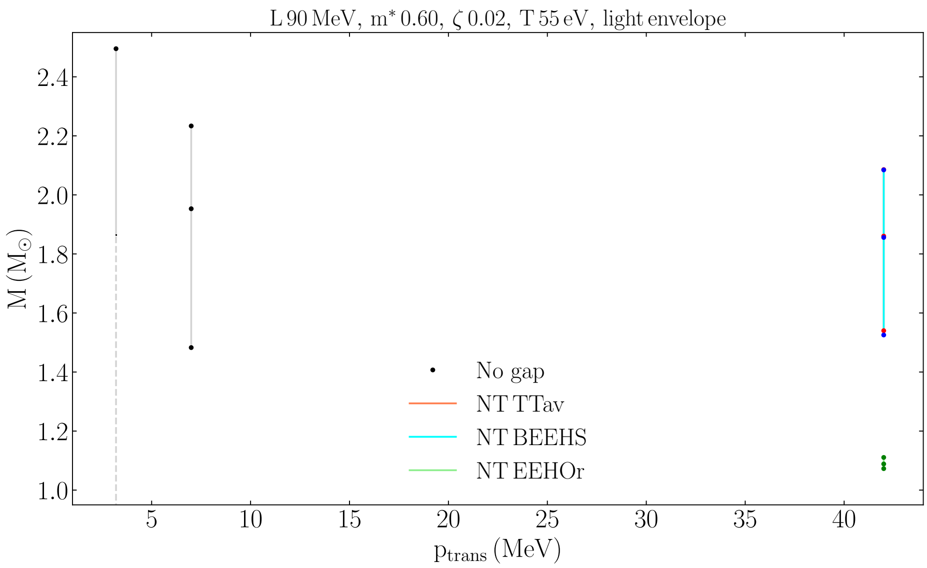

Figure 69: Total masses of the hybrid stars with MXB 1659-29's lower, most likely and upper inferred neutrino luminosities, built with nucleonic EOS L 90 MeV, m^* 0.60, ζ 0.02. The pressure transitions p_{trans} (MeV) are represented in the x-axis. The black lines correspond to the no-pairing case and the colorful lines, to different combinations of PS CCYms and NT pairing models, as indicated in the labels. The dashed black line indicates luminosity limits reached for hybrid stars with masses $M < M_{\odot}$.

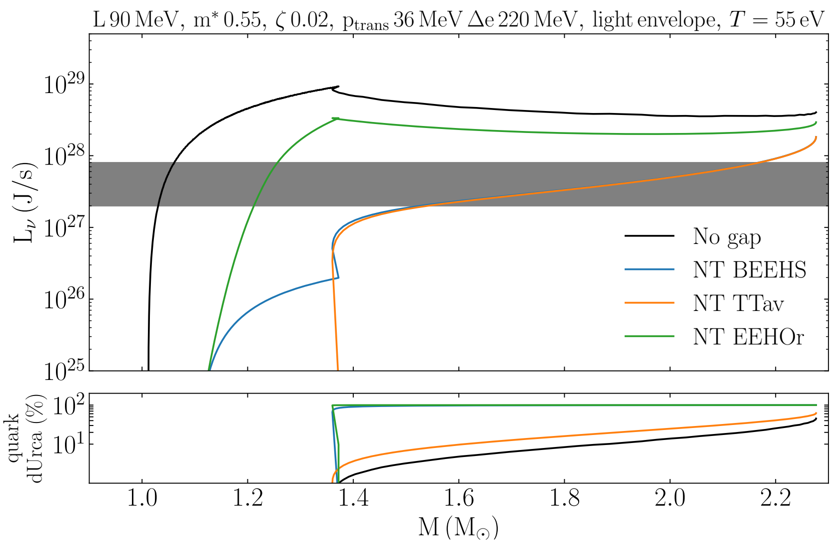

Figure 70: (Upper plot) Total direct Urca neutrino luminosities (in J/s) and total masses of all stable hybrid stars built with nucleonic EOS L 90 MeV, m^* 0.55, ζ 0.02, and phase transition $p_{\text{trans}} = 36$ MeV, $\Delta\epsilon = 220$ MeV for $T_e^{\infty} = T = 55$ eV and light element envelope composition. The black curve represents no nuclear pairing in the nucleonic phase and the colorful curves, combinations of PS CCYms and different neutron superfluidity nuclear pairing gap models in the nucleonic phase, labelled in the Figure. The horizontal grey area marks the lower and upper limits of MXB 1659-29's inferred neutrino luminosity. (Bottom plot) Percentage of quark dUrca luminosity contribution to the total dUrca luminosity shown above.

n_{sat}, thus, quark phase transitions at this value of density are not compatible with data. Hence, there seems to exist only a small interval of quark phase transition densities, between $n_{sat} < n_{trans} \leq 2.4\,n_{sat}$, compatible with all nuclear and astronomical observations as well as with the cooling results shown in this chapter. Even though the nucleonic EOS with L 50 MeV, m^* 0.60, ζ 0.02 supports larger quark phase transition densities, the range of masses predicted for their hybrid stars is too small and it cannot be significantly increased with nuclear pairing models.

In this analysis, it is crucial to understand the difference in effectiveness of nucleonic and quark dUrca emissivities. Their ratio, which is independent of the source's temperature, is shown on Figure 71 for all EOS studied in this work. One observes that nucleonic dUrca reactions are, at most, around only 10 times more effective than quark dUrca reactions, a ratio very similar to all EOS, peaking at low densities. Even though the value of this ratio is a consequence of the estimates I made for the strong coupling constant, $\alpha = 0.12$, and the electron fraction, $Y_e = 10^{-5}$, in the quark phase, the order of magnitude of these values is not expected to be substantially different in realistic quark EOS. Since the difference in effectiveness of dUrca processes is not large, the second most important factor in determining the total dUrca neutrino luminosity of an hybrid star becomes the volume fraction undergoing each process. This fraction is mostly determined by the size of the hybrid star and the nucleonic equation of state, which will set the nucleonic dUrca threshold, and whose stiffness will limit the density of quark phase transitions resulting in hybrid stars compatible with astronomical data, as discussed in Chapter 3. All these factors considered, the investigated framework is able to reproduce all current data for all hybrid EOS under study, however, they might not offer the most natural explanation for the cooling data.

An alternative interpretation to the results obtained in this chapter is that less effective non-quark dUrca processes, such as direct Urca reactions with hyperons or other heavier particles, are favored to reproduce the neutrino luminosity of cold neutron stars. They could potentially reproduce the sources' inferred neutrino luminosities for a larger mass range of neutron stars, providing a more natural explanation to their low luminosities. Nonetheless, studying these processes requires completely different hadronic equations of state, which is out of the scope of this work.

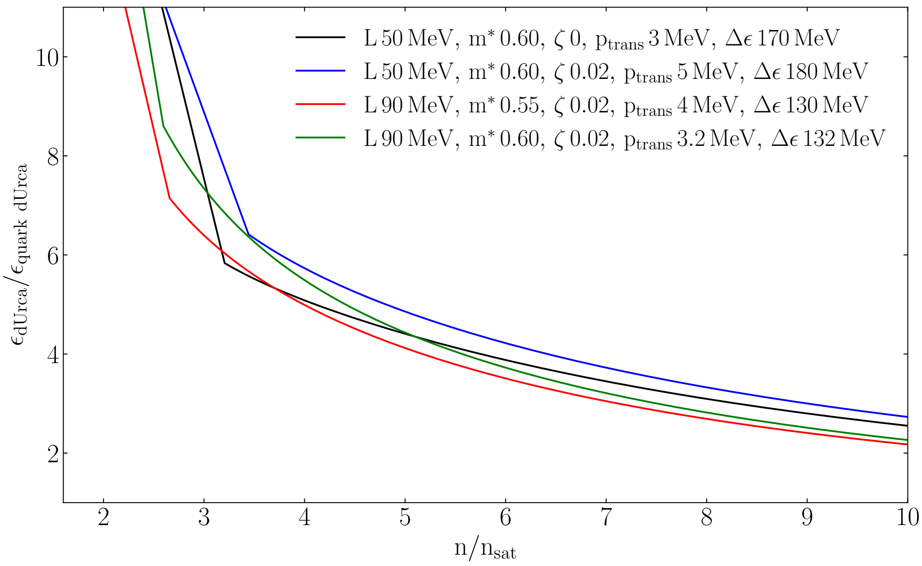

Figure 71: Ratio of nucleonic dUrca emissivity ($\epsilon_{\mathrm{dUrca}}$) to quark dUrca emissivity ($\epsilon_{\mathrm{quark\,dUrca}}$), assuming these reactions are simultaneously active for all $n \geq 2\,\mathrm{n_{sat}}$. Colorful lines represent different hybrid EOS.

Part IV

CONCLUSION

Overall summary and final remarks

6

CONCLUSION

This research has investigated neutron star cooling to check whether the neutrino luminosities of cold neutron stars can be reproduced by nucleonic and quark-hadron hybrid equations of state. This study has focused on a family of relativistic mean field nucleonic EOS with varied values of the slope of symmetry energy L, from 47 to 112.7 MeV. Nuclear pairing models have also been included, in an attempt to determine the most likely scenarios to reproduce the inferred neutrino luminosities of the neutron stars in MXB 1659-29 and SAX J1808.4-3658.

This type of study is motivated by advances in both nuclear experiments and astrophysical observations, that have probed the behavior of matter at low and high densities, but whose limitations have not allowed the determination of the neutron star equation of state yet. Nevertheless, they have constrained the possible neutron star EOS, as described in Chapter 1. A particular point of interest is the particle content of compact stars and which observables are sensitive to it. Neutron star luminosity and heat capacity are investigated in this context, especially because nucleonic and hybrid quark-hadron contents have specific signatures that could potentially be detected in the observations or inferences of those quantities. This is the topic of Chapter 2, that also describes in detail how nuclear pairing adds to the complexity of this framework.

The equations of state used in this work for both the nucleonic and the hybrid neutron stars are detailed in Chapter 3. In that chapter, I also discuss the influence of different EOS to the neutron star cooling calculations, in particular their nucleonic dUrca thresholds. The results of the cooling simulations are shown in Chapter 4, where I test the compatibility of all nucleonic EOS with the inferred neutrino luminosities of MXB 1659-29 and SAX J1808.4-3658. One observes that, even though all investigated EOS can generate neutron stars with those neutrino luminosities, large L EOS need strong nuclear pairing to produce stars above solar mass for MXB 1659-29. Furthermore, a variation of approximately one order of magnitude in neutrino luminosity for that source results in a very small range of predicted masses, around $0.02\,M_{\odot}$, for most EOS and nuclear pairing combinations, because of great cooling efficiency of nucleonic dUrca processes. A qualitatively similar picture is reproduced for SAX J1808.4-3658, with the difference that when taking a light element envelope composition for that source one should use weak nuclear pairings to reproduce its luminosity and strong nuclear pairings if a heavy element composition is considered. I also show that, for both sources, by combining their inferred neutrino luminosities with their temperature variations after some time in quiescence, one can estimate their heat capacities, which are directly related to the neutron star particle composition, thus can constrain their equation of state and nuclear pairing models.

Starting in Chapter 4, less efficient dUrca processes were investigated as a way to increase the predicted neutron star mass ranges. Preliminary calculations that did not incorporate a quark EOS, but only its dUrca emissivity, successfully reproduced both sources' neutrino luminosities for all tested phase transitions, resulting in increased mass ranges. However, they consistently predicted masses smaller than the solar mass when the phase transition happened at saturation density, thus that phase transition density was excluded, in agreement with nuclear experiment observations, that do not observe phase transition signatures at low densities. When a realistic quark EOS was included, leading to the appearance of hybrid twin stars, in Chapter 5, this result changed. The softness of hybrid EOS contributed to increase the mass ranges of the stars with the inferred luminosities, especially for low phase transition densities. Larger phase transition densities, when allowed by data constraints, could also reproduce the sources' neutrino luminosities but they either returned a very small mass range, that could not be increased even with nuclear pairing, or the phase transitions were still relatively small, around $2\,n_{sat}$.

This research concludes that while one can build nucleonic and quark-hadron hybrid stars that are compatible with MXB 1659-29 and SAX J1808.4-3658 luminosities for all values of L, other EOS might reproduce their luminosities more naturally. That could be case, for example, of equations of state with heavy hadronic particles that participate in less effective dUrca reactions, especially if they consistently lead to a broad mass range for neutron stars with varied luminosities. Future observations can help to further constrain the possible neutron star equations of state, by informing with more precision on its properties, so I look forward to the next limits on neutron star tidal deformabilities, mass, radius and luminosities.

BIBLIOGRAPHY

[1] Dmitrii G Yakovlev, Pawel Haensel, Gordon Baym, and Christopher Pethick. "Lev Landau and the concept of neutron stars." In: *Physics-Uspekhi* 56.3 (2013), pp. 289–295. DOI: 10.3367/ufne.0183.201303f.0307.

[2] J. Schaffner-Bielich. *Compact Star Physics*. Cambridge University Press, 2020. ISBN: 9781107180895.

[3] W. Baade and F. Zwicky. "Remarks on Super-Novae and Cosmic Rays." In: *Phys. Rev.* 46 (1 1934), pp. 76–77. DOI: 10.1103/PhysRev.46.76.2. URL: https://link.aps.org/doi/10.1103/PhysRev.46.76.2.

[4] P. Haensel, A.Y. Potekhin, and D.G. Yakovlev. *Neutron Stars 1: Equation of State and Structure*. Astrophysics and Space Science Library. Springer New York, 2006. ISBN: 9780387335438. URL: https://books.google.com.br/books?id=iIrj9nfHnesC.

[5] Pablo Cerda-Duran and Nancy Elias-Rosa. "The physics and astrophysics of neutron stars." In: ed. by Luciano Rezzolla, Pierre Pizzochero, David Ian Jones, Nanda Rea, and Isaac Vidaña. Astrophysics and space science library. Switzerland: Springer, 2018. Chap. Neutron stars formation and core-collapse supernovae, pp. 1–56. ISBN: 978-3-319-97616-7.

[6] J. R. Oppenheimer and G. M. Volkoff. "On Massive Neutron Cores." In: *Phys. Rev.* 55 (4 1939), pp. 374–381. DOI: 10.1103/PhysRev.55.374. URL: https://link.aps.org/doi/10.1103/PhysRev.55.374.

[7] Richard C. Tolman. "Static Solutions of Einstein's Field Equations for Spheres of Fluid." In: *Phys. Rev.* 55 (4 1939), pp. 364–373. DOI: 10.1103/PhysRev.55.364. URL: https://link.aps.org/doi/10.1103/PhysRev.55.364.

[8] L.D. Landau. “8 - ON THE THEORY OF STARS.” In: *Collected Papers of L.D. Landau*. Ed. by D. TER HAAR. Pergamon, 1965, pp. 60–62. ISBN: 978-0-08-010586-4. DOI: https://doi.org/10.1016/B978-0-08-010586-4.50013-4. URL: https://www.sciencedirect.com/science/article/pii/B9780080105864500134.

[9] Laura Tolos and Laura Fabbietti. “Strangeness in Nuclei and Neutron Stars.” In: *Prog. Part. Nucl. Phys.* 112 (2020), p. 103770. DOI: 10.1016/j.ppnp.2020.103770. arXiv: 2002.09223 [nucl-ex].

[10] S. Gandolfi, J. Lippuner, A. W. Steiner, I. Tews, X. Du, and M. Al-Mamun. “From the microscopic to the macroscopic world: from nucleons to neutron stars.” In: *J. Phys. G* 46.10 (2019), p. 103001. DOI: 10.1088/1361-6471/ab29b3. arXiv: 1903.06730 [nucl-th].

[11] Farrooh Fattoyev. “Sensitivity of neutron star properties to the equation of state.” PhD thesis. The Florida State University, Oct. 2011.

[12] Aleksi Kurkela, Eduardo S. Fraga, Jürgen Schaffner-Bielich, and Aleksi Vuorinen. “Constraining neutron star matter with Quantum Chromodynamics.” In: *Astrophys. J.* 789 (2014), p. 127. DOI: 10.1088/0004-637X/789/2/127. arXiv: 1402.6618 [astro-ph.HE].

[13] B. G. Todd-Rutel and J. Piekarewicz. “Neutron-Rich Nuclei and Neutron Stars: A New Accurately Calibrated Interaction for the Study of Neutron-Rich Matter.” In: *Phys. Rev. Lett.* 95 (12 2005), p. 122501. DOI: 10.1103/PhysRevLett.95.122501. URL: https://link.aps.org/doi/10.1103/PhysRevLett.95.122501.

[14] Feryal Özel and Paulo Freire. “Masses, Radii, and the Equation of State of Neutron Stars.” In: *Annual Review of Astronomy and Astrophysics* 54.1 (2016), pp. 401–440. DOI: 10.1146/annurev-astro-081915-023322.

[15] H. T. Cromartie et al. “Relativistic Shapiro delay measurements of an extremely massive millisecond pulsar.” In: *Nature Astron.* 4.1 (2019), pp. 72–76. DOI: 10.1038/s41550-019-0880-2. arXiv: 1904.06759 [astro-ph.HE].

[16] Thomas E. Riley et al. “A *NICER* View of PSR J0030+0451: Millisecond Pulsar Parameter Estimation.” In: *Astrophys. J. Lett.* 887.1 (2019), p. L21. DOI: 10.3847/2041-8213/ab481c. arXiv: 1912.05702 [astro-ph.HE].

[17] M. C. Miller et al. “PSR J0030+0451 Mass and Radius from *NICER* Data and Implications for the Properties of Neutron Star Matter.” In: *Astrophys. J. Lett.* 887.1 (2019), p. L24. DOI: 10.3847/2041-8213/ab50c5. arXiv: 1912.05705 [astro-ph.HE].

[18] A. J. Dittmann S. Bogdanov Z. Arzoumanian K. C. Gendreau S. Guillot W. C. G. Ho J. M. Lattimer M. Loewenstein S. M. Morsink P. S. Ray M. T. Wolff C. L. Baker T. Cazeau S. Manthripragada C. B. Markwardt T. Okajima S. Pollard I. Cognard H. T. Cromartie E. Fonseca L. Guillemot M. Kerr A. Parthasarathy T. T. Pennucci S. Ransom I. Stairs M. C. Miller F. K. Lamb. “The Radius of PSR J0740+6620 from NICER and XMM-Newton Data.” In: *The Astrophysical Journal Letters* 918.2 (Sept. 2021). DOI: 10.3847/2041-8213/ac089b.

[19] Thomas E. Riley et al. “A NICER View of the Massive Pulsar PSR J0740+6620 Informed by Radio Timing and XMM-Newton Spectroscopy.” In: *Astrophys. J. Lett.* 918.2 (2021), p. L27. DOI: 10.3847/2041-8213/ac0a81. arXiv: 2105.06980 [astro-ph.HE].

[20] B. P. Abbott et al. “GW170817: Observation of Gravitational Waves from a Binary Neutron Star Inspiral.” In: *Phys. Rev. Lett.* 119 (16 2017), p. 161101. DOI: 10.1103/PhysRevLett.119.161101. URL: https://link.aps.org/doi/10.1103/PhysRevLett.119.161101.

[21] B. P. Abbott et al. “Properties of the Binary Neutron Star Merger GW170817.” In: *Phys. Rev. X* 9 (1 2019), p. 011001. DOI: 10.1103/PhysRevX.9.011001. URL: https://link.aps.org/doi/10.1103/PhysRevX.9.011001.

[22] D.G. Yakovlev, A.D. Kaminker, O.Y. Gnedin, and P. Haensel. “Neutrino emission from neutron stars.” In: *Physics Reports* 354.1 (2001), pp. 1–155. ISSN: 0370-1573. DOI: https://doi.org/10.1016/S0370-1573(00)00131-9. URL: https://www.sciencedirect.com/science/article/pii/S0370157300001319.

[23] Spencer Beloin, Sophia Han, Andrew W. Steiner, and Dany Page. “Constraining Superfluidity in Dense Matter from the Cooling of Isolated Neutron Stars.” In: *Phys. Rev. C* 97.1 (2018), p. 015804. DOI: 10.1103/PhysRevC.97.015804. arXiv: 1612.04289 [nucl-th].

[24] A. Y. Potekhin, M. E. Gusakov, and A. I. Chugunov. *Thermal evolution of neutron stars in soft X-ray transients with thermodynamically consistent models of the accreted crust*. Pre-print. 2023. DOI: https://doi.org/10.48550/arXiv.2303.08716. arXiv: 2303.08716 [astro-ph.HE].

[25] D. Viganò, N. Rea, J. A. Pons, R. Perna, D. N. Aguilera, and J. A. Miralles. "Unifying the observational diversity of isolated neutron stars via magneto-thermal evolution models." In: *Monthly Notices of the Royal Astronomical Society* 434.1 (July 2013), pp. 123–141. ISSN: 0035-8711. DOI: 10.1093/mnras/stt1008. eprint: https://academic.oup.com/mnras/article-pdf/434/1/123/18498733/stt1008.pdf. URL: https://doi.org/10.1093/mnras/stt1008.

[26] Clara Dehman, José A Pons, Daniele Viganò, and Nanda Rea. "How bright can old magnetars be? Assessing the impact of magnetized envelopes and field topology on neutron star cooling." In: *Monthly Notices of the Royal Astronomical Society: Letters* 520.1 (Jan. 2023), pp. L42–L47. ISSN: 1745-3925. DOI: 10.1093/mnrasl/slad003. eprint: https://academic.oup.com/mnrasl/article-pdf/520/1/L42/48803647/slad003.pdf. URL: https://doi.org/10.1093/mnrasl/slad003.

[27] V. Dexheimer, R. O. Gomes, T. Klähn, S. Han, and M. Salinas. "GW190814 as a massive rapidly rotating neutron star with exotic degrees of freedom." In: *Phys. Rev. C* 103.2 (2021), p. 025808. DOI: 10.1103/PhysRevC.103.025808. arXiv: 2007.08493 [astro-ph.HE].

[28] Potekhin, A. Y., Chugunov, A. I., and Chabrier, G. "Thermal evolution and quiescent emission of transiently accreting neutron stars." In: *A&A* 629 (2019), A88. DOI: 10.1051/0004-6361/201936003. URL: https://doi.org/10.1051/0004-6361/201936003.

[29] Edward F. Brown, Andrew Cumming, Farrukh J. Fattoyev, C.J. Horowitz, Dany Page, and Sanjay Reddy. "Rapid Neutrino Cooling in the Neutron Star MXB 1659-29." In: *Physical Review Letters* 120.18 (2018). DOI: 10.1103/physrevlett.120.182701. URL: https://doi.org/10.1103%2Fphysrevlett.120.182701.

[30] F. J. Fattoyev and J. Piekarewicz. "Relativistic models of the neutron-star matter equation of state." In: *Phys. Rev. C* 82 (2 2010), p. 025805. DOI: 10.1103/PhysRevC.82.025805. URL: https://link.aps.org/doi/10.1103/PhysRevC.82.025805.

[31] M. B. Tsang et al. "Constraints on the symmetry energy and neutron skins from experiments and theory." In: *Phys. Rev. C* 86 (2012), p. 015803. DOI: 10.1103/PhysRevC.86.015803. arXiv: 1204.0466 [nucl-ex].

[32] Wynn C. G. Ho, Khaled G. Elshamouty, Craig O. Heinke, and Alexander Y. Potekhin. "Tests of the nuclear equation of state and superfluid and superconducting gaps using the Cassiopeia A neutron star." In: *Phys. Rev. C* 91 (1 2015), p. 015806. DOI: 10.1103/PhysRevC.91.015806. URL: https://link.aps.org/doi/10.1103/PhysRevC.91.015806.

[33] Feryal Özel. "Surface emission from neutron stars and implications for the physics of their interiors." In: *Reports on Progress in Physics* 76.1 (Dec. 2013), p. 016901. DOI: 10.1088/0034-4885/76/1/016901.

[34] D. G. Ravenhall, C. J. Pethick, and J. R. Wilson. "Structure of matter below nuclear saturation density." In: *Physical Review Letters* 50.26 (June 1983), pp. 2066–2069. DOI: 10.1103/physrevlett.50.2066.

[35] Zidu Lin, Matthew E. Caplan, Charles J. Horowitz, and Cecilia Lunardini. "Fast neutrino cooling of nuclear pasta in neutron stars: Molecular dynamics simulations." In: *Physical Review C* 102.4 (Oct. 2020), pp. 045801–1–12. DOI: 10.1103/physrevc.102.045801.

[36] Richard C. Tolman. *Relativity, Thermodynamics and Cosmology*. International series of monographs on physics. Oxford: The Clarendon Press, 1934.

[37] H. A. Buchdahl. "General Relativistic Fluid Spheres." In: *Physical Review* 116.4 (1959), 1027–1034. DOI: 10.1103/physrev.116.1027.

[38] Lee Lindblom. "Determining the Nuclear Equation of State from Neutron-Star Masses and Radii." In: 398 (Oct. 1992), p. 569. DOI: 10.1086/171882.

[39] Mark G. Alford, Steven P. Harris, and Pratik S. Sachdeva. "On the stability of strange dwarf hybrid stars." In: *Astrophys. J.* 847.2 (2017), p. 109. DOI: 10.3847/1538-4357/aa8509. arXiv: 1705.09880 [astro-ph.HE].

[40] Lee Lindblom. "Causal representations of neutron-star equations of state." In: 97.12, 123019 (June 2018), p. 123019. DOI: 10.1103/PhysRevD.97.123019. arXiv: 1804.04072 [astro-ph.HE].

[41] P. Bogacki and L.F. Shampine. "A 3(2) pair of Runge - Kutta formulas." In: *Applied Mathematics Letters* 2.4 (1989), pp. 321–325. ISSN: 0893-9659. DOI: https://doi.org/10.1016/0893-9659(89)90079-7.

[42] Pauli Virtanen et al. "SciPy 1.0: Fundamental Algorithms for Scientific Computing in Python." In: *Nature Methods* 17 (2020), pp. 261–272. DOI: 10.1038/s41592-019-0686-2.

[43] A.Y. Potekhin, J.A. Pons, and D. Page. "Neutron Stars—Cooling and Transport." In: *Space Sci Rev* 191 (2015), pp. 239–291. DOI: https://doi.org/10.1007/s11214-015-0180-9.

[44] Dany Page, James M. Lattimer, Madappa Prakash, and Andrew W. Steiner. "Minimal Cooling of Neutron Stars: A New Paradigm." In: *The Astrophysical Journal Supplement Series* 155.2 (2004), pp. 623–650. DOI: 10.1086/424844.

[45] Andrew Cumming, Edward F. Brown, Farrukh J. Fattoyev, C. J. Horowitz, Dany Page, and Sanjay Reddy. "Lower limit on the heat capacity of the neutron star core." In: *Phys. Rev. C* 95 (2 2017), p. 025806. DOI: 10.1103/PhysRevC.95.025806. URL: https://link.aps.org/doi/10.1103/PhysRevC.95.025806.

[46] M J P Wijngaarden, Wynn C G Ho, Philip Chang, Craig O Heinke, Dany Page, Mikhail Beznogov, and Daniel J Patnaude. "Diffusive nuclear burning in cooling simulations and application to new temperature data of the Cassiopeia A neutron star." In: *Monthly Notices of the Royal Astronomical Society* 484.1 (2019), pp. 974–988. DOI: 10.1093/mnras/stz042. URL: https://doi.org/10.1093%2Fmnras%2Fstz042.

[47] E. H. Gudmundsson, C. J. Pethick, and R. I. Epstein. "Structure of neutron star envelopes." In: 272 (Sept. 1983), pp. 286–300. DOI: 10.1086/161292.

[48] A. Y. Potekhin, G. Chabrier, and D. G. Yakovlev. "Internal temperatures and cooling of neutron stars with accreted envelopes." In: *Astron. Astrophys.* 323 (1997), p. 415. arXiv: astro-ph/9706148.

[49] C. O. Heinke, P. G. Jonker, R. Wijnands, C. J. Deloye, and R. E. Taam. "FURTHER CONSTRAINTS ON THERMAL QUIESCENT X-RAY EMISSION FROM SAX J1808.4-3658." In: *The Astrophysical Journal* 691.2 (2009), pp. 1035–1041. DOI: 10.1088/0004-637x/691/2/1035. URL: https://doi.org/10.1088%2F0004-637x%2F691%2F2%2F1035.

[50] M. Jaminon and C. Mahaux. "Effective masses in relativistic approaches to the nucleon-nucleus mean field." In: *Phys. Rev. C* 40 (1 1989), pp. 354–367. DOI: 10.1103/PhysRevC.40.354. URL: https://link.aps.org/doi/10.1103/PhysRevC.40.354.

[51] G. W. Carter and M. Prakash. "The quenching of the axial coupling in nuclear and neutron-star matter." In: *Physics Letters B* 525.3-4 (2002), pp. 249–254. DOI: 10.1016/s0370-2693(01)01452-6.

[52] Hideyuki Umeda, Sachiko Tsuruta, and Ken'ichi Nomoto. "Nonstandard Thermal Evolution of Neutron Stars." In: *The Astrophysical Journal* (Sept. 1994). DOI: 10.1086/174641.

[53] James M. Lattimer, C. J. Pethick, Madappa Prakash, and Pawel Haensel. "Direct URCA process in neutron stars." In: *Phys. Rev. Lett.* 66 (21 1991), pp. 2701–2704. DOI: 10.1103/PhysRevLett.66.2701. URL: https://link.aps.org/doi/10.1103/PhysRevLett.66.2701.

[54] Dany Page and James H. Applegate. "The Cooling of Neutron Stars by the Direct URCA Process." In: 394 (July 1992), p. L17. DOI: 10.1086/186462.

[55] Laura Tolos, Mario Centelles, Angels Ramos, Rodrigo Negreiros, and Veronica Dexheimer. "The Equation of State and Cooling of Hyperonic Neutron Stars." In: *15th Marcel Grossmann Meeting on Recent Developments in Theoretical and Experimental General Relativity, Astrophysics, and Relativistic Field Theories*. Ed. by Elia Battistelli, Robert T. Jantzen, and Remo Ruffini. World Scientific, Mar. 2022, 1860–1865. DOI: https://doi.org/10.1142/9789811258251_0277. arXiv: 1903.03525 [astro-ph.HE].

[56] Rodrigo Negreiros, V. A. Dexheimer, and S. Schramm. "Quark core impact on hybrid star cooling." In: *Phys. Rev. C* 85 (3 2012), p. 035805. DOI: 10.1103/PhysRevC.85.035805. URL: https://link.aps.org/doi/10.1103/PhysRevC.85.035805.

[57] Naoki Iwamoto. "Quark Beta Decay and the Cooling of Neutron Stars." In: *Phys. Rev. Lett.* 44 (24 1980), pp. 1637–1640. DOI: 10.1103/PhysRevLett.44.1637. URL: https://link.aps.org/doi/10.1103/PhysRevLett.44.1637.

[58] R. L. Workman et al. "Review of Particle Physics." In: *PTEP* 2022 (2022), p. 083C01. DOI: 10.1093/ptep/ptac097.

[59] D. Blaschke, S. Fredriksson, H. Grigorian, and F. Sandin. "Phase diagram of three-flavor quark matter under compact star constraints." In: *Phys. Rev. D* 72 (6 2005), p. 065020. DOI: 10.1103/PhysRevD.72.065020. URL: https://link.aps.org/doi/10.1103/PhysRevD.72.065020.

[60] Stefan B. Rüster, Verena Werth, Michael Buballa, Igor A. Shovkovy, and Dirk H. Rischke. "Phase diagram of neutral quark matter: Self-consistent treatment of quark masses." In: *Phys. Rev. D* 72 (3 2005), p. 034004. DOI: 10.1103/PhysRevD.72.034004. URL: https://link.aps.org/doi/10.1103/PhysRevD.72.034004.

[61] N. Chamel. "Superfluidity and Superconductivity in Neutron Stars." In: *Journal of Astrophysics and Astronomy* 38.3 (6 2017), p. 065020. DOI: 10.1007/s12036-017-9470-9. URL: https://doi.org/10.1007%2Fs12036-017-9470-9.

[62] Armen Sedrakian and John W. Clark. "Superfluidity in nuclear systems and neutron stars." In: *The European Physical Journal A* 55.9 (6 2019), p. 065020. DOI: 10.1140/epja/i2019-12863-6. URL: https://doi.org/10.1140%2Fepja%2Fi2019-12863-6.

[63] K. P. Levenfish and D. G. Yakovlev. "Suppression of neutrino energy losses in reactions of direct urca processes by superfluidity in neutron star nuclei." In: *Astronomy Letters* 20.1 (6 Jan. 1994), pp. 43–51. DOI: 10.1103/PhysRevD.72.065020. URL: https://ui.adsabs.harvard.edu/abs/1994AstL...20...43L.

[64] K. P. Levenfish and D. G. Yakovlev. "Specific heat of neutron star cores with superfluid nucleons." In: *Astronomy Reports* 38.2 (6 Mar. 1994), pp. 247–251. DOI: 10.1103/PhysRevD.72.065020. URL: https://link.aps.org/doi/10.1103/PhysRevD.72.065020.

[65] Wei-Chia Chen and J. Piekarewicz. "Building relativistic mean field models for finite nuclei and neutron stars." In: *Phys. Rev. C* 90 (4 2014), p. 044305. DOI: https://doi.org/10.1103/PhysRevC.90.044305. URL: https://link.aps.org/doi/10.1103/PhysRevC.90.044305.

[66] Melissa Mendes, Andrew Cumming, Charles Gale, and Farrukh J. Fattoyev. "Probing dense matter physics with transiently-accreting neutron stars: The case of source MXB 1659-29." In: *16th Marcel Grossmann Meeting on Recent Developments in Theoretical and Experimental General Relativity, Astrophysics and Relativistic Field Theories*. Vol. 72. American Physical Society, Oct. 2021, p. 065020. DOI: 10.1142/9789811269776_0309. arXiv: 2110.11077 [nucl-th]. URL: https://link.aps.org/doi/10.1103/PhysRevD.72.065020.

[67] J. Piekarewicz and M. Centelles. "Incompressibility of neutron-rich matter." In: *Phys. Rev. C* 79 (6 2009), p. 054311. DOI: https://doi.org/10.1103/PhysRevC.79.054311. arXiv: 0812.4499 [nucl-th]. URL: https://link.aps.org/doi/10.1103/PhysRevD.72.065020.

[68] James M. Lattimer and Andrew W. Steiner. "Constraints on the symmetry energy using the mass-radius relation of neutron stars." In: *Eur. Phys. J. A* 50, 40 (6 2014), p. 40. DOI: 10.1140/epja/i2014-14040-y. arXiv: 1403.1186 [nucl-th]. URL: https://ui.adsabs.harvard.edu/abs/2014EPJA...50...40L/exportcitation.

[69] Gordon Baym, Christopher Pethick, and Peter Sutherland. "The Ground State of Matter at High Densities: Equation of State and Stellar Models." In: *Astrophys. J.* 170 (6 1971), pp. 299–317. DOI: https://doi.org/10.1086/151216. URL: https://ui.adsabs.harvard.edu/abs/1971ApJ...170..299B/abstract.

[70] J.W. Negele and D. Vautherin. "Neutron star matter at sub-nuclear densities." In: *Nucl. Phys. A* 207.2 (6 1973), pp. 298–320. ISSN: 0375-9474. DOI: https://doi.org/10.1016/0375-9474(73)90349-7. URL: https://www.sciencedirect.com/science/article/pii/0375947473903497.

[71] J. Piekarewicz, F. J. Fattoyev, and C. J. Horowitz. "Pulsar glitches: The crust may be enough." In: *Phys. Rev. C* 90 (1 2014), p. 015803. DOI: 10.1103/PhysRevC.90.015803. URL: https://link.aps.org/doi/10.1103/PhysRevC.90.015803.

[72] D. Blaschke, S. Fredriksson, H. Grigorian, and F. Sandin. *Splrep documentation, version 1.11.1*. Online. 2005. DOI: 10.1103/PhysRevD.72.065020. URL: https://docs.scipy.org/doc/scipy/reference/generated/scipy.interpolate.splrep.html#scipy.interpolate.splrep.

[73] D. Blaschke, S. Fredriksson, H. Grigorian, and F. Sandin. *Splev documentation, version 1.11.1*. Online. 2005. DOI: 10.1103/PhysRevD.72.065020. URL: https://docs.scipy.org/doc/scipy/reference/generated/scipy.interpolate.splev.html#scipy.interpolate.splev.

[74] Achim Schwenk and Bengt Friman. "Polarization Contributions to the Spin Dependence of the Effective Interaction in Neutron Matter." In: *Phys. Rev. Lett.* 92 (8 2004), p. 082501. DOI: 10.1103/PhysRevLett.92.082501. URL: https://link.aps.org/doi/10.1103/PhysRevLett.92.082501.

[75] L. Amundsen and E. Østgaard. "Superfluidity of neutron matter: (I). Singlet pairing." In: *Nuclear Physics A* 437.2 (6 1985), pp. 487–508. ISSN: 0375-9474. DOI: https://doi.org/10.1016/S0375-9474(85)90103-4. URL: https://www.sciencedirect.com/science/article/pii/S0375947485901034.

[76] M. Baldo, J. Cugnon, A. Lejeune, and U. Lombardo. "Proton and neutron superfluidity in neutron star matter." In: *Nuclear Physics A* 536.2 (6 1992), pp. 349–365. ISSN: 0375-9474. DOI: https://doi.org/10.1016/0375-9474(92)90387-Y. URL: https://www.sciencedirect.com/science/article/pii/037594749290387Y.

[77] M. Baldo and H.-J. Schulze. "Proton pairing in neutron stars." In: *Phys. Rev. C* 75 (2 2007), p. 025802. DOI: 10.1103/PhysRevC.75.025802. URL: https://link.aps.org/doi/10.1103/PhysRevC.75.025802.

[78] J.M.C. Chen, J.W. Clark, R.D. Davé, and V.V. Khodel. "Pairing gaps in nucleonic superfluids." In: *Nuclear Physics A* 555.1 (6 1993), pp. 59–89. ISSN: 0375-9474. DOI: https://doi.org/10.1016/0375-9474(93)90314-N. URL: https://www.sciencedirect.com/science/article/pii/037594749390314N.

[79] N.-C. Chao, J.W. Clark, and C.-H. Yang. "Proton superfluidity in neutron-star matter." In: *Nuclear Physics A* 179.2 (6 1972), pp. 320–332. ISSN: 0375-9474. DOI: https:

//doi.org/10.1016/0375-9474(72)90373-9. URL: https://www.sciencedirect.com/science/article/pii/0375947472903739.

[80] Ø. Elgarøy, L. Engvik, M. Hjorth-Jensen, and E. Osnes. "Superfluidity in β-Stable Neutron Star Matter." In: *Phys. Rev. Lett.* 77 (8 1996), pp. 1428–1431. DOI: 10.1103/PhysRevLett.77.1428. URL: https://link.aps.org/doi/10.1103/PhysRevLett.77.1428.

[81] Ø. Elgarøy, L. Engvik, M. Hjorth-Jensen, and E. Osnes. "Model-space approach to 1S0 neutron and proton pairing in neutron star matter with the Bonn meson-exchange potentials." In: *Nuclear Physics A* 604.4 (6 1996), pp. 466–490. ISSN: 0375-9474. DOI: https://doi.org/10.1016/0375-9474(96)00152-2. URL: https://www.sciencedirect.com/science/article/pii/0375947496001522.

[82] Tatsuyuki Takatsuka. "Proton Superfluidity in Neutron-Star Matter." In: *Progress of Theoretical Physics* 50.5 (6 Nov. 1973), pp. 1754–1755. ISSN: 0033-068X. DOI: 10.1143/PTP.50.1754. eprint: https://academic.oup.com/ptp/article-pdf/50/5/1754/5209126/50-5-1754.pdf. URL: https://doi.org/10.1143/PTP.50.1754.

[83] L. Amundsen and E. Østgaard. "Superfluidity of neutron matter: (II). Triplet pairing." In: *Nuclear Physics A* 442.1 (6 1985), pp. 163–188. ISSN: 0375-9474. DOI: https://doi.org/10.1016/0375-9474(85)90140-X. URL: https://www.sciencedirect.com/science/article/pii/037594748590140X.

[84] M. Baldo, Ø. Elgarøy, L. Engvik, M. Hjorth-Jensen, and H.-J. Schulze. "${}^3P_2-{}^3F_2$ pairing in neutron matter with modern nucleon-nucleon potentials." In: *Phys. Rev. C* 58 (4 1998), pp. 1921–1928. DOI: 10.1103/PhysRevC.58.1921. URL: https://link.aps.org/doi/10.1103/PhysRevC.58.1921.

[85] Ø. Elgarøy, L. Engvik, M. Hjorth-Jensen, and E. Osnes. "Triplet pairing of neutrons in -stable neutron star matter." In: *Nuclear Physics A* 607.4 (6 1996), pp. 425–441. ISSN: 0375-9474. DOI: https://doi.org/10.1016/0375-9474(96)00217-5. URL: https://www.sciencedirect.com/science/article/pii/0375947496002175.

[86] Peter S. Shternin, Dmitry G. Yakovlev, Craig O. Heinke, Wynn C. G. Ho, and Daniel J. Patnaude. "Cooling neutron star in the Cassiopeia A supernova remnant: evidence for superfluidity in the core." In: *Monthly Notices of the Royal Astronomical*

Society: Letters 412.1 (6 Mar. 2011), pp. L108–L112. ISSN: 1745-3925. DOI: 10.1111/j.1745-3933.2011.01015.x. eprint: https://academic.oup.com/mnrasl/article-pdf/412/1/L108/3262203/412-1-L108.pdf. URL: https://doi.org/10.1111/j.1745-3933.2011.01015.x.

[87] Tatsuyuki Takatsuka. "Energy Gap in Neutron-Star Matter." In: *Progress of Theoretical Physics* 48.5 (6 Nov. 1972), pp. 1517–1533. ISSN: 0033-068X. DOI: 10.1143/PTP.48.1517. eprint: https://academic.oup.com/ptp/article-pdf/48/5/1517/5328994/48-5-1517.pdf. URL: https://doi.org/10.1143/PTP.48.1517.

[88] Tatsuyuki Takatsuka and Ryozo Tamagaki. "Baryon Superfluidity and Neutrino Emissivity of Neutron Stars." In: *Progress of Theoretical Physics* 112.1 (6 July 2004), pp. 37–72. ISSN: 0033-068X. DOI: 10.1143/PTP.112.37. eprint: https://academic.oup.com/ptp/article-pdf/112/1/37/19571870/112-1-37.pdf. URL: https://doi.org/10.1143/PTP.112.37.

[89] Mark G. Alford, Sophia Han, and Madappa Prakash. "Generic conditions for stable hybrid stars." In: *Phys. Rev. D* 88 (8 2013), p. 083013. DOI: 10.1103/PhysRevD.88.083013. URL: https://link.aps.org/doi/10.1103/PhysRevD.88.083013.

[90] J. L. Zdunik and P. Haensel. "Maximum mass of neutron stars and strange neutron-star cores." In: *Astron. Astrophys.* 551 (6 2013), A61. DOI: 10.1051/0004-6361/201220697. arXiv: 1211.1231 [astro-ph.SR]. URL: https://docs.scipy.org/doc/scipy/reference/generated/scipy.interpolate.splev.html#scipy.interpolate.splev.

[91] Jan-Erik Christian and Jürgen Schaffner-Bielich. "Supermassive Neutron Stars Rule Out Twin Stars." In: *Phys. Rev. D* 103.6 (6 2021), p. 063042. DOI: 10.1103/PhysRevD.103.063042. arXiv: 2011.01001 [astro-ph.HE]. URL: https://docs.scipy.org/doc/scipy/reference/generated/scipy.interpolate.splev.html#scipy.interpolate.splev.

[92] Jan-Erik Christian. "Neutron star equations of state with a phase transition in a relativistic mean field approach at finite temperatures." doctoralthesis. Universitätsbibliothek Johann Christian Senckenberg, 2023, p. 143. DOI: 10.21248/gups.74239. URL: https://publikationen.ub.uni-frankfurt.de/frontdoor/index/index/

start/4/rows/10/sortfield/score/sortorder/desc/searchtype/simple/query/Jan-Erik+Christian/docId/74239.

[93] Bikram Keshari Pradhan, Debarati Chatterjee, Radhika Gandhi, and Jürgen Schaffner-Bielich. "Role of vector self-interaction in neutron star properties." In: *Nucl. Phys. A* 1030 (6 2023), p. 122578. DOI: 10.1016/j.nuclphysa.2022.122578. arXiv: 2209.12657 [nucl-th]. URL: https://docs.scipy.org/doc/scipy/reference/generated/scipy.interpolate.splev.html#scipy.interpolate.splev.

[94] Jan-Erik Christian and Jürgen Schaffner-Bielich. "Confirming the Existence of Twin Stars in a NICER Way." In: *Astrophys. J.* 935.2 (6 2022), p. 122. DOI: 10.3847/1538-4357/ac75cf. arXiv: 2109.04191 [astro-ph.HE]. URL: https://docs.scipy.org/doc/scipy/reference/generated/scipy.interpolate.splev.html#scipy.interpolate.splev.

[95] D. Blaschke, S. Fredriksson, H. Grigorian, and F. Sandin. *Brentq documentation, version 1.11.1*. Online. 2005. DOI: 10.1103/PhysRevD.72.065020. URL: https://docs.scipy.org/doc/scipy/reference/generated/scipy.optimize.brentq.html.

[96] Adam Burrows, David Radice, David Vartanyan, Hiroki Nagakura, M Aaron Skinner, and Joshua C Dolence. "The overarching framework of core-collapse supernova explosions as revealed by 3D fornax simulations." In: *Monthly Notices of the Royal Astronomical Society* 491.2 (6 Nov. 2019), pp. 2715–2735. ISSN: 0035-8711. DOI: 10.1093/mnras/stz3223. eprint: https://academic.oup.com/mnras/article-pdf/491/2/2715/31221715/stz3223.pdf. URL: https://doi.org/10.1093/mnras/stz3223.

[97] X. Roca-Maza and N. Paar. "Nuclear equation of state from ground and collective excited state properties of nuclei." In: *Progress in Particle and Nuclear Physics* 101 (6 2018), 96–176. DOI: 10.1016/j.ppnp.2018.04.001. URL: https://docs.scipy.org/doc/scipy/reference/generated/scipy.optimize.brentq.html.